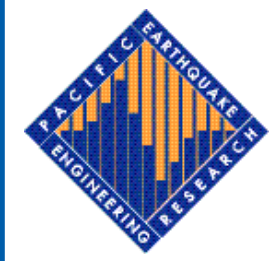

PACIFIC EARTHQUAKE ENGINEERING
RESEARCH CENTER

Modeling of Unreinforced Masonry Infill Walls Considering In-Plane and Out-of-Plane Interaction

Stephen Kadysiewski
Khalid M. Mosalam

University of California, Berkeley

PEER 2008/102
JANUARY 2009

Modeling of Unreinforced Masonry Infill Walls Considering In-Plane and Out-of-Plane Interaction

Stephen Kadysiewski
Department of Civil and Environmental Engineering
University of California, Berkeley

Khalid M. Mosalam
Department of Civil and Environmental Engineering
University of California, Berkeley

PEER Report 2008/102
Pacific Earthquake Engineering Research Center
College of Engineering
University of California, Berkeley

January 2009

ABSTRACT

This report describes a practical analytical model that can be used for the seismic evaluation of unreinforced masonry (URM) infill walls located within a reinforced concrete (RC) frame. The model, which consists of diagonal beam-column members utilizing fiber element cross sections, is suitable for use in a nonlinear time history analysis. The model considers both the in-plane (IP) and out-of-plane (OOP) response of the infill, as well as the interaction between IP and OOP capacities. The behavior is elastoplastic, and limit states may be defined by deformations or ductilities in the two directions. These limit states may be chosen to conform to various codes and guidelines, or they may be developed independently by the engineer. The model is composed of elements that are available in commonly used structural analysis software programs, and is based on small displacement theory, so it is rather straightforward to implement. For each infill wall panel modeled, one additional degree of freedom and two beam-column members are added to the overall structural model.

This report is part of a larger research program of investigation into RC frames with URM infill, carried out in recent years at the University of California, Berkeley. Some of the previous work is described, including a previously proposed strut and tie (SAT) model. The behavior of that SAT model is investigated, and it is found that under certain circumstances, problematic issues are encountered.

The newly proposed infill wall model is idealized as a single diagonal beam-column member, composed of two beam-column elements, with a node at the midspan. The midspan node is assigned a mass in the OOP direction to account for the inertial forces in that direction. The beam-column elements used in this report are force-based elements with inelastic behavior concentrated at the hinge regions. These regions are modeled using inelastic fibers, whose strength and locations are calculated to produce the desired IP-OOP strength interaction relationship for the panel. The interaction relationship is based on previous work conducted in an earlier phase of the research program. Additionally, the elastic stiffness and area of the fibers are determined such that the IP and OOP elastic dynamic properties of the infill panel and the overall model strength properties are preserved. The performance of a simple one-panel model is demonstrated using static pushover and dynamic analyses. The performance of the model is

shown to be generally satisfactory. However, possible limitations and drawbacks of the model are discussed, as well as possible improvements.

The proposed infill model is incorporated into a larger five-story model of a RC moment frame building with URM infill walls. The building model is the same as that used for earlier investigations in the research program. It is subjected to 20 sets of ground acceleration time histories, at five different levels of spectral acceleration. Collapse of the infill panel is assumed to occur at critical displacement ductilities in the IP and OOP directions, with interaction between the ductilities considered. Fragility functions, giving the probability of collapse as a function of spectral acceleration level, are calculated. These functions consider only the effect of record-to-record variability. Finally, the strength variability of the URM infill walls is considered using a first-order, second-moment (FOSM) analysis, and it is shown that the effect of this strength variability is minor compared with that of record-to-record variability. The effect of disregarding the interaction between IP and OOP strength, which is a common design practice, is discussed. The fragility functions produced in this report are found to give failure probabilities lower than those determined by earlier work in the research program, which assumed failure based on IP and OOP elastic forces rather than inelastic deformations. Conclusions and suggestions for further investigations are given at the end of the report.

ACKNOWLEDGMENTS

The authors would like to express their appreciation to Dr. Alidad Hashemi, for generously sharing both his advice and his OpenSees model, which forms the basis of the five-story building model used in Chapter 4.

The support of the Pacific Earthquake Engineering Research Center (PEER) in publishing this report is gratefully acknowledged. The authors specifically thank Ms. Janine Hannel, Senior Publications Coordinator, for her editing of the report.

CONTENTS

LIST OF FIGURES

LIST OF TABLES

1 Introduction

1.1 GENERAL

Reinforced concrete (RC) frames containing unreinforced masonry (URM) infill walls are a commonly used structural system, both in the United States and around the world. Many buildings of this type have performed poorly during earthquakes. In the United States such construction is no longer permitted; however, many such structures still exist. Kircher et al. (2006) indicate that concrete frames, including those with and without infill, represent one of the three major sources of seismic risk in the San Francisco region (the other two sources being URM bearing wall buildings and soft-story wood-frame structures). Jaiswal et al. (2002) report that RC frames with URM infill are currently being built in India in violation of the building codes, and that they performed poorly during the 2001 Bhuj earthquake. The 2008 earthquake in Wenchuan, China, provides numerous examples of frame-wall interaction (Li et al. 2008; see Figs. 1.1–1.2).

Fig. 1.1 Infill damage after Wenchuan, China 2008 earthquake (Li et al. 2008).

Fig. 1.2 Infill damage after Wenchuan, China 2008 earthquake (Mosalam and Sitar 2008).

The general outlines of the behavior and vulnerabilities of structures with URM infill are well known. Paulay and Priestley (1992) point out that infill walls may have beneficial or detrimental effects on the behavior of the overall structure. The beneficial effects derive from the fact that the infill walls add, at least during the initial stages of an earthquake, to the lateral force-resisting capacity and damping of the structure. However, the URM is brittle and prone to early failure due to in-plane (IP) loads, and interacts with the surrounding frame in such a way that column shear failure is made more likely. Also, the infill wall failure may lead to the formation of a soft story and consequent column failure. Failure of the URM walls in the out-of-plane (OOP) direction leads to life-safety hazard from falling debris. It is also known that there is an interaction effect between the IP strength of the wall and the OOP strength, with load in one direction reducing the strength in the other. This interaction is generally ignored in current engineering practice, such as FEMA 356 (FEMA 2000).

A number of conceptual models have been proposed to simulate the behavior of RC frame and infill wall structures (Hashemi and Mosalam 2007). This diversity of models reflects an epistemic uncertainty, one that stems from the rather complex interaction between the flexure-dominated frame and the shear-dominated infill wall panel. It is recognized that there is a need for a simple analytical model for the infill, one that can be incorporated into a model of the overall structure, and that will produce acceptably accurate responses. This report attempts to address that need.

1.2 BACKGROUND AND OBJECTIVES

This report is part of a larger study of the behavior of RC frames with URM infill walls, carried out in recent years at the University of California, Berkeley. An overview of the program of study is shown in Figure 1.3, and a detailed discussion of the program is given in Hashemi and Mosalam (2007), Elkhoraibi and Mosalam (2007), and Talaat and Mosalam (2008).

The subject matter of this report is contained in Block 14 and, to a lesser extent, Block 16. Block 14, "Development of new SAT models," refers to the development of a simple strut and tie model of infill wall behavior. This work was begun by Hashemi and Mosalam (2007), who proposed a simple inelastic SAT model, one which simulates both the IP and the OOP responses of a panel, and incorporates the interaction relationship between the IP and OOP strength of the panel. This relationship was derived from a detailed nonlinear finite element analysis (FEA) of a single infill panel. Block 16, "Reliability analysis for performance evaluation of RC structures with URM infill walls" refers to the use of the proposed URM infill wall model in an overall structural model, and the calculation of fragility functions, which give the probability of failure as a function of the earthquake intensity measure. Hashemi and Mosalam (2007) have begun work on this subject also, using an elastic infill model, which therefore did not include the inelastic behavior of their SAT model.

The objectives of this report are

1. To perform a detailed evaluation of the SAT model proposed by Hashemi and Mosalam (2007);
2. To improve the numerical stability and behavior of that model, and to investigate and demonstrate in detail the behavior of an improved model; and
3. To incorporate the improved infill wall model into an overall model of a representative building, and to calculate vulnerability functions for the infill panels themselves, as well as for selected global responses of the building.

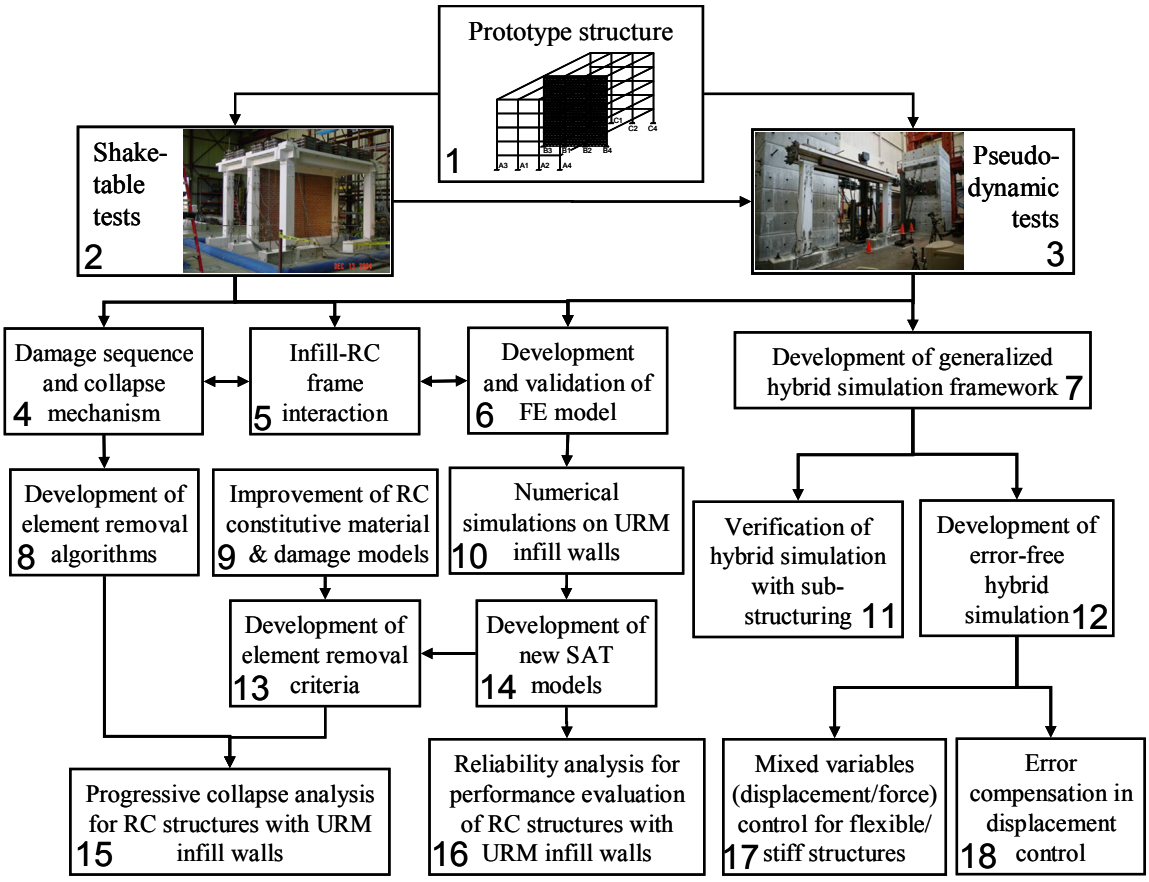

Fig. 1.3 Overview of study program for RC frames with URM infill.

1.3 OUTLINE OF THE REPORT

Chapter 2 contains an evaluation of the SAT infill wall model previously proposed by Hashemi and Mosalam (2007). This evaluation includes an application of two types of static pushover analysis to the proposed model. In this pushover analysis, bidirectional loading is applied in the IP and OOP directions. One type of the pushover analysis is the "conventional" pushover, in which a constant force is applied in one direction, with a monotonically increasing displacement applied in the other direction. The other type of the pushover analysis is a "double displacement" pushover, in which monotonically increasing displacements are applied in both directions. The results of these analyses are then discussed, and conclusions are drawn.

Chapter 3 presents an improved infill wall model, consisting of a diagonal beam-column element, with a cross section composed of nonlinear fiber elements. The infill wall panel stiffness, strength, and limit state deformation are based on values provided by other means, such

as FEMA 356 (FEMA 2000) or experimental results if available. The derivations of the properties of the model are outlined in detail, such that the dynamic properties of the infill model match those calculated using a vertically spanning, distributed mass model of the infill panel. The behavior of a simple one-panel model is then demonstrated, using conventional pushover, fiber-section cyclic pushover, and time history analyses. The responses are presented, the characteristics of the model are discussed, and limitations and opportunities for further developments are outlined.

Chapter 4 utilizes the improved infill wall model in an example vulnerability analysis. The model is incorporated into an overall model of a five-story RC frame building with infill walls, and analyzed for its response to a suite of twenty ground motion time histories. For each analysis, the time histories are scaled to a common spectral acceleration, *Sa*, measured at the fundamental period of the building. The analysis is performed for each of five different values of *Sa*. From the results of these analyses, the probability that a selected infill wall panel will exceed a threshold value, taken in this study as the FEMA 356 (FEMA 2000) "collapse prevention" (CP) limit state, is determined as a function of *Sa*. Finally, a vulnerability analysis is carried out for a global response of the building. For this case the interstory drift ratio (IDR) is examined.

Since the analysis just described assumes that all the structural properties are deterministic with exactly defined parameters, the resulting uncertainty is a product of only the record-to-record uncertainty in the time histories. This is also known as ground motion profile (GMP) uncertainty. In order to illustrate the effects of other uncertainties, an analysis is made to determine the contribution to infill wall collapse uncertainty due to uncertainty in the infill strength. This uncertainty is calculated using a first-order, second-moment (FOSM) approach, and is then compared to the GMP uncertainty.

Chapter 5 presents a summary of the report, conclusions, and opportunities for further improvements in the infill wall model and the vulnerability study.

1.4 REPORT CONTRIBUTIONS

This report takes a step forward in the practical modeling and analysis of URM infill walls. Three items of particular interest are:

1. A theoretical development of the OOP properties (mass, stiffness, strength) of the model for the infill panel is given in Appendix D. The use of these properties ensures that the

global responses of the overall building model (of which the infill panel model is a subsystem) will be closely approximated, relative to a case in which the panels are modeled in detail such as using finite elements.

2. In Chapter 3, a methodology is derived for calculating the strength properties of the cross-section fibers used in the beam-column element that comprises the infill panel model. The methodology, based on a straightforward calculation, ensures that the target interaction relationship between IP axial strength and OOP bending strength for the infill panel model will be satisfied under all conditions of load and deformation. This methodology has the potential for a wider field of application than is illustrated here.
3. An example vulnerability study, using the proposed infill model as part of a larger RC moment frame building model, is presented in Chapter 4. The study calculates the probability of infill wall collapse as a function of spectral acceleration. It considers both the IP and OOP capacities of the infill wall, as well as interaction between them. In this study, the CP limit state capacities are defined as a function of the infill wall deformations.

2 Review of Previously Proposed Strut and Tie Model

As discussed in Chapter 1, this report is part of a larger program, investigating the seismic behavior of reinforced concrete (RC) frames with unreinforced masonry (URM) infill walls. In previous work, Hashemi and Mosalam (2007) proposed a strut and tie (SAT) model that would account for both the in-plane (IP) and out-of-plane (OOP) responses of the infill, including the interaction between the two directions. This chapter examines the behavior of that model.

2.1 DESCRIPTION OF STRUT AND TIE MODEL

The SAT model proposed by Hashemi and Mosalam (2007) is shown in Figure 2.1. The model consists of eight compression-only struts, arranged as shown, connected with a tension-only tie at the center point of the infill panel. The nature of the compressive stress-strain relationship is indicated in the figure. From zero to peak stress the relationship is parabolic, while the post-peak relationship is linear, down to a constant residual resistance. The model behavior is calculated based on finite displacements of the degrees of freedom, and is therefore geometrically as well as materially nonlinear. Using monotonic pushover analyses, Hashemi and Mosalam (2007) have calibrated the properties of the model so that its IP, OOP, and interaction behavior matches those of a nonlinear finite element model of a prototype infill panel. It is this calibrated model which is examined in the following sections of this chapter. Detailed properties of the model are given in Appendix B.

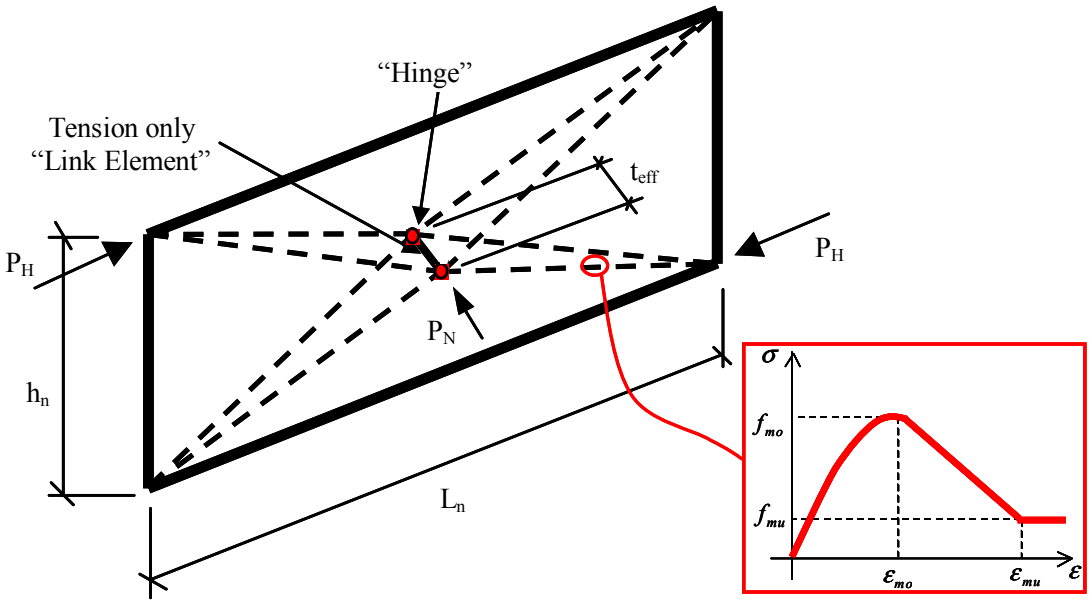

Fig. 2.1 Strut and tie model (Hashemi and Mosalam 2007).

2.2 COMPUTATIONAL MODELING AND ANALYSIS OF STRUT AND TIE MODEL

In order to examine the behavior of the SAT model, a computational analysis model is created using the program MathCad (MathSoft 1997). The properties of the model are identical to those described by Hashemi and Mosalam (2007). The deformation and force relationships of the model are given in Appendix A. There are essentially two degrees of freedom (DOFs) in the SAT model: the IP longitudinal deflection and the OOP transverse deflection. There are also two methods by which static pushover analysis may be conducted. One method may be thought of as a more conventional approach, in which a constant force is applied to one DOF, while a monotonically increasing displacement is imposed on the other DOF. Another, less common method, is to impose deformations on both DOFs. This latter method may be called the "double displacement pushover" method.

The double displacement method has the attractive feature that, given the displacements, the member deformations and forces may be calculated directly, without a requirement for iteration. The resultant forces, P_H and P_N may then be determined directly from equilibrium, where

P_H = resultant IP horizontal force, and
P_N = resultant OOP horizontal force.

For this study the displacements are applied monotonically to the IP and OOP DOFs in a ratio that is held constant for a given case, from zero displacements to their maximum values. There are six separate cases considered, ranging from pure IP displacement to pure OOP displacement, with a variety of intermediate ratios.

The maximum OOP displacement is chosen as 10 in., since this is the "snap-through" displacement, beyond which all eight of the struts are on one side of the wall's midplane. The maximum IP displacement is chosen as 3 in., since preliminary testing of the model indicates that a unidirectional IP displacement of about that value will reduce the IP force capacity to zero. The imposed double displacement paths are shown in Figure 2.2. An example MathCad analysis, for the case where both the maximum IP displacement and the maximum OOP displacement are 3 in. (Case 2), is given in Appendix B.

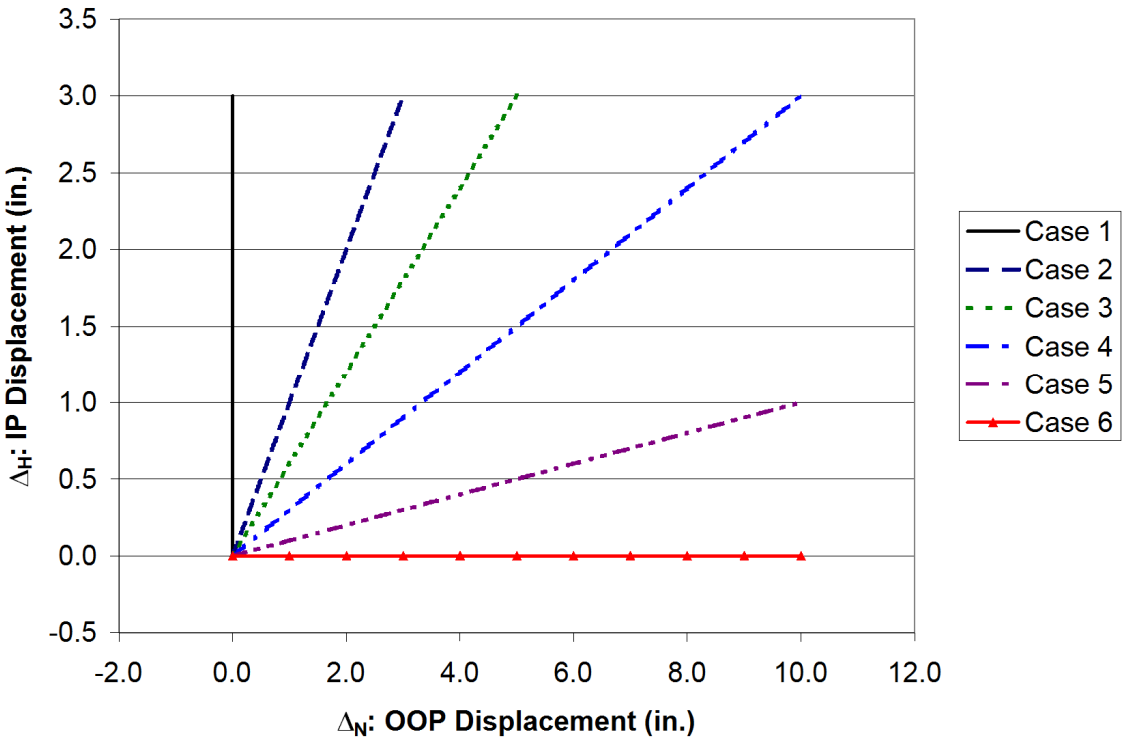

Fig. 2.2 IP-OOP displacement loading paths for double-displacement pushover analysis.

The resulting IP-OOP force paths for the six cases are shown in Figure 2.3. Also shown in that figure is the envelope interaction curve developed by Hashemi and Mosalam (2007). It is noted that the cases where the displacements are purely in-plane or out-of-plane produce

corresponding unidirectional forces, as expected. However, the intermediate cases produce more complex force paths, with some rather surprising results. A few of the unexpected results, along with their explanations, are discussed in the following paragraphs.

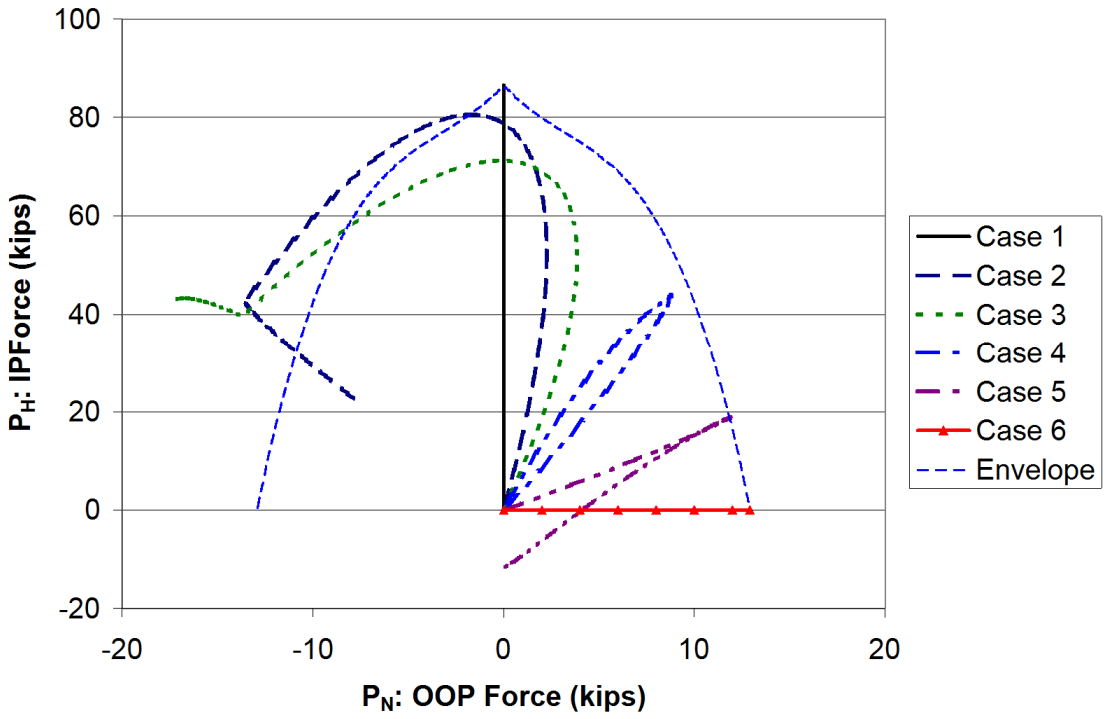

Fig. 2.3 IP-OOP force paths.

For Case 2, where the displacement vector has equal IP and OOP components, the out-of-plane force, P_N, is positive at first. This is expected, since the out-of-plane displacement, Δ_N, is also positive. However, as the displacements increase, P_N becomes negative. This behavior is perhaps somewhat surprising. A closer study of the analysis results indicates that the four strut elements that comprise the "compression diagonal" remain in compression during the entire duration of the displacement loading (see Fig. 2.4), since the deformed geometry of the frame is dominated by the in-plane displacement. All the elements in the "tension diagonal" show tensile strain throughout, and therefore do not contribute to the force response.

During early stages of loading, strut elements 1 and 7 carry more load, since their strains are higher than elements 2 and 8, due to the fact that IP and OOP strains are additive in elements 1 and 7 and subtractive in elements 2 and 8. Thus, P_N is positive as shown. However, as the loading proceeds, elements 1 and 7 reach their maximum capacities (corresponding to maximum

stress of 2.46 ksi), and their loads thereafter decline. Elements 2 and 8 continue to increase in load, eventually becoming larger than elements 1 and 7. At some point, the sign of P_N reverses. The important point to notice is that while the forces do not exceed the interaction envelope in the first quadrant, they do exceed it in the second. This must be viewed as a problem with the model behavior.

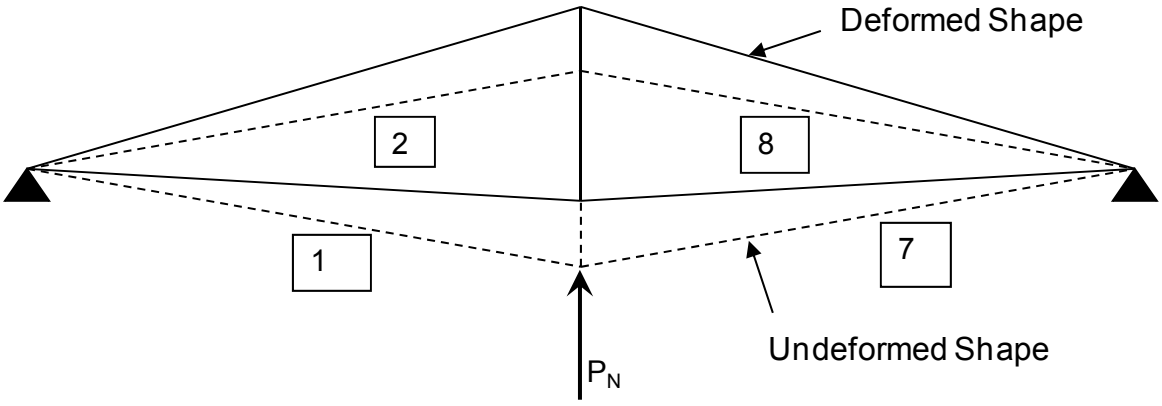

Fig. 2.4 Displacement relationships in compression diagonal.

For cases where the displacement loading pattern is almost purely out-of-plane, e.g., Case 5, another situation develops in which the in-plane force P_H is positive at first and then becomes negative. Here, all strut elements on one side of the model with respect to the midplane remain in compression throughout the loading, while the other elements remain in tension (hence they have zero force). As displacement loading begins, the two compression elements in the "compression diagonal" have higher loads than the two compression elements in the so-called "tension diagonal," since their strains are larger. This produces a positive value of P_H. As loading proceeds, the compression diagonal struts exceed their maximum strengths, lose load, and the resultant value of P_H changes sign.

The results of the more conventional pushover analyses, in which the OOP forces are held constant, while the IP displacement is increased monotonically, are shown in Figures 2.5–2.7. This form of analysis is somewhat more difficult to accomplish, since no solution with finite OOP displacements exists above a maximum IP displacement, which varies with out-of-plane load. Attempting to exceed that maximum displacement will result in a non-convergence (as OOP displacement goes to infinity), so that displacement must be determined before the start of the analysis. Although a subroutine could be written, it was found most convenient for this

study to find the maximum in-plane displacement graphically, as shown in the sample MathCad workbook given in Appendix C. Once the maximum in-plane displacement is found, the analysis proceeds in a relatively straightforward manner, using an iterative procedure to find the out-of-plane displacement corresponding to the given in-plane displacement and out-of-plane force. The last step is to use the displacement vector to calculate the in-plane force at each step.

Figure 2.5 shows the conventional pushover curves for the SAT model. The IP force, P_H, is given as a function of the IP displacement, Δ_H, with the constant OOP force, P_N, as noted in the legend. For each curve, the maximum displacement shown is the last displacement at which the solution is stable. Figure 2.6 shows the IP-OOP displacement path during the pushover; this figure corresponds to Figure 2.2 above. Figure 2.7 shows the IP-OOP force path, and corresponds to Figure 2.3.

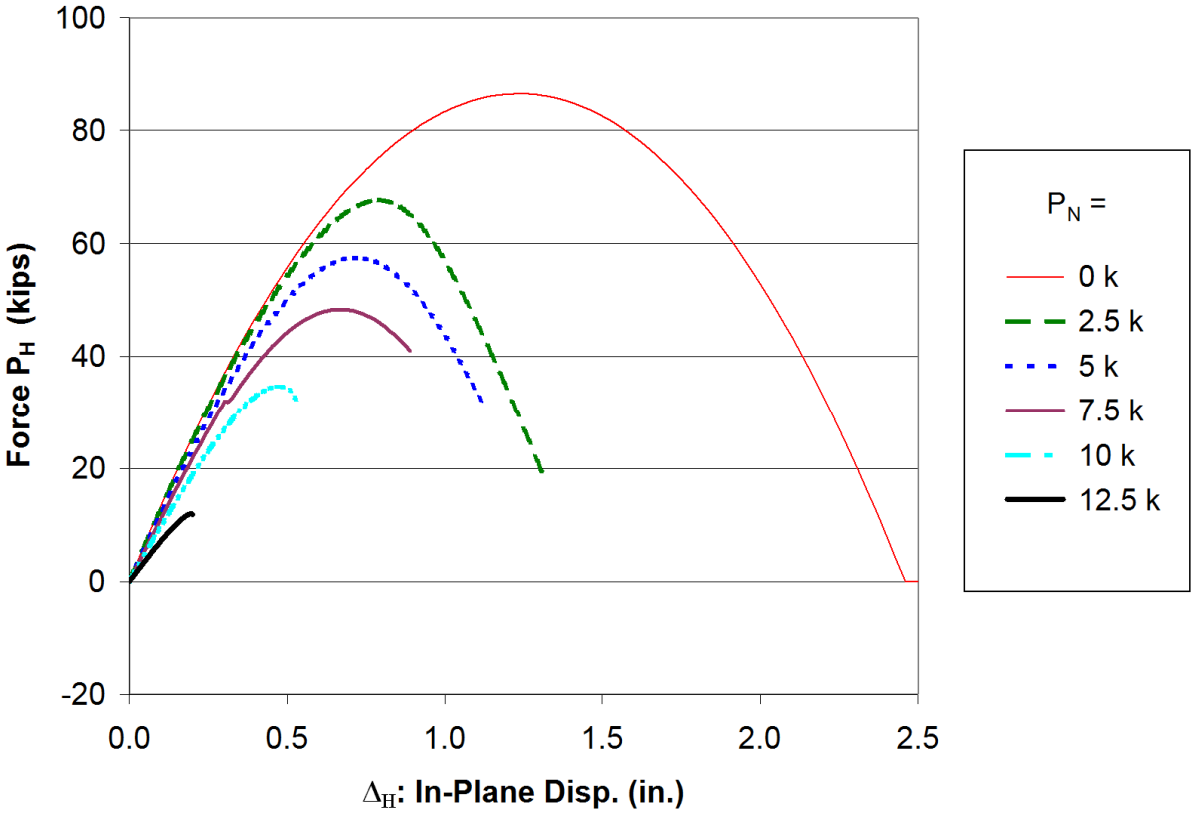

Fig. 2.5 IP force vs. IP displacement, conventional pushover analysis with constant OOP forces as noted.

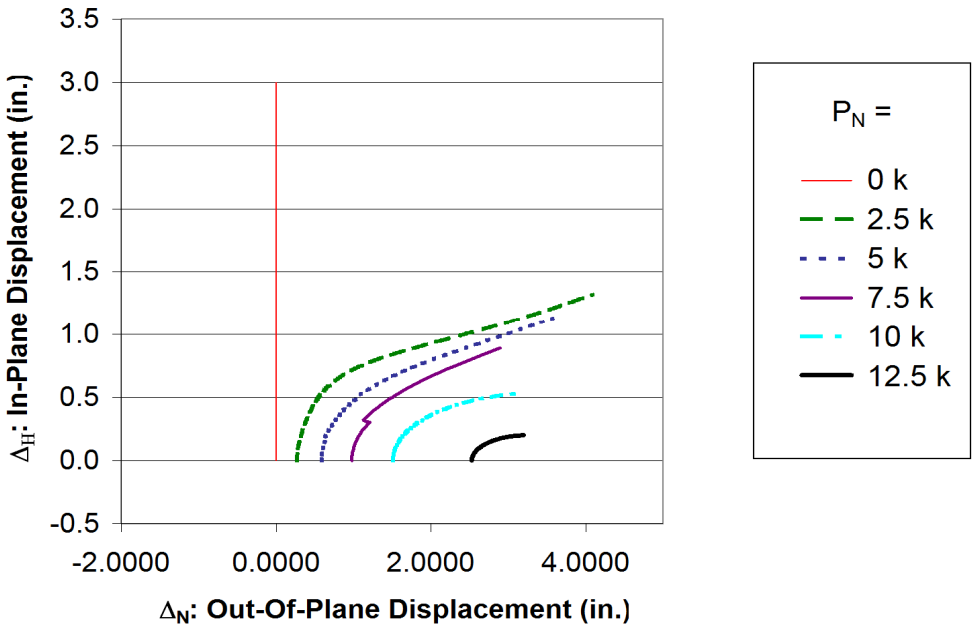

Fig. 2.6 IP-OOP displacement paths.

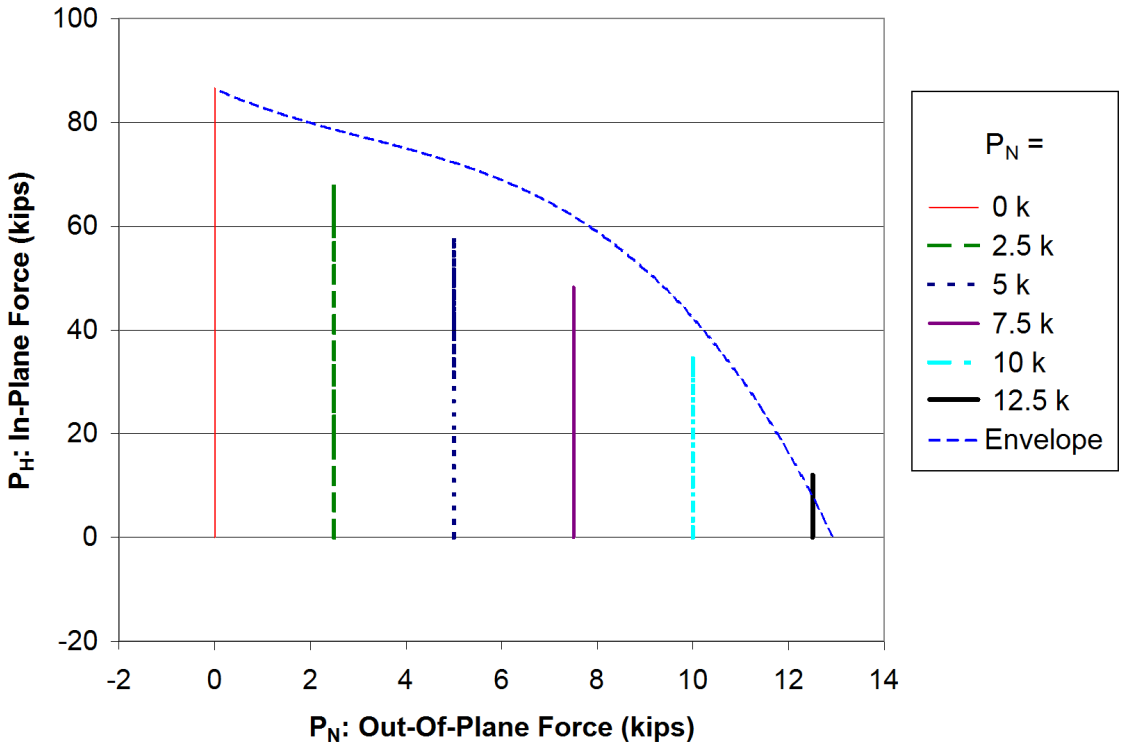

Fig. 2.7 IP-OOP force paths.

Again, some interesting features present themselves. On some of the displacement curves (e.g., Fig. 2.6, $P_N = 7.5$ k), a break in slope is observed at fairly low displacements. The break also appears on the corresponding load deflection curve (Fig. 2.5, $P_N = 7.5$ k). At first it was suspected that this break represents a numerical problem with the analysis. However, closer inspection of the analysis output (See the MathCad file, Appendix C) reveals that the break occurs at the load steps in which some of the struts are transitioning from compression to tension, or vice versa. While an analysis based on small displacement theory would predict that exactly four struts would be in compression at all times, the finite displacement, i.e., "exact," theory used here shows that there is a point during the transition in which there are only two struts in compression, thus leading to lower stiffness. While this effect is theoretically interesting, it is not anticipated that it would have a significant effect on the overall analysis.

2.3 CONCLUSIONS

As discussed above, the empirically derived SAT model proposed by Hashemi and Mosalam (2007) exhibits some problematical behaviors under certain conditions. For instance, it is possible that the IP and OOP force path may violate the chosen interaction relationship. Additionally, the model may become unstable under combinations of high IP displacement and high OOP loads. Also, issues such as cyclic behavior and hysteretic damping (intended or not intended) need to be addressed. Based on these concerns, an alternate infill model is presented in Chapter 3.

3 Proposed Fiber-Section Interaction Model

Given the problems associated with the strut and tie (SAT) infill model, discussed in Chapter 2, it is decided to develop a new model with fiber discretization. In this model the inherent interaction between the in-plane (IP) and out-of-plane (OOP) responses are explicitly addressed in the discretization process of the cross section. A sketch of this model is shown in Figure 3.1. For each infill panel, representing a single bay in a single story, the model consists of one diagonal member. That member is composed of two beam-column elements, joined at the midpoint node. This node is given a lumped mass in the OOP direction. The surrounding frame elements (dashed lines) are not part of the proposed infill panel model, and are shown in the figure for reference only. Such elements are handled separately using well-known modeling techniques of framed structures. The infill model takes advantage of the ability, e.g., using OpenSees (Mazzoni et al. 2006), to model a cross section as an arbitrary collection of nonlinear fiber elements. The procedure for constructing this model is discussed in the following sections. A discussion of the theory for developing the equivalent OOP properties of the model is given in Appendix D. Detailed calculations are given in Appendix E, and a summary of the calculation steps is given in Table 3.2, at the end of Section 3.5 of this chapter. The structural dimensions and material strengths for the infill panel and surrounding beams and columns in the example adopted for this chapter are identical to those used by Hashemi and Mosalam (2007) and are also included for completeness in Appendix E.

It should be pointed out that the formulation of the proposed model is different from that used by Hashemi and Mosalam (2007), or by FEMA 356 (FEMA 2000), in that it uses only one diagonal member rather than the two compression-only diagonal struts used in those references. This is because, as will be seen later, using only one diagonal member is sufficient in order to satisfy the IP-OOP interaction relationship. Because of this, the proposed model uses a diagonal member with both tension and compression strength. This single diagonal member approach causes a somewhat different distribution of forces in the surrounding structure. However, if the

floor diaphragms are relatively stiff and strong, as is often the case, the consequences of this simplification are expected to be minor.

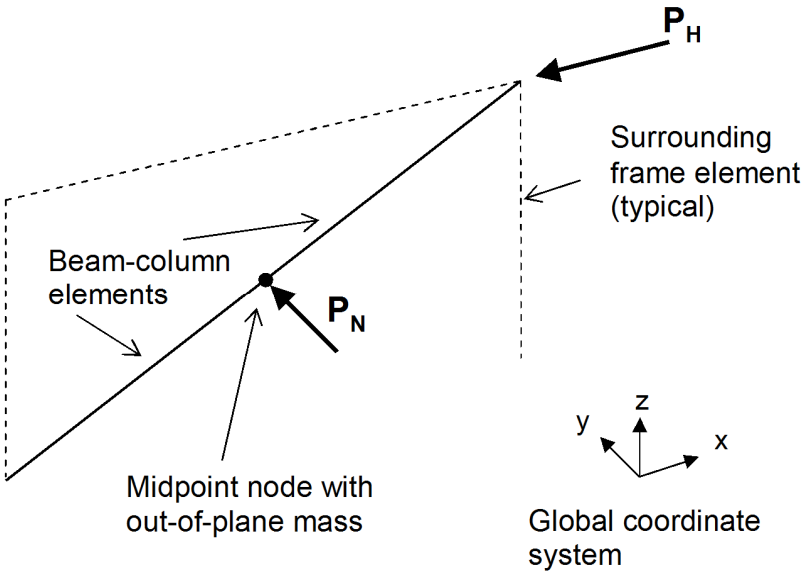

Fig. 3.1 Proposed infill model using beam-column elements with fiber discretization.

3.1 MODEL OBJECTIVES

It is desirable for the fiber-section model to exhibit the following attributes, relative to the actual infill wall that it represents:

1. For pure IP behavior, the model should provide a prescribed axial stiffness and strength (specified later in this chapter).
2. For pure OOP deflections, the model should have the same natural frequency as the infill wall. Locally, the model should produce the same support reactions, where it is originally attached to the surrounding structure, for a given support motion. Moreover, it should exhibit initial yielding at the same level of support motion that causes the infill wall to yield.
3. For combined IP and OOP behavior, the model should exhibit the specified strength interaction (discussed later) between IP strength and OOP strength.
4. For simplicity, in the post-yield region, the model is designed to behave in a perfectly plastic manner, i.e., there is no degradation of the stress in the model materials with increasing strain. Although this simplification is not realistic in general circumstances,

for small ductilities, as expected in unreinforced masonry (URM) walls, the simplification is acceptable and is consistent with the assumptions of documents such as FEMA 356 (FEMA 2000). As will be shown, it is necessary to track the ductilities resulting from the analysis model, and to recognize that the member has failed when it exceeds a specified ductility capacity. This is performed in the post-processing phase of the analysis, i.e., this is not conducted internally in the model formulation. The consequences of this simplification will be discussed in Section 3.7.

3.2 IN-PLANE PROPERTIES

The in-plane behavior of the infill panel is modeled by a diagonal strut, following the procedures given in Section 7.5 of FEMA 356 (FEMA 2000). The strut is given a thickness (normal to the wall), t_{inf}, equal to the actual infill thickness [in]. The width of the strut, a, is given by Equation 7-14 in FEMA 356 (FEMA 2000), and reproduced below:

$$a = 0.175 \left(\lambda_1 h_{col}\right)^{-0.4} r_{\text{inf}} \tag{3.1}$$

$$\lambda_1 = \left(\frac{E_{me}\, t_{\text{inf}} \sin 2\theta}{4\, E_{fe}\, I_{col}\, h_{\text{inf}}} \right)^{\frac{1}{4}} \tag{3.2}$$

where h_{col} is the column height between centerlines of beams [in], h_{inf} is the height of infill panel [in], E_{fe} and E_{me} are the expected moduli of elasticity of the frame and infill materials, respectively [ksi]. I_{col} is the moment of inertia about the out-of-plane axis of the column cross section [in.^{4}]. L_{inf} is the length of the infill panel [in], r_{inf} is the diagonal length of the infill panel [in], θ is the angle whose tangent is the infill height-to-length aspect ratio [radians], i.e., $\tan\theta = h_{\text{inf}} / L_{\text{inf}}$, and λ_1 is a coefficient used to determine the equivalent width of the infill strut, a. Application of the above equation to the case studied in Hashemi and Mosalam (2007) produces a value for $a = 16.8$ in.. In order for the present study to be comparable to Hashemi and Mosalam (2007), E_{me} is taken as 1770 ksi, and t_{inf} is taken as 3.75 in., matching their values. Based on the values of these parameters, the stiffness of the equivalent strut, k_{inf}, is calculated as 616.7 kip/in., and the equivalent area of the diagonal element, A_{elem}, is 67.8 in.^{2} (see Appendix E for more details of the calculations).

The axial strength of the equivalent strut of the infill panel for pure IP loading, P_{A0}, is determined by transforming the expected infill shear strength, V_{ine}, determined by using the methodology given in Section 7.5.2.2 in FEMA 356 (FEMA 2000):

$$V_{ine} = v_{me} A_n \tag{3.3}$$

where A_n is the area of the net mortared/grouted horizontal section across the infill panel, and v_{me} is the expected shear strength of the masonry infill (see Appendix E for details). Accordingly, the axial strength of the diagonal member is obtained as follows:

$$P_{N0} = V_{ine} / \cos\theta \tag{3.4}$$

For the case studied by Hashemi and Mosalam (2007), $P_{N0} = 55.3$ kips. Dividing this value by the axial stiffness, k_{inf}, gives an axial deflection at "yield," $\Delta_{Ay0} = P_{N0} / k_{\text{inf}} = 0.09$ inch. The IP horizontal deflection at yield is then $\Delta_{Hy0} = \Delta_{Ay0} / \cos\theta = 0.11$ inch.

Based on the axial strength of the strut and its inclination, θ, the resulting horizontal IP resistance of the infill model, $P_{H0} = V_{ine} = P_{A0} \cos\theta = 46.0$ kips. Since, as discussed earlier, the infill panel is modeled with only one diagonal strut, but has equal capacity for loading in either the positive or negative IP horizontal direction, the axial capacity of the member is identical in tension and compression.

FEMA 356 (FEMA 2000) also enables calculating of the IP horizontal displacement of the wall at the "collapse prevention" (CP) limit state. Using Table 7-9 and Section 7.5.2.3.4 of FEMA 356 (FEMA 2000), the IP horizontal deflection at CP (for assumed ratio of frame to infill strengths $\beta = V_{fre} / V_{ine} \le 0.7$, where the frame is assumed to have small strength compared to the infill panel), and for infill panel aspect ratio $L_{\text{inf}} / h_{\text{inf}} = 150/101.5 \approx 1.5$, is calculated as $\Delta_{Hcp0} = 0.355$ inch. From this estimate, the implied ultimate horizontal displacement ductility is $\mu_{H0} = \Delta_{Hcp0} / \Delta_{Hy0} = 0.355/0.11 = 3.3$. As noted before, this CP limit state is not reflected in the behavior of the proposed model itself, since the fiber material does not degrade. However, potential attainment of the CP limit state is determined by post-processing of the calculated displacements.

3.3 OUT-OF-PLANE PROPERTIES

The OOP strength of the URM infill wall is determined using the procedure in Section 7.5.3.2 of FEMA 356 (FEMA 2000). Based on arching action, the expected OOP capacity of the infill [psf] is given by

$$q_{ine} = \frac{0.7 f_{me} \lambda_2}{h_{\text{inf}} / t_{\text{inf}}} \times 144 \tag{3.5}$$

where f_{me} is the expected compressive strength of the masonry (2460 psi), and λ_2 is the slenderness parameter defined in Table 7.11 in FEMA 356 (FEMA 2000). For the case study structure from Hashemi and Mosalam (2007), $h_{\text{inf}} / t_{\text{inf}} = 101.5 / 3.75 = 27.1$. The value of λ_2 is obtained by linear extrapolation from Table 7-11 of FEMA 356 (FEMA 2000) as 0.0087 (see Appendix E). Therefore, the OOP capacity is estimated as 79.3 psf.

Since the infill weighs about 40 psf (total panel weight of approximately 4 kips), this represents a uniform acceleration capacity of approximately 2.0g. Using an effective cracked moment of inertia of one half the gross moment of inertia, the OOP first-mode natural frequency is estimated as 11.6 Hz. This estimate is based on assuming that the infill spans vertically with pinned connections at the top and bottom edges. The first-mode effective weight, 3.2 kips, is 81% of the total weight of the infill panel (see Appendix D). This effective weight (divided by g) is used in the proposed model as an OOP-only horizontal mass at the midspan node. This ensures that the OOP reactions at the upper and lower nodes of the proposed model due to dynamic loading (e.g., earthquake) are consistent (within the reasonable assumption of dominance of the first mode of vibration) with those resulting from detailed continuum modeling of the actual infill wall, thus preserving the floor diaphragm displacements and accelerations.

Knowing the concentrated mass and the frequency of the proposed model, the required equivalent stiffness, $E_m I_{eq}$, of the model beam-column member (with span equal to the infill wall diagonal) can be determined. For the case study structure, the value of the equivalent moment of inertia I_{eq} is determined to be 3824 in.^{4} (see Appendix E). Finally, the midspan yield moment of the member is calculated, such that the model element yields at the same level of support motion as the actual infill wall. This value is found to be 320.5 kip-in., corresponding to an applied OOP nodal force of 6.6 kips.

As with the IP case, the OOP "yield" displacement is calculated as the OOP load-carrying capacity divided by the translational stiffness of the equivalent member (based on its bending stiffness). This value is 0.15 inch for the case study structure (see Appendix E). FEMA 356 (FEMA 2000) provides a value of OOP displacement for the CP limit state. This value, taken as 5% of the infill height, results in a calculated displacement unrealistically greater than the thickness of the infill for the single wythe wall considered in the case study structure. As pointed out by Sharif et al. (2007), a rigid-body rocking model would predict that the OOP resistance of a URM wall would vanish at a displacement equal to its thickness. Since this value seems excessive, it is decided to define the OOP CP displacement ductility as 5.0. This implies an OOP displacement at CP of 0.75 inch, which is approximately 20% of the wall thickness. This value is judged to be more realistic and possibly somewhat conservative.

3.4 CONSIDERATION OF INTERACTION EFFECTS

The previous work by Hashemi and Mosalam (2007), based on a nonlinear finite element (FE) model of the infill panel, indicated that there is an interaction between IP and OOP capacities. In that study the interaction function was expressed as a third-degree polynomial. The polynomial coefficients have been derived to provide a best fit to the FE results. This has resulted in an interaction curve which is not convex at all points. Since the procedure used in this report for creating the fiber element section requires a convex curve (as discussed later), it is necessary to create an alternative interaction equation, one which will also provide a good match to the FE results.

After some numerical experimentation, it is found that an interaction curve of the following form provides a good match to the FE model results, and is also convex.

$$\left(\frac{P_N}{P_{N0}}\right)^{\frac{3}{2}} + \left(\frac{P_H}{P_{H0}}\right)^{\frac{3}{2}} \leq 1.0 \tag{3.6}$$

where P_N is the OOP capacity in the presence of IP force, P_{N0} is the OOP capacity without IP force, P_H is the IP capacity in the presence of OOP force, and P_{H0} is the IP capacity without OOP force. The proposed relationship in Equation (3.6) is compared with the previously proposed third-degree polynomial, as well as the FE results, in Figure 3.2. It is clearly observed that the proposed relationship provides a better match to the FE results.

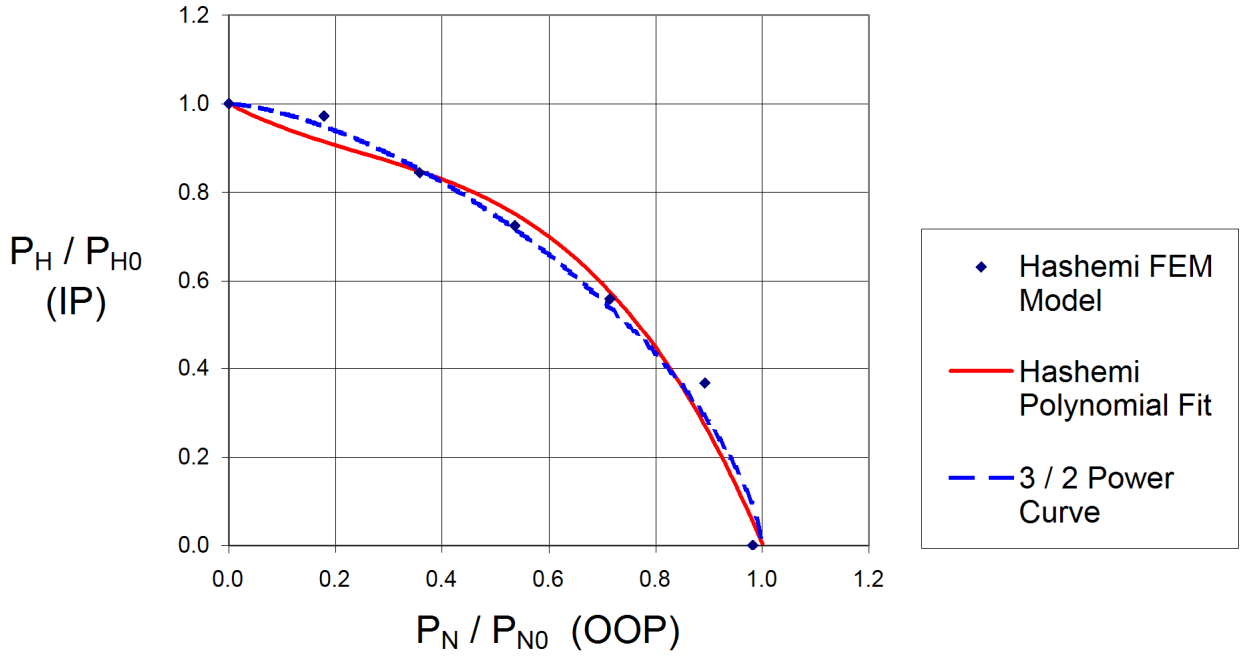

Fig. 3.2 Comparison of interaction curves for typical infill panel with FE results.

Since the fiber-section model, as described later, has pinned connections to the surrounding structure, it is possible to use the ratio of the OOP bending moment strengths instead of the ratio of the OOP force capacities. Thus, the interaction may be expressed as a "P-M" interaction diagram. This fact is used in Section 3.5 when calculating the properties of the fibers in the model.

Based on the results shown in Figure 3.2, it is decided to accept the proposed 3/2 power interaction relationship. It is to be noted that one of the limitations of the subsequent development is that it is assumed that the behavior of the infill wall is symmetric with respect to both IP and OOP behavior. Therefore, the adopted interaction curve is also doubly symmetric, as shown in Figure 3.3, expressed as a "P-M" interaction.

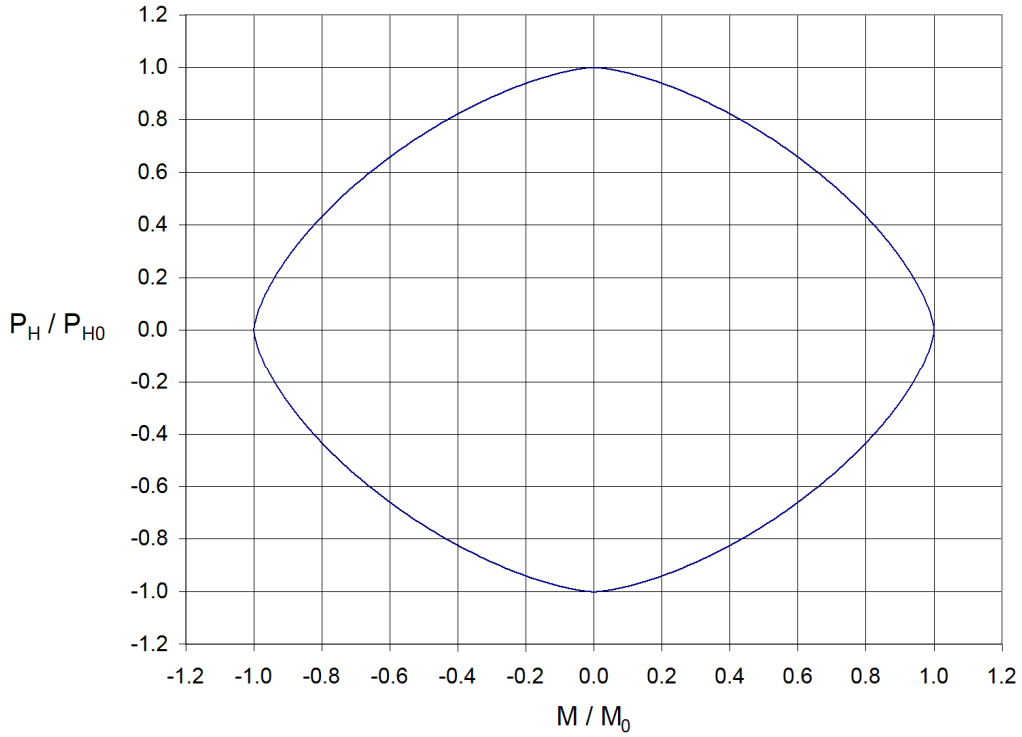

Fig. 3.3 P-M interaction curve of typical infill panel.

Since the attainment of the CP limit state is defined by the maximum displacements (or ductilities) in the IP and OOP directions, it is necessary to postulate interaction relationships for the yield displacements and CP displacements. It seems reasonable to use the same 3/2 power curve for these as well. This is justifiable for the yield displacements, since elastic displacements are proportional to loads. For the CP displacement it is simply a matter of convenience; more research is required to better define the nature of this CP interaction. These relationships, normalized by the unidirectional yield displacements in the respective directions, are shown in Figure 3.4. Note that Δ_H is the IP horizontal displacement, Δ_N is the OOP horizontal displacement, and Δ_{Hy0} and Δ_{Ny0} are their respective yield values at zero load on the opposite direction.

As mentioned previously, the interaction curve marked "CP" is not a property of the present model. Instead, it is invoked in subsequent post-processing of the analytical results. An analysis that shows the calculated displacement vector equaling or exceeding the CP curve will be deemed to have reached the collapse prevention limit state.

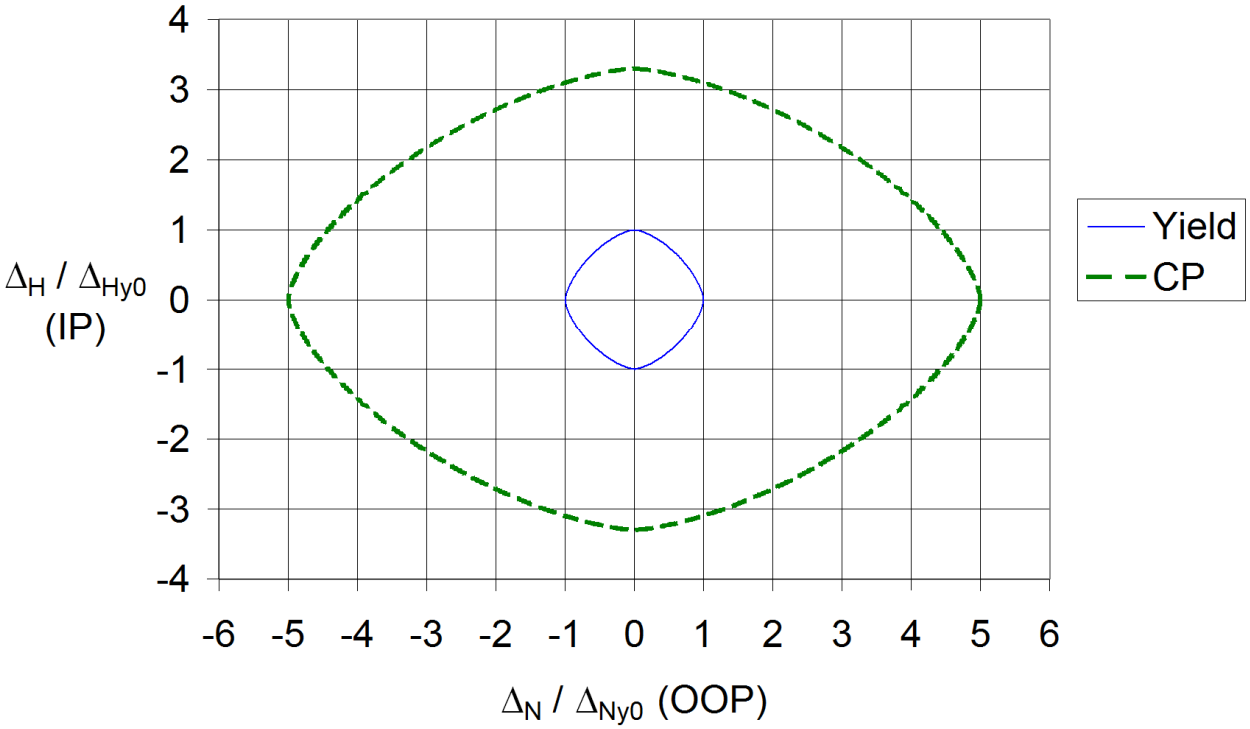

Fig. 3.4 Displacement limit-state interaction curves of typical infill panel.

3.5 DEVELOPMENT OF THE FIBER-SECTION MODEL

The infill model is composed of nonlinear beam-column elements that exist in many nonlinear structural analysis programs such as OpenSees. The nonlinear P-M hinge, which is located at the midspan of the diagonal, is modeled using a fiber section. A schematic layout of the cross section is shown in Figure 3.5. The local z-axis is horizontal, in the OOP direction, normal to the axis of the member, which is the local x-axis. The local y-axis is also normal to the member, and lies in the midplane of the infill wall.

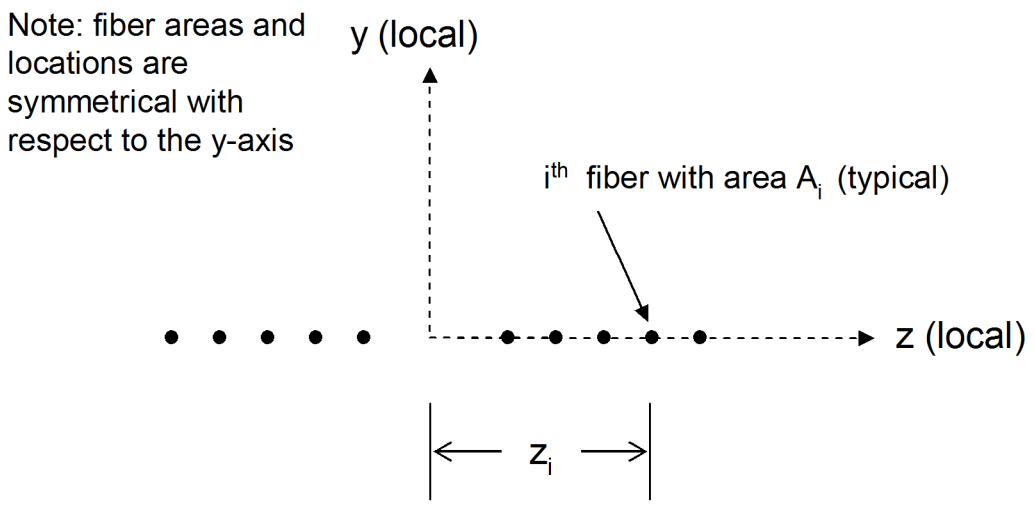

Fig. 3.5 Fiber layout at plastic hinge region.

First, the yield strength and location of each fiber is determined. This calculation is based on the chosen P-M interaction curve for the model (Fig. 3.3), discretized at a finite number of points, as shown in Figure 3.6. Consideration of the changes in the plastic axial force and moment that occur as the plastic neutral axis is "swept through" the section results in the following relationships:

$$F_{yi} = \frac{1}{2}\left[P_j - P_{j+1}\right] \tag{3.7a}$$

$$z_i = \frac{1}{2}\left[\frac{M_{j+1} - M_j}{F_{yi}}\right] \tag{3.7b}$$

where F_{yi} is the yield strength of the ith fiber, P_j is the axial (IP) load for the jth point of the interaction curve ($j = 1$ is taken as P_0, the axial (IP) strength in the absence of applied OOP moment), z_i is the distance of the ith fiber from the centroid of the cross section, and M_j is the OOP moment strength of the cross section for the jth point of the interaction curve ($j = N_{pts}$ is taken as M_0, the bending moment (OOP) strength in the absence of applied IP load).

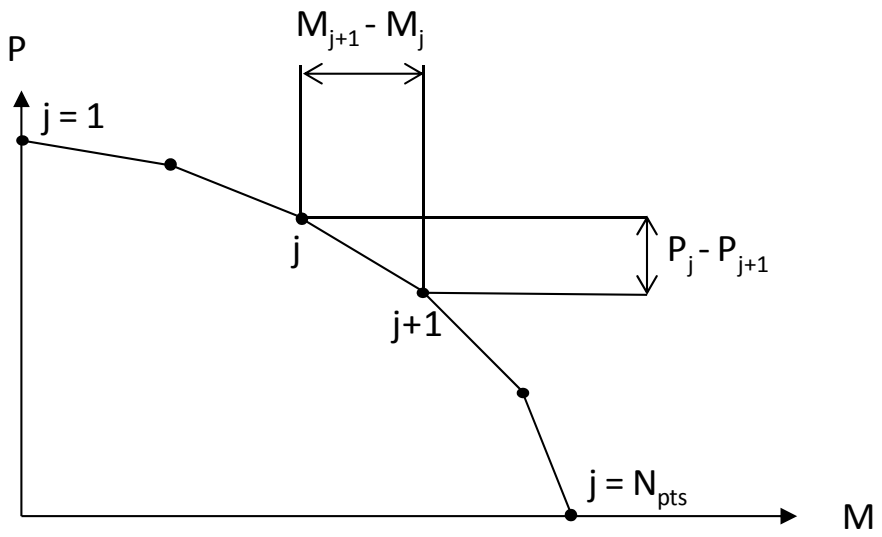

Fig. 3.6 Calculating A_i and z_i.

The yield strength and location for each fiber (i counter) are calculated sequentially for different points on the interaction curve (j counter). These same values are then assigned to the symmetric fibers on the other side of the section centroid. We can obtain a unique cross-section discretization to represent the interaction curve by artificially making the two counters (i and j) identical. In this way, $i = j$, and the total number of fibers in the cross section is equal to $2(N_{pts} - 1)$ where N_{pts} is the number of discrete points used to describe the first quadrant of the interaction curve.

The sequence of calculations just described is the source of the convexity requirement. It is clear that by substituting Equation (3.7a) into Equation (3.7b), a convex relationship between P and M is needed to validate the underlying assumptions in the equations.

Next, it is necessary to calculate the elastic properties of each fiber, i.e., the area and the elastic modulus. It is convenient to take the elastic modulus of all fibers as E_m, the modulus of elasticity of the masonry. As discussed in Section 3.2, this value is taken as 1770 ksi for the case study structure, following Hashemi and Mosalam (2007). With this convenient and identical choice for the elastic moduli of all the fibers, the question of how much area to assign to each fiber becomes an underconstrained problem and hence does not have a unique solution. However, it is required that the areas assigned to the various fibers satisfy the following two conditions:

1. The total area of the cross section must equal the area derived in Section 3.2 based on the elastic axial stiffness, i.e., $A = t_{\text{inf}} \times a$.
2. The section moment of inertia must equal the moment of inertia derived in Section 3.3 based on the OOP stiffness of the model, i.e., I_{eq}.

These requirements may be expressed as follows:

$$\sum_{i=1}^{2(N_{pts}-1)} A_i = t_{\text{inf}} \times a = \text{(67.8 in.}^2\text{ for the case study structure)} \tag{3.8a}$$

$$\sum_{i=1}^{2(N_{pts}-1)} A_i \times z_i^{\,2} = I_{eq} = \text{(3824 in.}^4\text{ for the case study structure)} \tag{3.8b}$$

It is to be noted that while it is tempting to assign a common yield stress f_y to all fibers, and then calculate the area of each fiber as $A_i = F_{yi} / f_y$, this will allow satisfaction of only one of the above conditions. Therefore, the above approach using Equations (3.8) is utilized in this study.

The above two requirements may be satisfied in various ways. One way is to assume a relationship between the fiber area and its distance from the centroid of the cross section. While a linear relationship is the simplest, no valid solution can be found. Instead, it is found that a power law relationship provides reasonable results. Therefore, the above two conditions are augmented by the following relationship (as a postulated form of the solution):

$$A_i = \gamma \times \left| z_i \right|^{\eta} \tag{3.9}$$

where γ and η are constants to be determined such that Equations (3.8) are satisfied. Finally, the yield stress for each fiber is calculated, based on the relationship $f_i = F_{yi} / A_i$, and the fiber yield strain is determined from $\varepsilon_{yi} = f_{yi} / E_m$.

A summary of the fiber properties of the case study structure used in this report is given in Table 3.1. It is to be noted that all the fibers are modeled in OpenSees as "Hardening" material, with a small post-yield modulus (less than 1% of the initial elastic modulus to promote numerical stability; see Fig. 3.19). Thus, the fiber properties are very close to elastic–perfectly plastic material. A summary of the steps used for calculating the properties of the proposed case study model is given in Table 3.2.

Table 3.1 Summary of calculated fiber properties

$i =$ fiber index	$z_i =$ distance from centerline (in)	$A_i =$ area (in.^{2})	$f_{yi} =$ yield stress (ksi)	$\varepsilon_{yi} =$ yield strain
1	19.1	2.44	0.69	0.00039
2	10.0	4.31	0.75	0.00042
3	7.1	5.83	0.78	0.00044
4	5.1	7.73	0.81	0.00046
5	2.7	13.62	0.88	0.00050
6	-2.7	13.62	0.88	0.00050
7	-5.1	7.73	0.81	0.00046
8	-7.1	5.83	0.78	0.00044
9	-10.0	4.31	0.75	0.00042
10	-19.1	2.44	0.69	0.00039
$E_m =$ 1770 ksi (elastic modulus for all fibers)				
$\gamma = 32.273$ in.^{2}		$\eta = -0.875$		

Table 3.2 Summary of calculation steps for infill fiber-section model.

1. Determine the IP axial stiffness and strength of the diagonal member, based on FEMA 356. The ductility that will cause attainment of the Collapse Prevention limit state is also calculated.
2. Calculate the OOP strength of the infill (e.g., in pounds per square foot), based on FEMA 356. Convert this to a bending moment strength at the midheight of the wall assuming a simply-supported vertical span of the infill wall.
3. Calculate the fundamental OOP natural frequency of the infill wall, based on the same assumptions as in Step 2. Also calculate the fundamental modal effective mass (see Appendix D). The modal effective mass is used for assigning the OOP mass of the midspan node of the model.
4. Calculate the required equivalent OOP moment of inertia of the diagonal beam-column elements, based on the principle that the OOP frequencies of the actual wall and the model must be equal. A nominal value, less than 1% of the OOP bending stiffness, is used for the IP bending stiffness, in order to provide numerical stability.

5. Calculate the OOP moment strength of the diagonal beam-column elements of the model, such that the model will experience incipient yielding at the same level of support motion as the actual infill wall panel (see Appendix D).
6. Steps (1) and (5) have determined the axial strength and bending strength of the diagonal member without considering interaction. These values are used as the "anchors" for the chosen interaction relationship.
7. Given the full interaction relationship, which is described by its anchors and its chosen shape (at a discrete number of points), the values of the individual fiber strengths, as well as their distances from the centroid, may be calculated, using Equations 3.7. The number of fibers used in the cross section is a function of the number of points in the discretized interaction shape.
8. For a chosen value of fiber elastic modulus (common to all fibers), the required total area of fibers is calculated based on the required axial stiffness (see Step (1)). Similarly, the required moment of inertia is calculated, based on the equivalent moment of inertia (Step 4). Using a chosen relationship between individual fiber area and distance from the centroid (e.g., Equation (3.9)), the area of each individual fiber is calculated.
9. Knowing the required strength of each fiber from Step (7) and the area from Step (8), the yield stress of each fiber may be calculated. The material is assumed to be elastoplastic, with a small post-yield stiffness to ensure numerical stability.
10. The location, area, elastic modulus, and yield stress of each fiber are now known. The fiber section is finally assembled using this information and standard procedures in many structural analysis programs such as OpenSees.

3.6 PERFORMANCE OF THE PROPOSED FIBER-SECTION MODEL

In order to verify the performance of the proposed fiber section, a model similar to that shown in Figure 3.1 is created using OpenSees (Mazzoni et al. 2006). Dimensions and properties are given in Appendix E. The diagonal strut is modeled using two "Beam With Hinges" elements. The ends of the elements connected to the midspan node are represented by the nonlinear fiber section discussed in Section 3.5. The total hinge length (sum of the lengths of the hinges on both sides of the node) is taken as 1/10 of the total length of the diagonal. This length is chosen to be as short as possible in order to minimize the effect of sequential yielding of the fibers (i.e., to produce a relatively sharp yield point for the element), while at the same time providing a numerically stable solution. The central portions of the "Beams With Hinges" are elastic, and are assigned the elastic area and moment of inertia described previously. The ends of the elements that are attached to the surrounding frame are modeled as elastic hinges, and so are modeled with the normal elastic area, but with artificially low moments of inertia (0.001 $in.^4$). The analysis is based on an assumption of small displacements.

First, the model is analyzed for static pushover, applying a fixed static force in the OOP direction, then performing a displacement-controlled pushover analysis in the IP direction. An example result from this type of analysis is given in Figures 3.7–3.9. For the shown case, an OOP static force of 3 kips is applied to the model, which is then pushed in the IP direction under IP displacement control. Figure 3.7 shows the resulting pushover curve, i.e., IP shear force versus IP horizontal displacement. Figure 3.8 shows the corresponding path on the P-M diagram. Note that, as anticipated, the path does not exceed the prescribed interaction boundary. This is, of course, a consequence of the methodology of choosing the strength of the section fibers, as derived above. Finally, Figure 3.9 shows the path of the displacements, normalized by the respective unidirectional yield displacements. As clearly observed, the shape of the displacement path is similar to that of the P-M path while the fibers are elastic; after crossing the yield surface the path bends more sharply. For the shown case, the displacement path also crosses the outer interaction surface, indicating that the infill wall has reached the CP limit state.

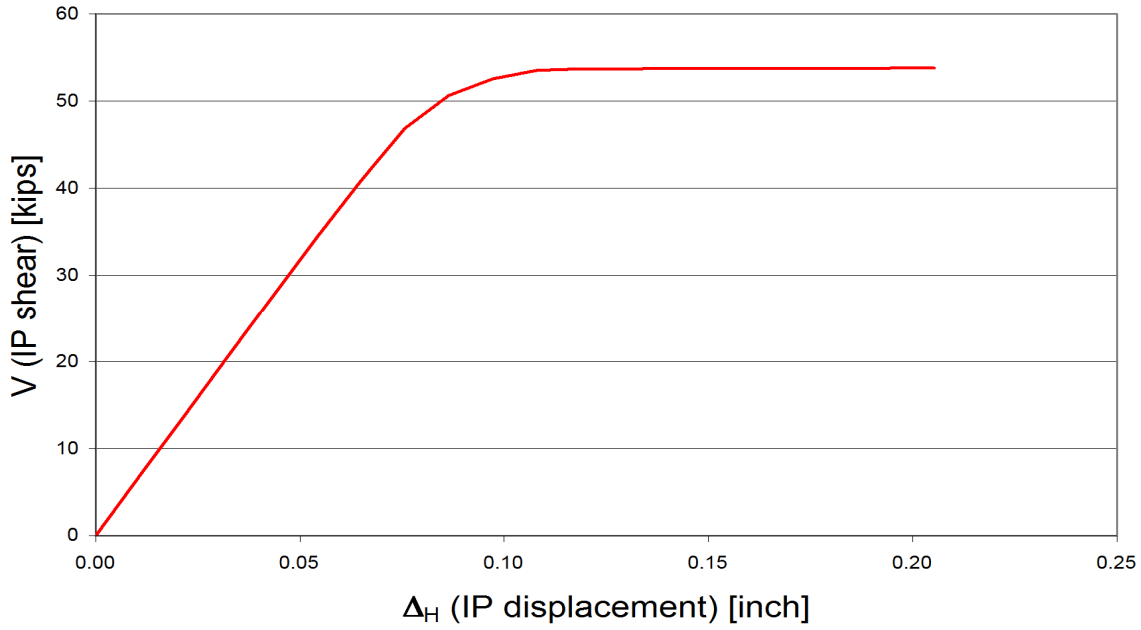

Fig. 3.7 In-plane pushover curve with $P_N = 3$ kips.

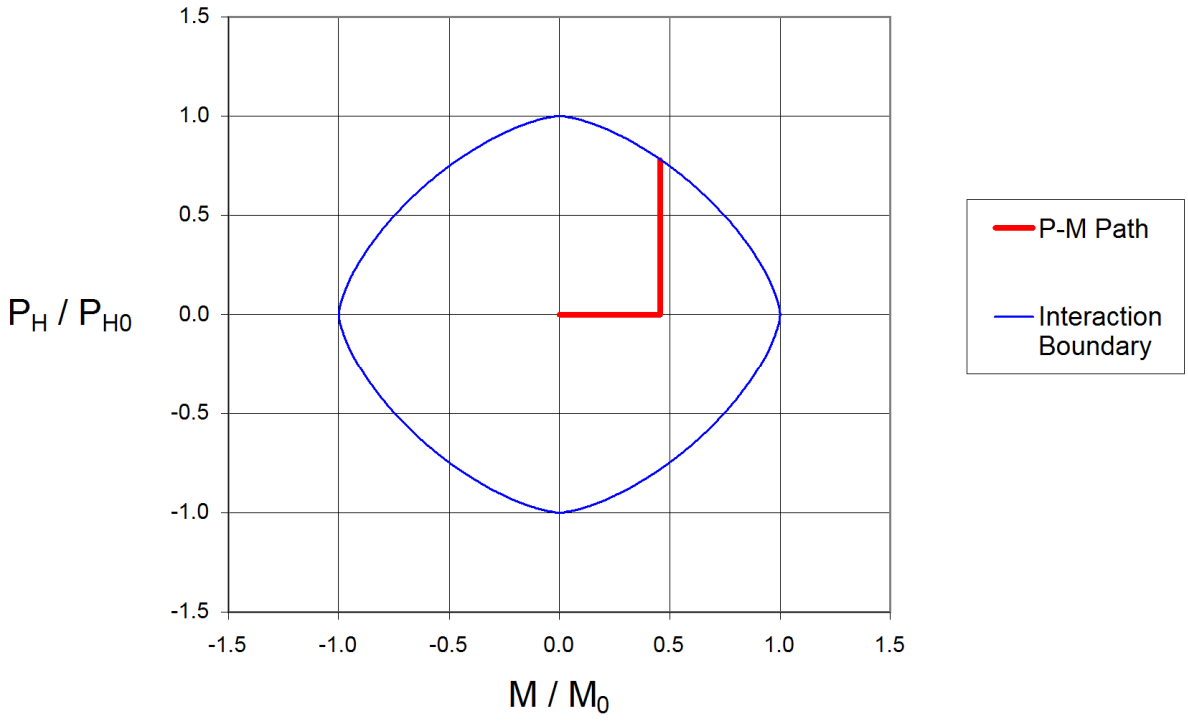

Fig. 3.8 P-M path from pushover analysis with $P_N = 3$ kips.

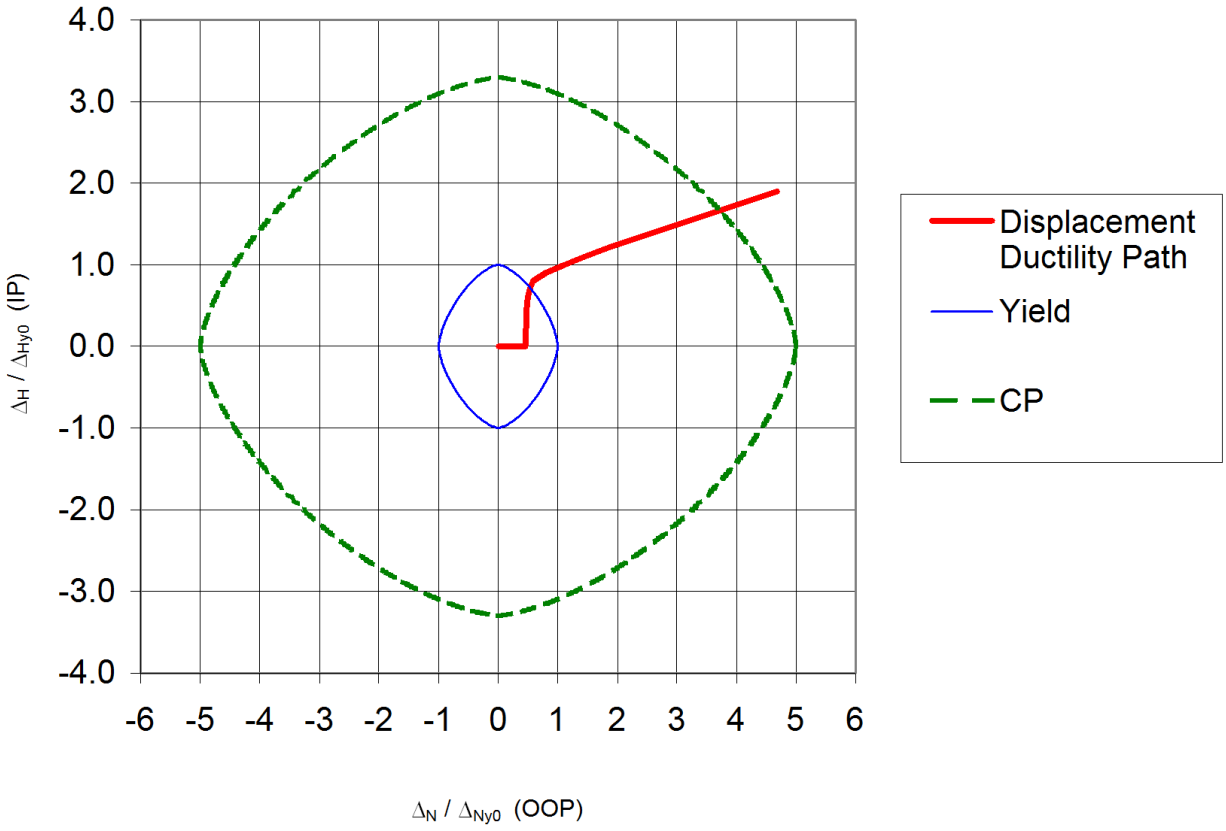

Fig. 3.9 Displacement path from pushover analysis with $P_N = 3$ kips.

Next, the model is utilized for a cyclic pushover analysis. In this case, both the IP and OOP displacements are prescribed (i.e., this is a fiber-section controlled analysis). The displacement loading regime is shown in Figure 3.10. As observed, both IP and OOP displacements are cycled in phase. The same information is presented, in different form, in Figure 3.11, which shows the prescribed displacement path on the $\Delta_H - \Delta_N$ plane. Figure 3.12 presents the response path in the P-M plane. Note that although the displacements trace a straight line after crossing the yield interaction curve (as prescribed by the displacement control regime), the P-M path, rather than simply stopping at the interaction curve, changes direction and runs along the interaction curve. It is believed that this behavior is due to the fact that the location of the fully plastic neutral axis within the cross section is different from that of the elastic neutral axis, thus changing the P/M ratio as it shifts during loading. Eventually, the P-M path stops moving along the interaction curve, as seen in Figure 3.13 (the IP hysteresis curve) and in Figure 3.14 (the OOP hysteresis curve), in the regions where the P and M curves are horizontal (constant). The P and M values do not leave this point until displacement unloading occurs.

This movement along the interaction curve also explains why the two hysteresis curves deviate from an elastic–perfectly plastic (EPP) shape, despite the fact that the fiber material itself is EPP. The implications of this non-ideal hysteresis shape from an energy-dissipation point of view are discussed in Section 3.7.

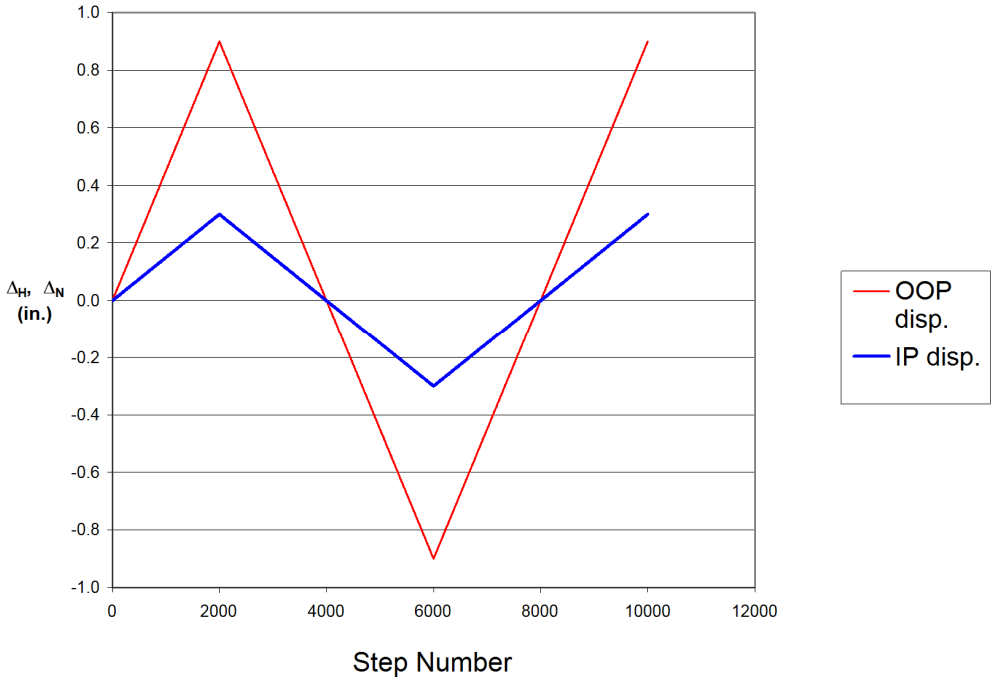

Fig. 3.10 Displacement-controlled load regime.

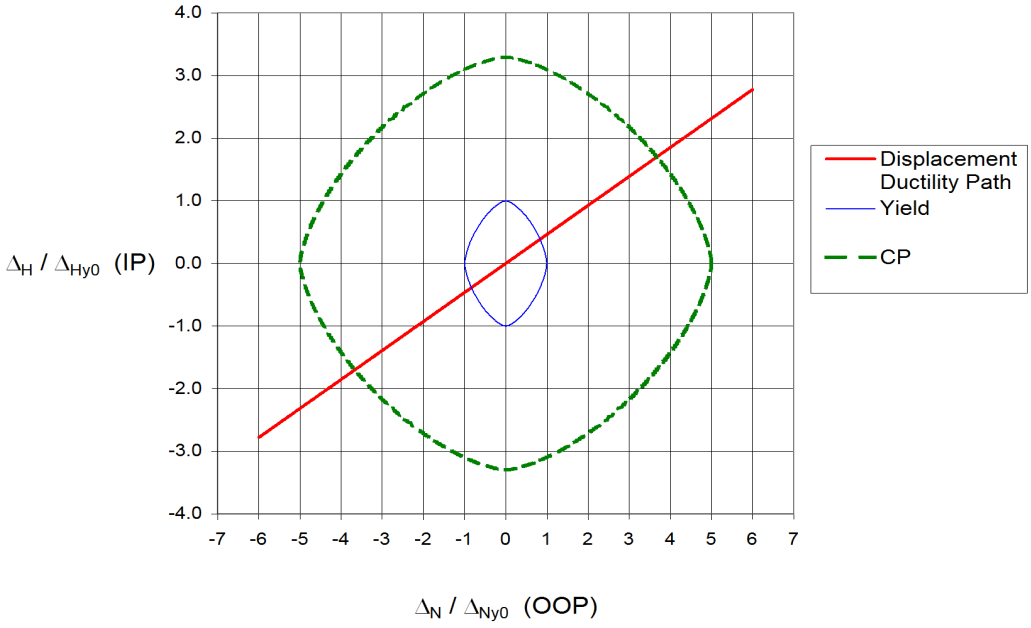

Fig. 3.11 Displacement path from pushover analysis with double displacement control.

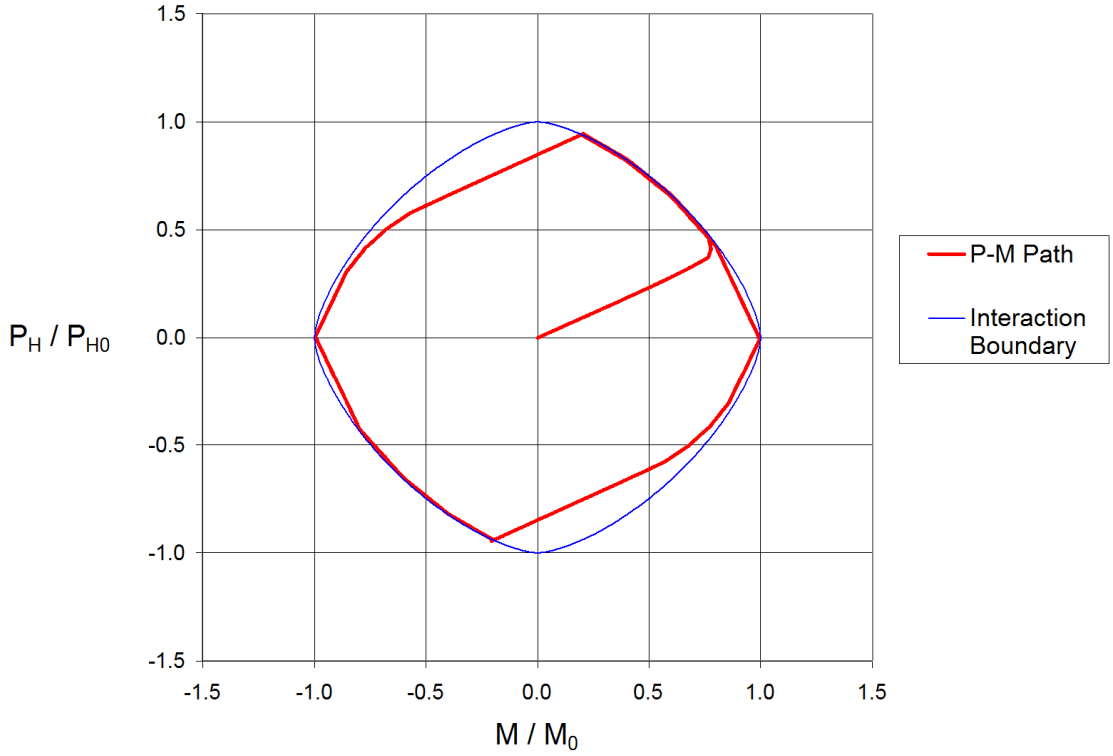

Fig. 3.12 P-M path from pushover analysis with double displacement control.

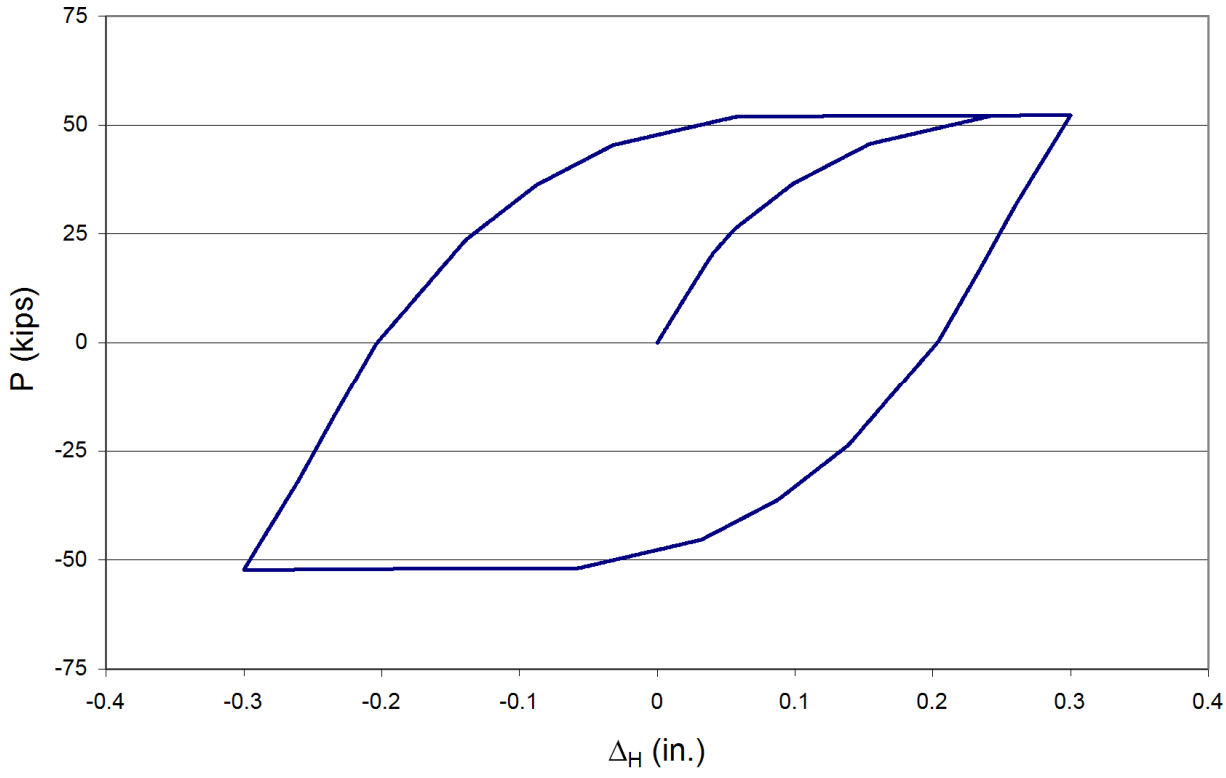

Fig. 3.13 P versus Δ_H from pushover analysis with double displacement control.

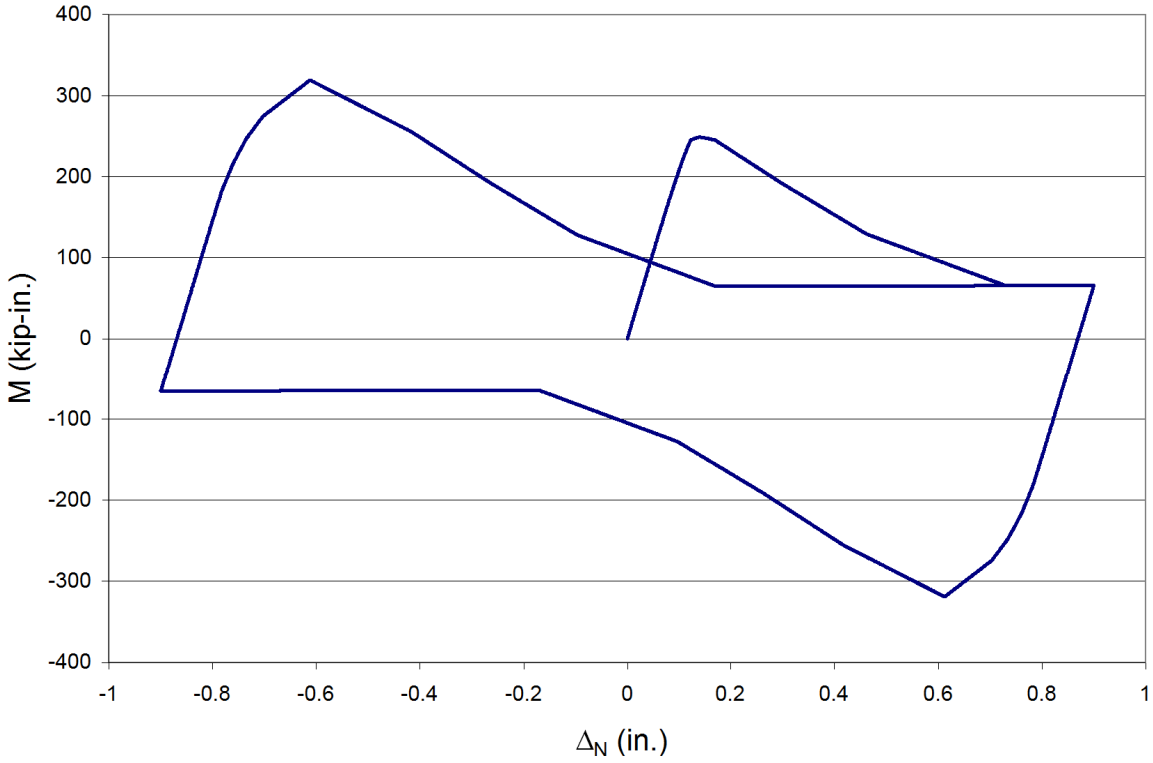

Fig. 3.14 M versus Δ_N from pushover analysis with double displacement control.

Finally, a simple dynamic base-excitation analysis is performed. For this case the static model is modified by adding an IP horizontal mass at the upper node, as well as the OOP mass at the midspan node (see Fig. 3.15). The IP mass is sized to provide an IP natural frequency of 4 Hz, to approximate the frequency of the five-story building investigated by Hashemi and Mosalam (2007), since that structure will be used in the example analysis conducted in Chapter 4. Further discussion about the five-story building model is provided in that chapter. The upper node is restrained from motion in the OOP direction, while the lower node is restrained in all directions. An earthquake time history is applied to the restrained degrees of freedom in both the IP and OOP translational directions. The chosen time history is that of the Coyote Lake Dam (CL_clyd, see Table 4.1). The longitudinal time history component is applied in both the x- and y-directions. These time history components are scaled such that the peak accelerations are 0.10g in the x-direction and 1.9g in the y-direction. These values are chosen after several trials to illustrate the full range of the P-M interaction relationship for the considered case study structure. It is recognized that this method of applying base accelerations is not realistic; for more realistic analyses, see Chapter 4.

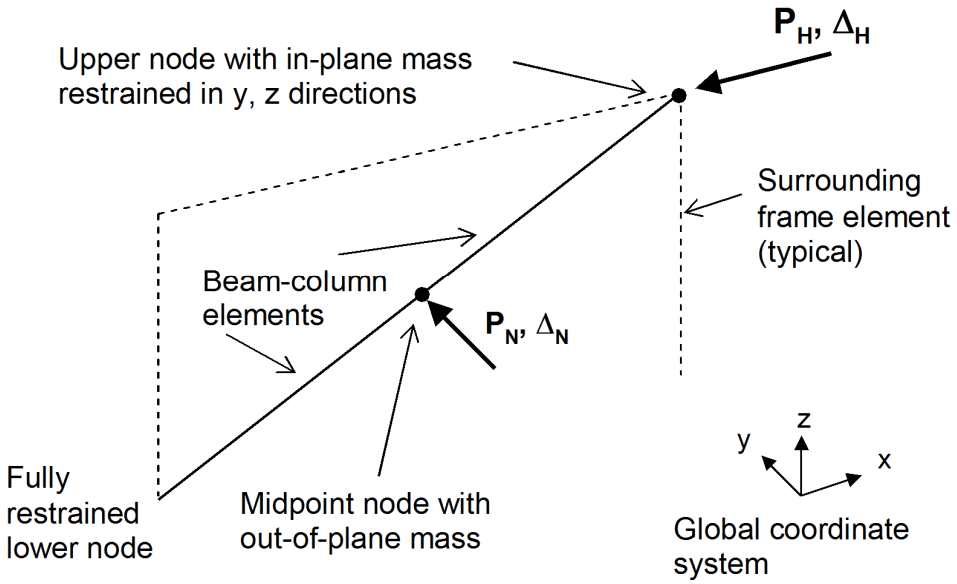

Fig. 3.15 Dynamic model of infill panel.

Figure 3.16 presents the IP and OOP displacement responses as a function of time, while Figure 3.17 shows the same information on the $\Delta_H - \Delta_N$ plane. It should be noted that the $\Delta_H - \Delta_N$ path crosses the CP interaction curve, and therefore the wall has exceeded the CP limit state. Moreover, significant residual OOP displacement is observed from the time history plots of Figure 3.16. This residual displacement is about 50% of the peak OOP displacement. The P-M response path is shown in Figure 3.18. As intended, the values of axial force and moment do not exceed the envelope interaction curve. The stress-strain response path of the inner fiber is presented in Figure 3.19.

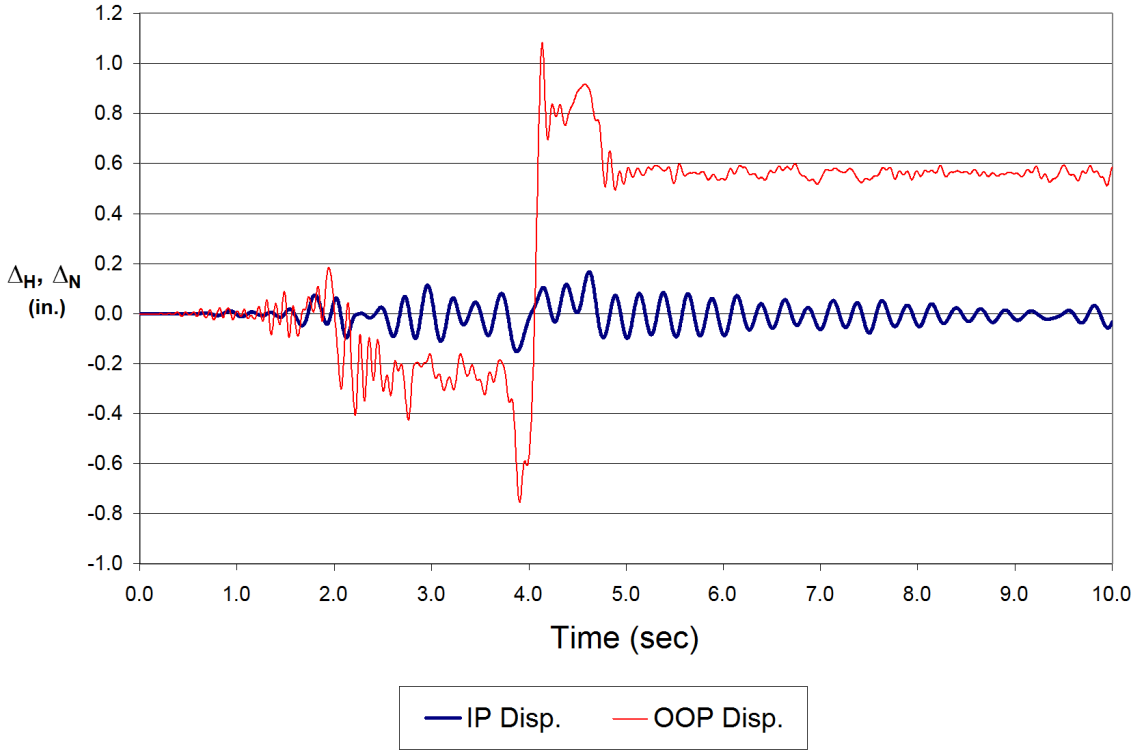

Fig. 3.16 IP and OOP displacements from time history analysis.

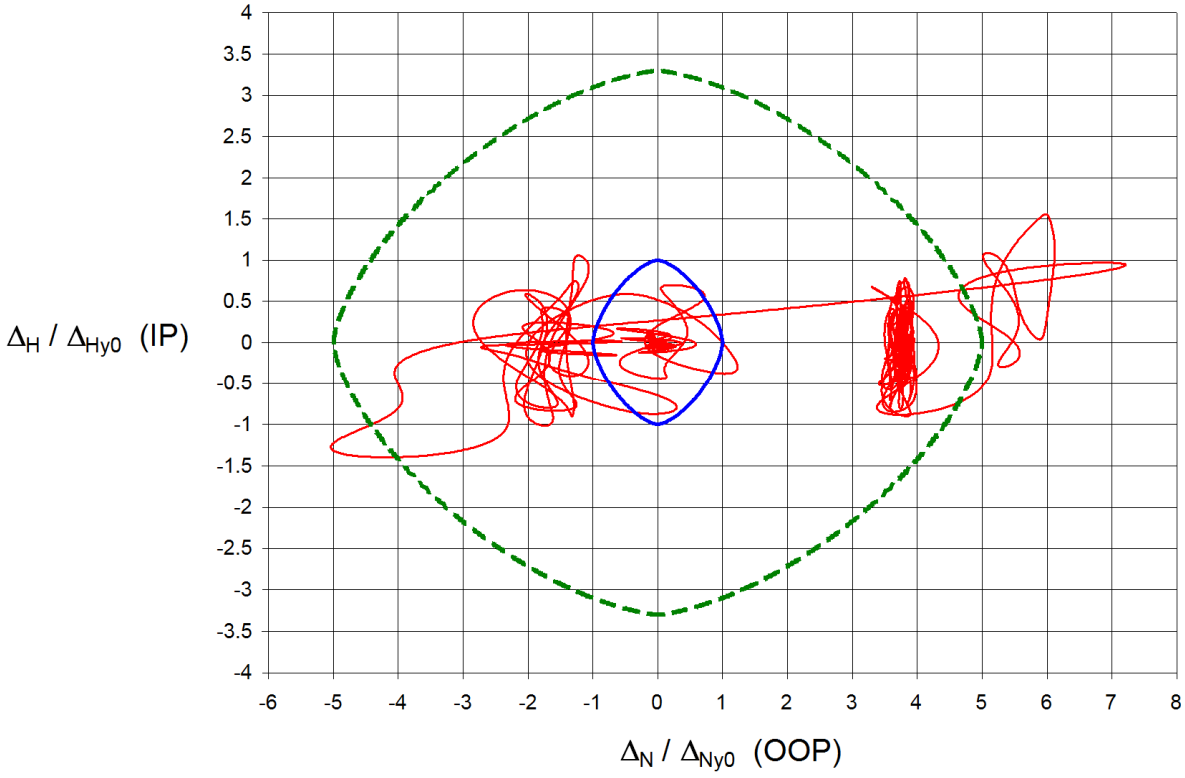

Fig. 3.17 Displacement response path from time history analysis.

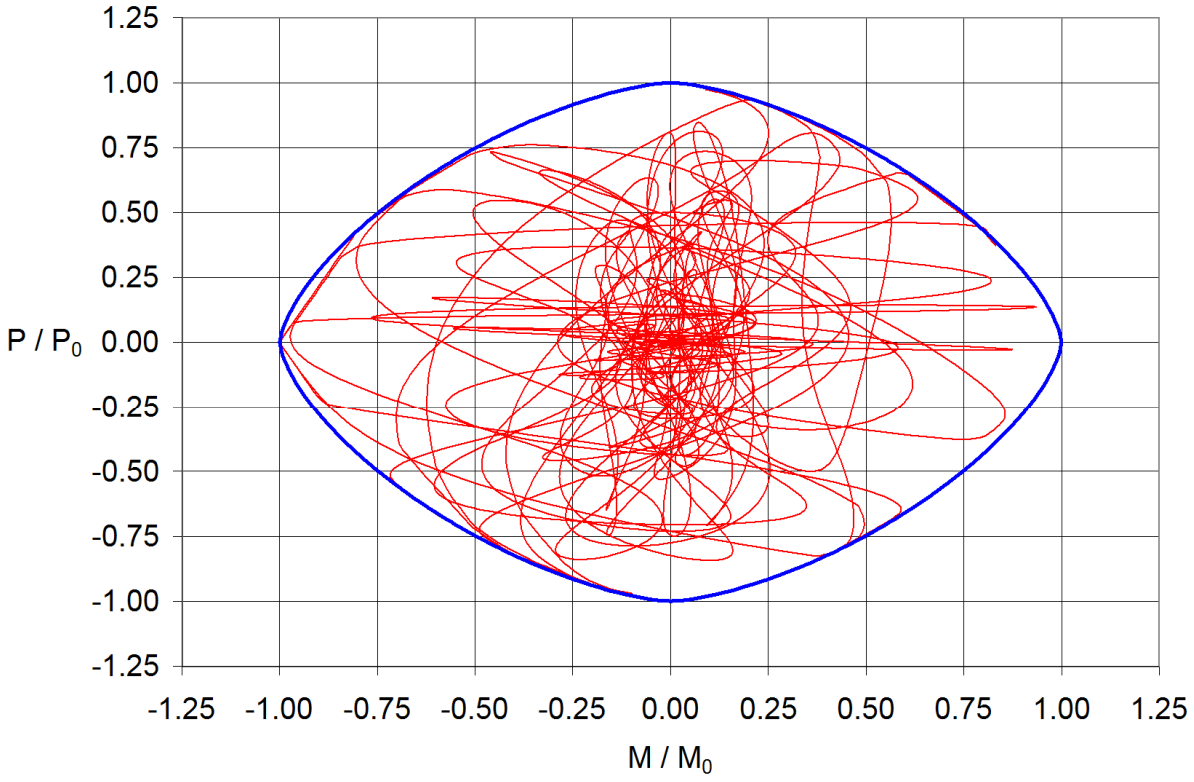

Fig. 3.18 P-M path from time history analysis.

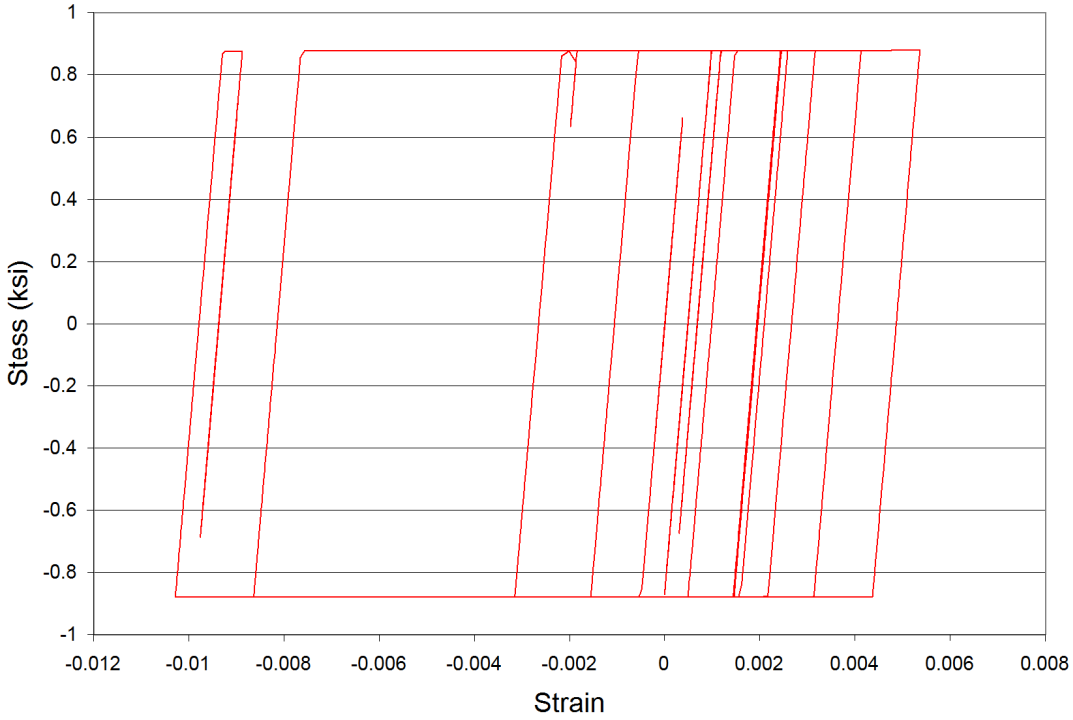

Fig. 3.19 Inner fiber stress-strain path from time history analysis.

3.7 SUMMARY OF OBSERVATIONS AND COMMENTS

Based on the results of the preceding section, it is concluded that the proposed fiber-section model generally meets the goals set out in Section 3.1. The simple one-bay, one-story model reproduces the elastic properties of the infill panel in the elastic range. In the nonlinear range, the model produces axial force and moment that conform to the prescribed interaction relationship. However, there are several aspects of the model that deserve closer inspection.

One problem stems from the fact that the model cannot attain the goal of an ideally "sharp" yield point for all loading paths, despite the fact that the individual fibers themselves are EPP. This is clear from Table 3.1, which lists the yield stresses of the fibers. If, for instance, the model experiences pure axial load, the outer fibers will yield first, followed progressively by the fibers closer to the centroid of the section. This will also be the case if the model is loaded with pure OOP moment. A consequence of this non-sharp, "distributed" yielding is that some fibers experience yielding before the displacements reach the so-called "yield" surface shown on the displacement paths (see Fig. 3.9), or before the axial force and OOP moment reach the interaction surface. This, in turn, will produce some unwanted hysteretic damping at displacements below "yield."

The yield under pure axial load will be sharp if all the fibers have equal yield stress; the yield for pure moment will be sharp if the yield stress varies linearly with distance from the centroid. Since it is not possible to satisfy both of these requirements simultaneously, it may be that the optimal model is some linear combination of these requirements, where the yield stresses are adjusted to minimize the unwanted damping. The fiber areas must then be changed, in order that the total strength (in kips) of each fiber remains unchanged. The change in area will then affect the elastic-range properties of the nonlinear hinge region, but the linear elastic region of the element can then be modified to preserve the correct overall elastic stiffness of the model. It should be noted that a sharp yield point does not necessarily represent the behavior of an actual infill wall. However, the inability to have full control over the sharpness of the yield point must still be viewed as a drawback in the context of the proposed model.

Next, there is some question about whether the post-yield behavior of the proposed model can accurately reflect the inelastic behavior of the actual infill wall. This is illustrated by the hysteresis curves in Figures 3.13 and 3.14. It is noted, for instance, that the moment drops after yielding, while the axial force increases. This is a consequence of the fact that the plastic neutral

axis does not have the same location in the fiber section as the elastic neutral axis. It is not clear that this model behavior reflects the behavior of the actual infill. It has been pointed out in (Sharif et al. 2007) that in fact the resisting moment of the infill decreases with increasing displacement. However, this effect is fortuitous here, since the model does not consider the large displacements that are the cause of this behavior. Finally, it may be possible to modify the post-yield properties of the fibers in order to produce post-yield model behavior closer to experimentally observed behavior.

Another more serious objection stems from the fact that the model IP axial and OOP moment strengths do not drop to zero when the CP limit state interaction curve is exceeded. In the actual structure, the collapse of an element is accompanied by an increase of load in neighboring elements. They, in turn, may experience increased displacements, and reach CP themselves. This effect will not be captured with the proposed model where the collapse of the element by reaching the CP limit is determined in post-processing. This may not be a problem if the design engineer intends to redesign or retrofit the walls where collapse is predicted, thus preserving their ability to carry load. However, if the objective of the analysis is a performance-based evaluation of an existing structure, the use of the proposed model may lead to unrealistically optimistic conclusions.

One crude yet (probably) conservative remedy for the problem discussed in the previous paragraph is to simply remove the "collapsed" infill panel elements, rerun the analysis, remove the collapsed panels from the new analysis, and repeat this process until no more panels collapse or until there is a global collapse of the structure. A more realistic, although more difficult, solution would be to modify the analysis program so that it removes the collapsed elements, when they collapse, and then proceeds with the analysis without interruption. This method of direct element removal has been proposed by Talaat and Mosalam (2008). Again, it may be possible to adjust the stress-strain properties of the fibers, as discussed above for post-yield behavior, so that the post-collapse behavior may be simulated, at least in an approximate fashion.

It should also be pointed out that, for the case of an infill wall, the question of detailed post-yield behavior may not be of paramount importance. Given the high natural frequency of the wall relative to the input seismic motion at its supports, it would be expected that the wall would experience large OOP inelastic displacement, as soon as the input motion exceeds the yield level by a small amount (Chopra 2005). Thus, the level of support spectral acceleration causing the wall to reach the CP limit state is not expected to be much higher than the level

causing yielding. Since the yield state is predicted well by the interaction relationship, the error in acceleration level for the CP state is not expected to be significant, at least for the first few walls to reach the CP state.

4 Example Analysis Using Proposed Infill Model

In order to demonstrate its behavior and capabilities, the infill model proposed in Chapter 3 is incorporated into a larger model of a five-story reinforced concrete (RC) frame building with unreinforced masonry (URM) infill walls. This model is then subjected to seismic base excitation, using 20 sets of ground motion, at five different levels of spectral acceleration. The global responses of the structure are determined, along with the local responses of the individual infill panels. Next, fragility functions are calculated, giving the probability that the individual panels will reach the so-called "collapse prevention" (CP) limit state as a function of the spectral acceleration level. Fragility functions are also derived for a global response, the interstory drift ratio (IDR). Complete details of the building model and the input ground motions may be found in Hashemi and Mosalam (2007).

4.1 DESCRIPTION OF BUILDING MODEL AND INPUT MOTIONS

The building model used in this chapter is derived from the model previously used in the collaborative program of investigations into RC frames with URM infill, discussed in Chapter 1. The model is illustrated in Figure 4.1. The prototype building is a RC frame, five stories in height, with three bays in the x-direction and two bays in the y-direction. The central column line running in the x-direction (Column Line B) has URM infill panels in all bays at all levels. Thus, the x-direction is designated as the "longitudinal" direction. In the model of Hashemi and Mosalam (2007), each infill panel was modeled with two members, one on each diagonal. Each member was a compression-only elastic strut. The RC frame was modeled using nonlinear, force-based, beam-column elements. For this report, the diagonal members representing the infill panels are replaced with the infill model developed in Chapter 3. One diagonal beam-column with two elements is located in each panel (see Fig. 4.2). As discussed in Chapter 3, these diagonal elements reproduce the IP force-displacement relationship (in both the positive and

negative x-directions), as well as the OOP force-displacement relationship, with the interaction between the IP and OOP responses also considered. The stiffness of the infill model elements is adjusted so that the periods of the fundamental modes of vibration of the building in the longitudinal and transverse directions match those obtained by Hashemi and Mosalam (2007), i.e., 0.24 and 0.35 sec, respectively. The properties of the infill members are the same as those used in Chapter 3, and the calculation of their properties is given in Appendix E.

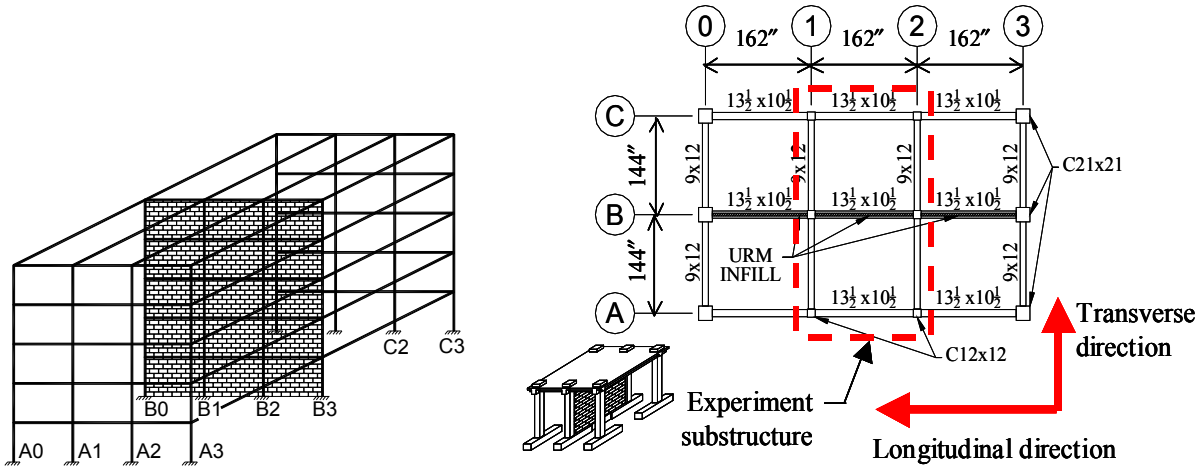

Fig. 4.1 Building model (Hashemi and Mosalam 2007).

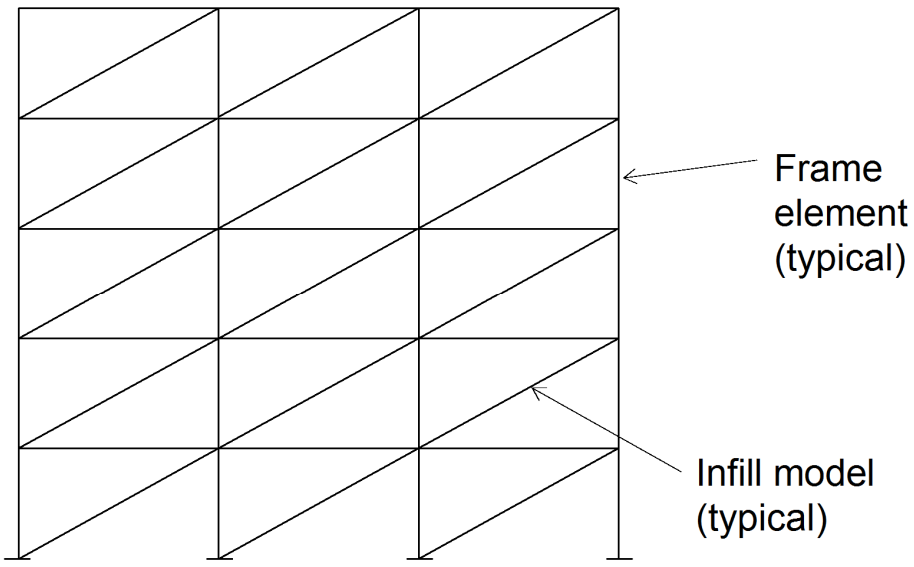

Fig. 4.2 Elevation of column line B, showing arrangement of proposed infill models within building frame.

The seismic analysis of the model is performed using OpenSees (Mazzoni et al. 2006). The input base motion consists of 20 sets of recorded time histories used in a previous study (Lee and Mosalam 2006), each set consisting of one time history in the longitudinal direction and one in the transverse direction. The ground motions are listed in Table 4.1. These motions are then scaled so that their spectral accelerations, *Sa*, at the fundamental periods in each direction of the building model are set to five values: 0.50g, 1.00g, 1.61g (10/50), 2.05g (5/50), and 2.75g (2/50). The designation "1.61g (10/50)," for example, indicates that there is a 10% chance that the spectral acceleration will equal or exceed 1.61g during a period of 50 years. As an illustration, the scaled response spectra for the *Sa* = 1.61g level are shown in Figure 4.3. Thus, for this part of the investigation, the building is analyzed for 20 time history sets at five spectral accelerations values, for a total of 100 analyses.

Table 4.1 Ground motion characteristics for life science addition (LSA) PEER testbed study (Lee and Mosalam 2006).

Earthquake	Mw	Station	Designation	Distance	Site
Coyote Lake, 1979/6/8	5.7	Coyote Lake Dam abutment	CL-clyd	4.0 km	C
		Gilroy #6	CL-gil6	1.2 km	C
Erzincan, Turkey, 1992/3/13	6.7	Erzincan	EZ-erzi	1.8 km	C
Kobe, Japan, 1995/1/17	6.9	Kobe JMA	KB-kobj	0.5 km	C
Loma Prieta, 1989/10/17	7.0	Corralitos	LP-cor	3.4 km	C
		Gavilan College	LP-gav	9.5 km	C
		Gilroy historic	LP-gilb		C
		Lexington Dam abutment	LP-lex1	6.3 km	C
		Los Gatos Presentation Center	LP-lgpc	3.5 km	C
		Saratoga Aloha Ave	LP-srtg	8.3 km	C
Livermore, 1980/1/27	5.5	Fagundes Ranch	LV-fgnr	4.1 km	D
		Morgan Territory Park	LV-mgnp	8.1 km	C
Morgan Hill, 1984/4/24	6.2	Anderson Dam Downstream	MH-andd	4.5 km	C
		Coyote Lake Dam abutment	MH-clyd	0.1 km	C
		Halls Valley	MH-hall	2.5 km	C
Parkfield, 1966/6/27	6.0	Array #5	PF-cs05	3.7 km	D
		Array #8	PF-cs08	8.0 km	D
		Temblor	PF-temb	4.4 km	C
Tottori, Japan, 2000/10/6	6.6	Kofu	TO-ttr007	10.0 km	C
		Hino	TO-ttrh02	1.0 km	C

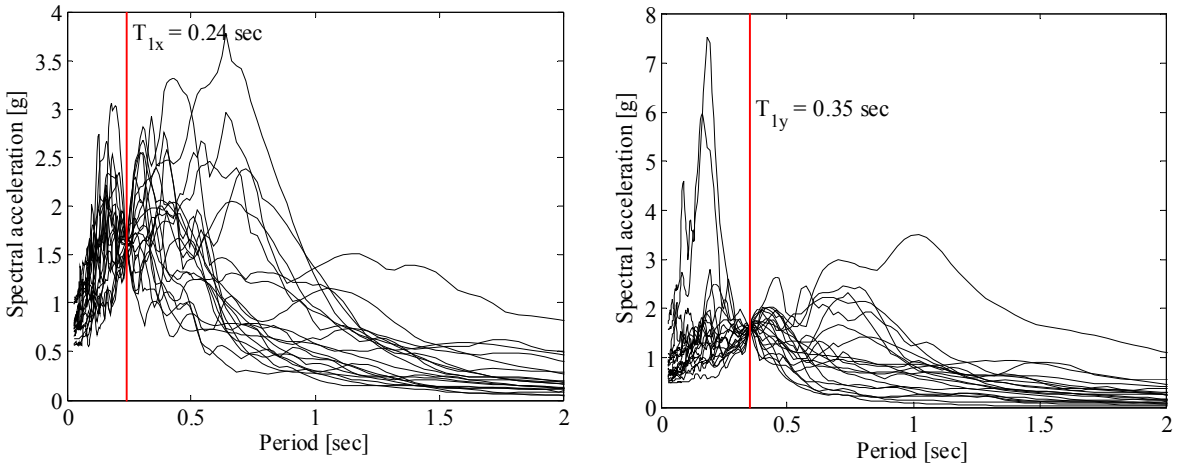

(a) Longitudinal direction (b) Transverse direction

Fig. 4.3 Scaled earthquake spectra for Sa = 1.61g (Hashemi and Mosalam 2007).

4.2 DISCUSSION OF ANALYSIS RESULTS

The 100 analysis cases described above are carried out, with floor level displacements and accelerations in the longitudinal and transverse directions recorded as measures of the global response of the building model. In addition, infill model response parameters (IP axial force, OOP moment, IP and OOP relative displacements, and fiber stresses) are recorded for the middle bay of the first, third, and fifth story, to serve as sample local responses of these infill panels. These locations give responses that cover most of the possibilities of typical infill responses for the building as a whole. Had this been an actual design calculation, it would be necessary to verify that the chosen locations are the critical ones.

As an example of the results obtained from the 100 analyses, Figure 4.4 shows the longitudinal displacement response for the roof, relative to the ground, from the analysis for the Coyote Lake earthquake, CL-gil6 (see Table 4.1), with *Sa* = 1.0g. For the same analysis case, the IP and OOP displacement deformations of the infill panel at the center bay of the first story are given in Figures 4.5 and 4.6, respectively. For reference, the unidirectional yield deformations are 0.11 inch for IP, and 0.15 inch for OOP. The deformations are calculated by the following formulas:

$$\Delta_N = u_{y\_mid} - \frac{\left(u_{y\_top} + u_{y\_bot}\right)}{2} \tag{4.1}$$

where

$\Delta_N =$ OOP deformation of the infill panel, calculated at each time step

$u_{y\_mid} =$ y-direction (OOP horizontal) deflection of the midheight node of the infill element, relative to ground

$u_{y\_top} =$ y-direction deflection of the top node of the infill element, relative to ground

$u_{y\_bot} =$ y-direction deflection of the bottom node of the infill element, relative to ground

$$\Delta_H = \left(u_{x\_top} - u_{x\_bot}\right) - \frac{h_{col}}{L_{col}}\left(u_{z\_bot} - u_{z\_top}\right) \tag{4.2}$$

where

$\Delta_H =$ IP deformation of the infill panel, calculated at each time step

$u_{x\_top} =$ x-direction (IP horizontal) deflection of the top node of the infill element, relative to ground

$u_{x\_bot} =$ x-direction deflection of the bottom node of the infill element, relative to ground

$u_{z\_top} =$ z-direction (IP vertical) deflection of the top node of the infill element, relative to ground

$u_{z\_bot} =$ z-direction (IP vertical) deflection of the bottom node of the infill element, relative to ground

$h_{col} =$ The column height between beam centerlines

$L_{col} =$ Horizontal distance between column lines

The second term in Equation (4.2) results from the fact that a rigid body rotation of the diagonal does not change its length, and the purpose of the Δ_H parameter in this instance is to serve as a measure of the diagonal deformation. Figure 4.7 shows the deformation path of Δ_H and Δ_N, normalized by their respective unidirectional yield values, and plotted on the same plane. These results are also obtained from the example time history analysis of CL-gil6 ground motion (Table 4.1) scaled to *Sa* = 1.0g. The yield and the CP limit state boundaries are also included (see Chapter 3 for a discussion of the limit states). Since the deformation path crosses the CP boundary, this plot of the normalized deformation path indicates that the infill panel will exceed the CP limit state. Based on the same time history analysis used for Figure 4.7, the IP axial force and OOP moment path in the infill model is shown in Figure 4.8. In this figure the axial force and OOP moment are normalized by their unidirectional plastic capacities. Note that the force and moment do not exceed the bounds of the P-M interaction diagram (as expected and

discussed in Chapter 3 during the derivation of the model), and that the axial force dominates the behavior.

An interesting result may be observed in these figures. The permanent, residual inelastic displacement is more prominent for the OOP direction than the IP direction, despite the fact that the force–moment path touches the yield surface near the pure axial force vertex. This behavior is attributed to the fact that there is significant IP structural redundancy provided by the RC moment frame (which is seismically designed as discussed by Hashemi and Mosalam (2007)), which prevents the IP displacements from increasing rapidly after yield. In the OOP direction, however, there is no redundancy, and inelastic displacements are resisted only by the inelastic OOP moment, which has been reduced by the interaction effects. This causes the OOP displacements to increase rapidly after yield.

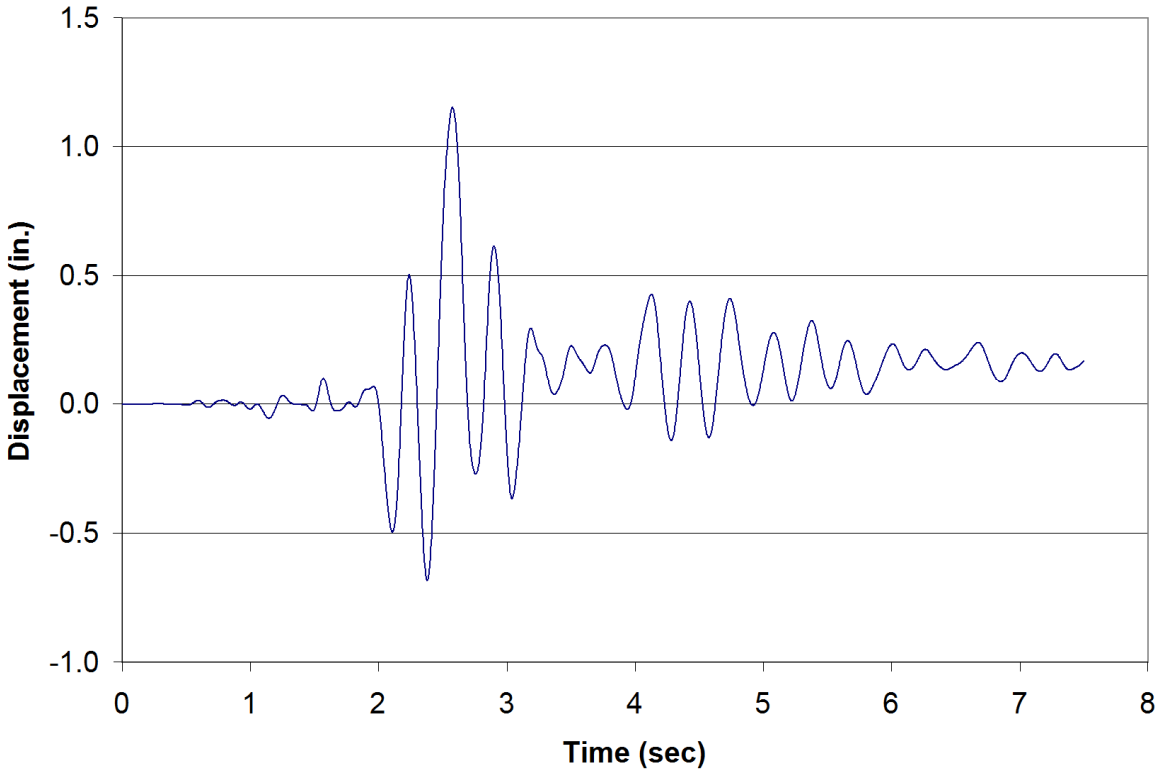

Fig. 4.4 Longitudinal displacement of roof relative to ground.

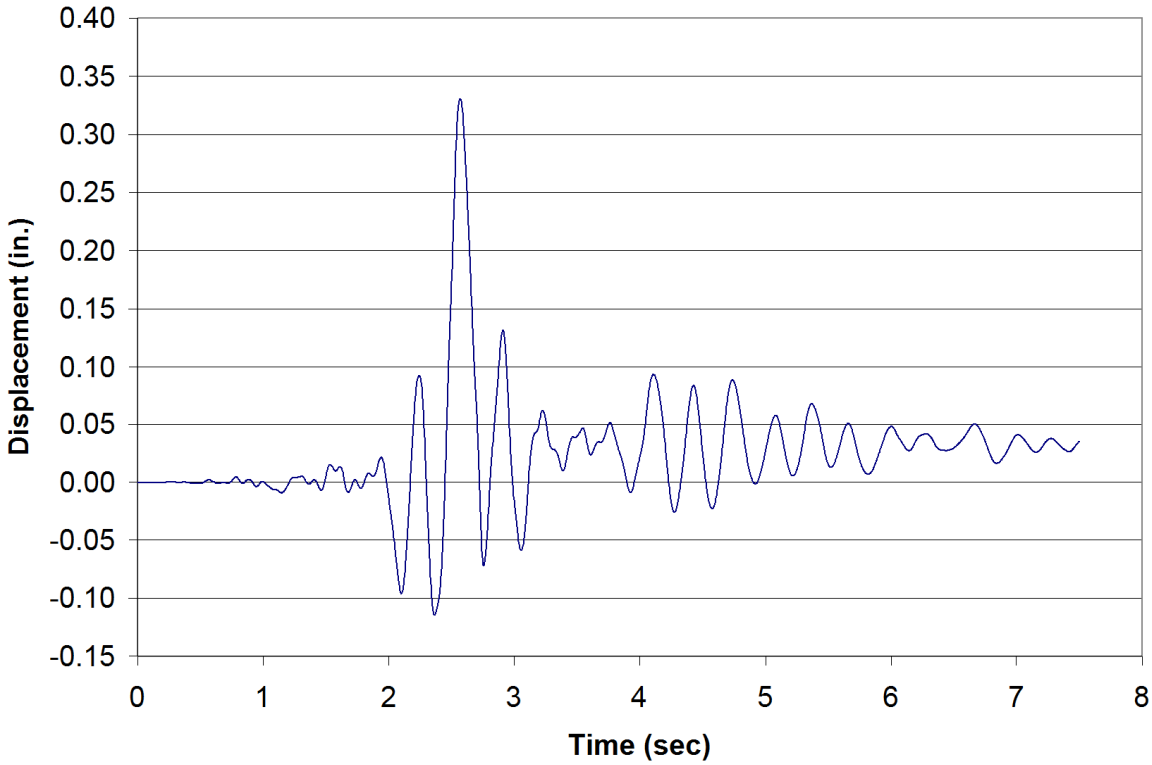

Fig. 4.5 IP deformation, Δ_H, time history for first-story infill.

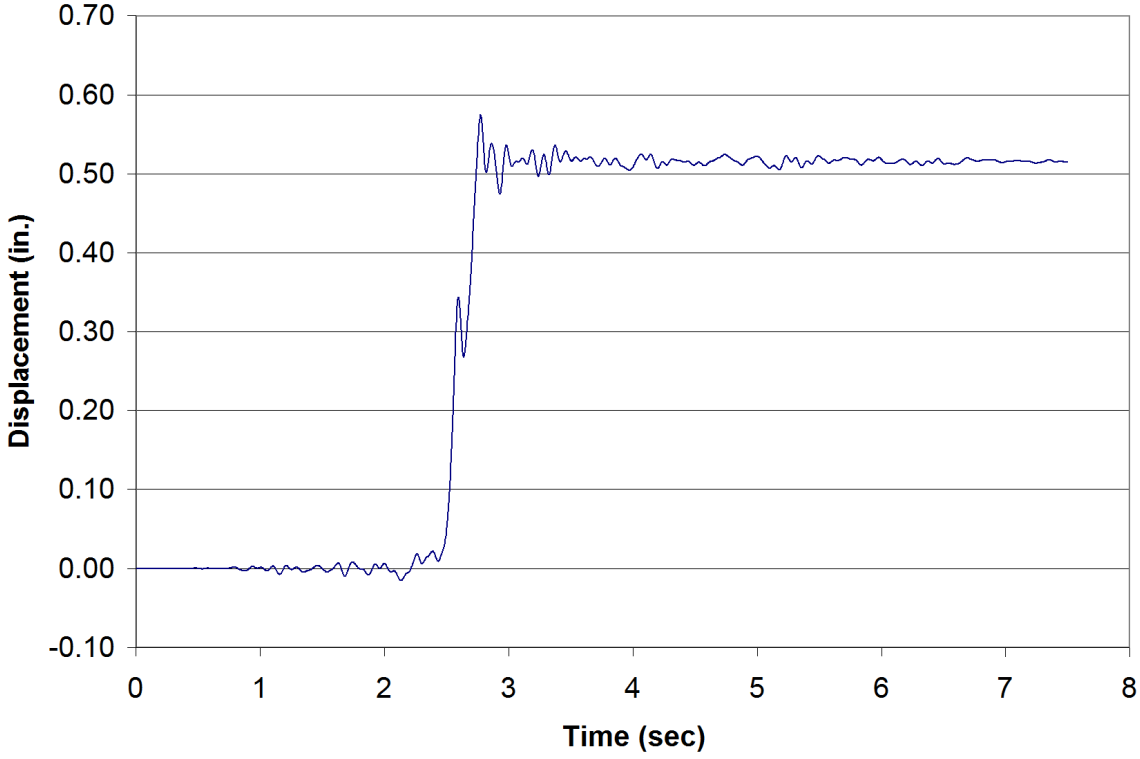

Fig. 4.6 OOP deformation, Δ_N, time history for first-story infill.

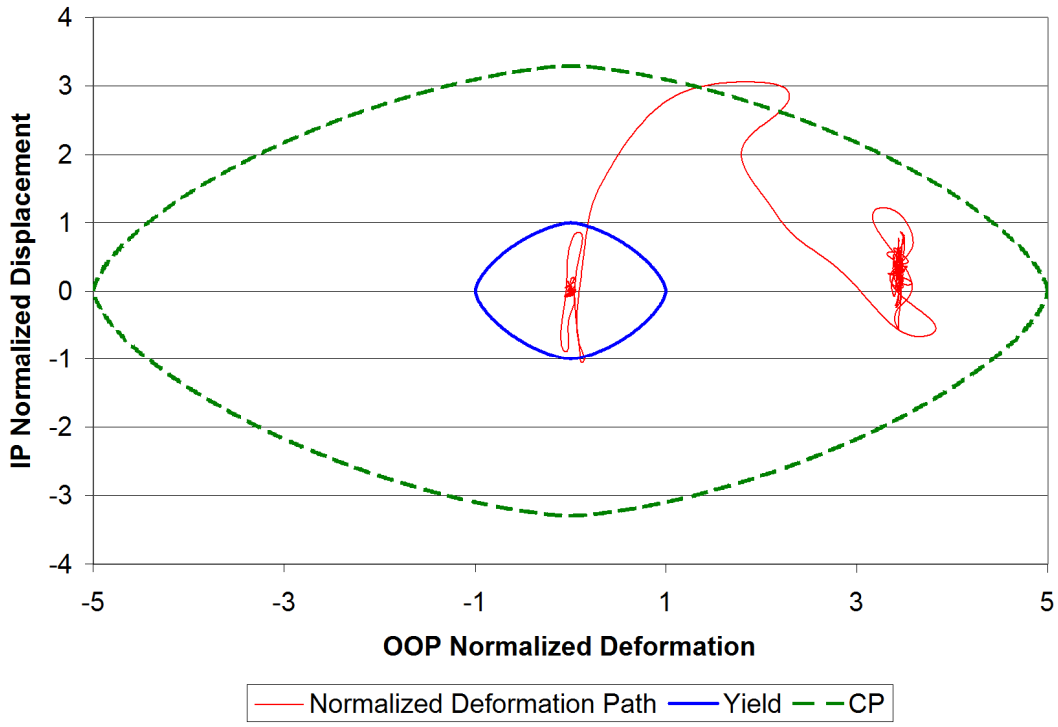

Fig. 4.7 IP-OOP normalized deformation path for first-story infill.

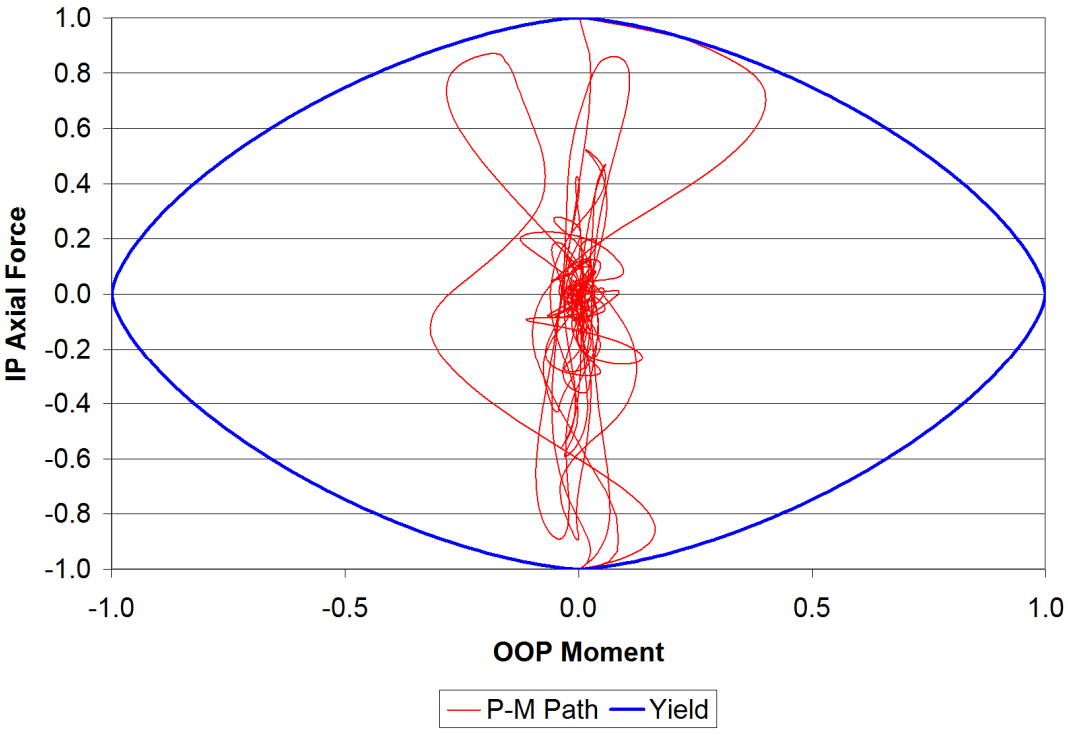

Fig. 4.8 Normalized (IP axial force)–(OOP moment) path for first-story infill.

4.3 FRAGILITY CURVE CALCULATIONS FOR INFILL PANELS

It is possible to construct fragility curves, given the results of the 100 time history analyses discussed in the previous section. In this study, a fragility curve or function is defined as the probability that the response of a particular infill panel will exceed a chosen limit state, for a given spectral acceleration, *Sa*. Here, collapse prevention (CP), as defined in Chapter 3, is the chosen limit state (*LS*). For this part of the study, it is assumed that only record-to-record variability affects the resulting probabilities. The effect of strength variability is investigated later in this chapter.

In order to facilitate calculations, define a variable known as the deformation interaction ratio (*DIR*) as follows:

$$DIR(t) = \left[\left(\frac{\Delta_H(t)}{\Delta_{Hcp\,0}} \right)^{\frac{3}{2}} + \left(\frac{\Delta_N(t)}{\Delta_{Ncp\,0}} \right)^{\frac{3}{2}} \right]^{\frac{2}{3}} \tag{4.3}$$

where

$\Delta_H(t) =$ IP deformation of the infill panel at time *t*

$\Delta_{Hcp0} =$ IP deformation to cause the panel to reach CP in the absence of OOP deflection (see Chapter 3)

$\Delta_N(t) =$ OOP deformation of the infill panel at time *t*

$\Delta_{Ncp0} =$ OOP deformation to cause the panel to reach CP in the absence of IP deflection (see Chapter 3)

This definition is derived from the 3/2-power interaction curves discussed in Section 3.4. The CP limit state is reached when the value of the *DIR* equals 1.0. The 2/3 exponent is added for geometrical clarity: for an arbitrary point in the (Δ_H/Δ_{Hcp0}), (Δ_N/Δ_{Ncp0}) plane with a *DIR* of, e.g., 3, a line joining it to the origin will intersect the interaction curve at 1/3 of the distance from the origin to the point. Thus, the *DIR* may be estimated directly from a normalized deformation path such as Figure 4.7 above.

As discussed above, under the definition given in Equation (4.3) the infill panel will reach the CP limit state when the *DIR* equals or exceeds 1.0. Note also that this definition calculates the IP-OOP interaction function at each time step in the analysis, and then takes the maximum for the entire time record, in contrast to the previous work of Hashemi and Mosalam

(2007), in which the maximum IP and maximum OOP responses were used in the interaction check, without considering their temporal relationship.

The calculations for the fragility functions in this study proceed as follows:

1. At each *Sa* level, the maximum *DIR* is determined for each earthquake record.
2. Since the distribution of the *DIR*'s is assumed to be lognormal, the natural logarithm, ln(*DIR*), is found for each record.
3. Then, the mean and sample standard deviation are found for the ln(*DIR*)'s for each set of 20 records. Note that the infill panel reaches the CP limit state when ln(*DIR*) = 0.0.
4. Finally, the probability of reaching or exceeding the CP limit state is given by

$$P(LS \geq CP) = 1 - \Pr_{norm}(0, \mu_{\ln DIR}, \sigma_{\ln DIR}) \tag{4.4}$$

where

$\mu_{\ln DIR}$ = mean of the ln(*DIR*)'s from the 20 records

$\sigma_{\ln DIR}$ = sample standard deviations of ln(*DIR*)'s from the 20 records

$\Pr_{norm}(0, \mu_{\ln DIR}, \sigma_{\ln DIR})$ = cumulative probability that the random variable ln(*DIR*) will exceed 0.0, given $\mu_{\ln DIR}$ and $\sigma_{\ln DIR}$, and assuming that ln(*DIR*) has a normal distribution (i.e., *DIR* has a lognormal distribution)

The procedure described above is performed for each of the five selected levels of *Sa*. As an example, the fragility function for the infill panel of the first story, center bay, is given in Figure 4.9. As shown in this example, there is approximately a 50% probability of exceeding the CP limit state for an earthquake with *Sa* = 1.0g, while at *Sa* = 2.5g the probability of exceedence is greater than 95%.

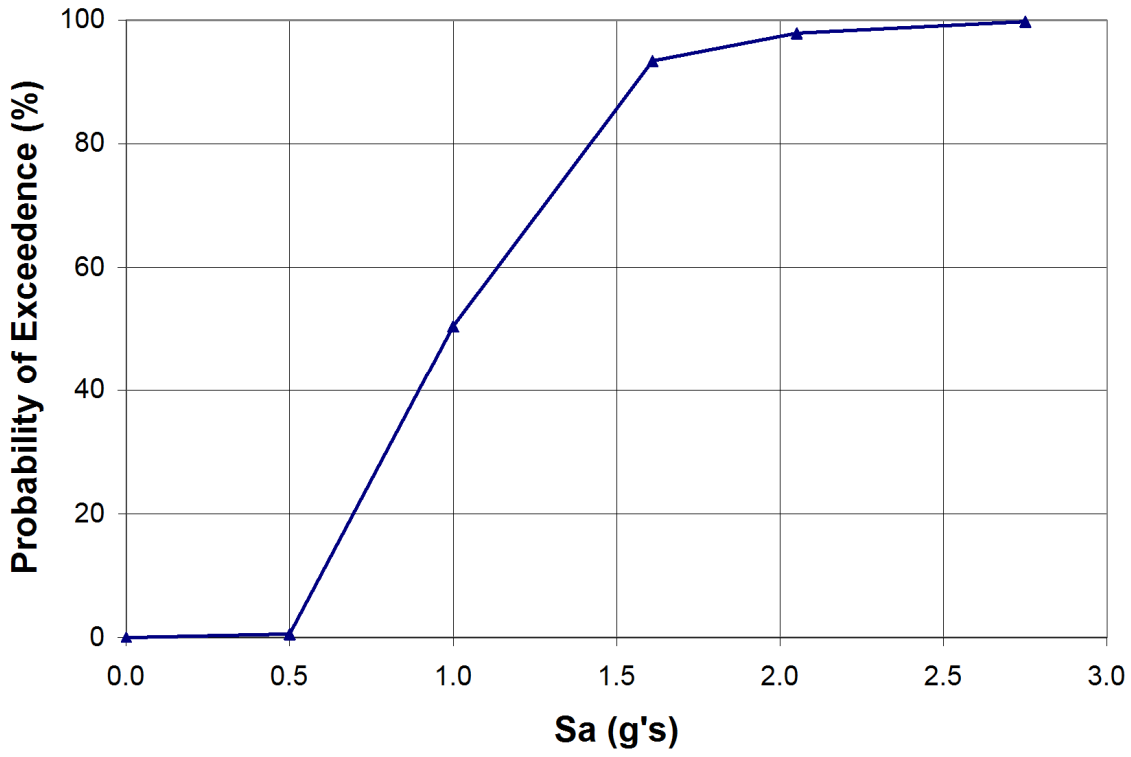

Fig. 4.9 Fragility function for reaching or exceeding CP limit state for first-story, center bay, infill panel.

It is possible to examine the relative contributions to the fragility function from the IP and OOP responses. Define:

$$DIR\_IP(t) = \frac{\Delta_H(t)}{\Delta_{Hcp\,0}} \tag{4.5}$$

$$DIR\_OOP(t) = \frac{\Delta_N(t)}{\Delta_{Ncp\,0}} \tag{4.6}$$

Thus, *DIR_IP* represents the deformation ratio for the IP response only, while *DIR_OOP* represents the corresponding ratio for the OOP response. It is possible to calculate fragility functions for these deformation ratios, using the same method as described above. The fragility functions for *DIR*, *DIR_IP*, and *DIR_OOP* are given in Figures 4.10, 4.11 and 4.12 for the center bay of the first, third, and fifth story, respectively. It is noted that the response of *DIR_IP* is dominant at the first story, while the *DIR_OOP* is dominant at the fifth story. The two responses are roughly equal at the third story. This pattern can be explained by the fact that IP loads are cumulative, and are maximized at the first story, while OOP loads are not cumulative, but depend on OOP accelerations, which increase with height.

It is of some interest to consider the impact of ignoring the IP-OOP interaction effects on the CP fragility functions. The common practice is to check an infill wall for the IP force without considering the OOP loading, and then to check it for the OOP force, ignoring the IP loads. Taking Figure 4.10 as an example, it is clear that the probability of reaching the CP limit state is higher when the interaction effects are considered than for the case where interaction is ignored. Whether these differences would have significant impacts on project decisions can be determined only on a case-by-case basis, but the nontrivial magnitudes of the differences indicate that some consideration should be given for this interaction effect, at least in an informal way.

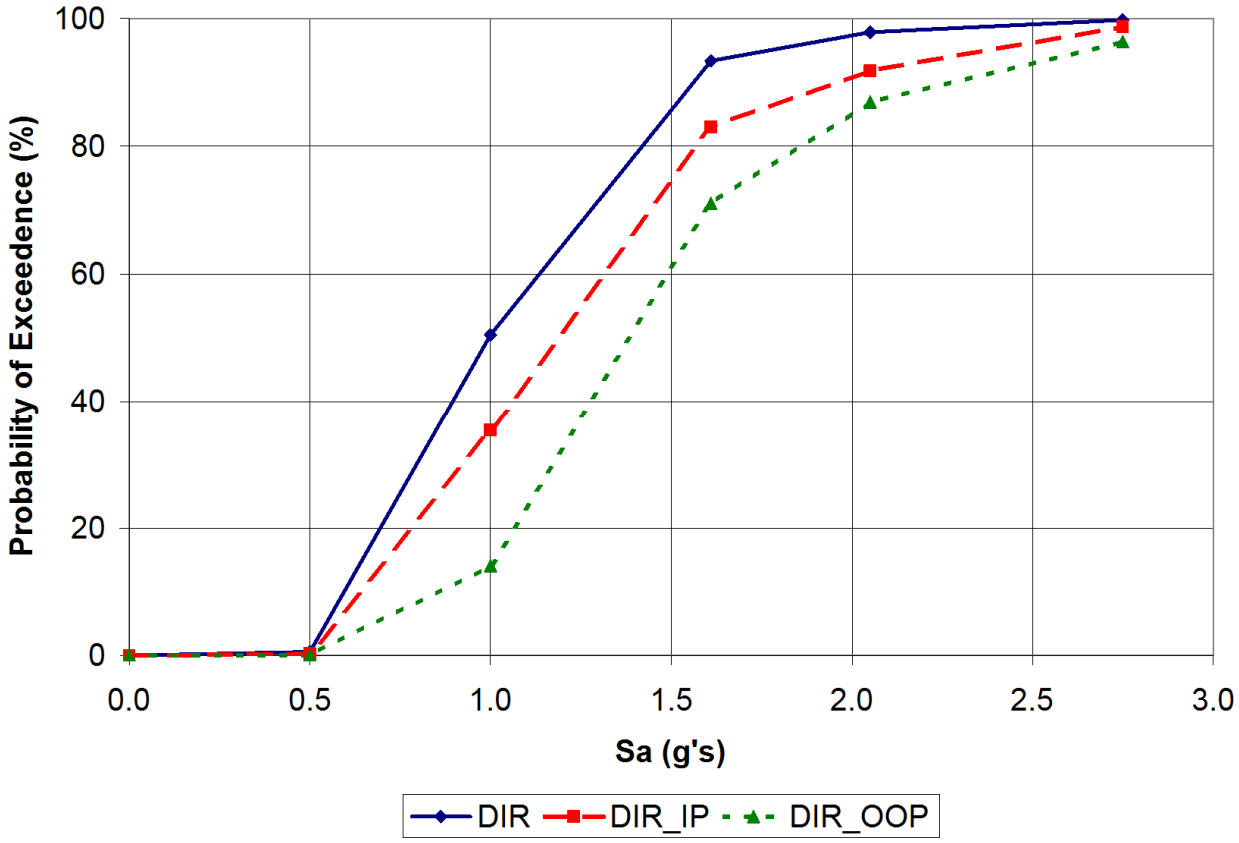

Fig. 4.10 CP fragility functions for first-story, center bay, infill panel.

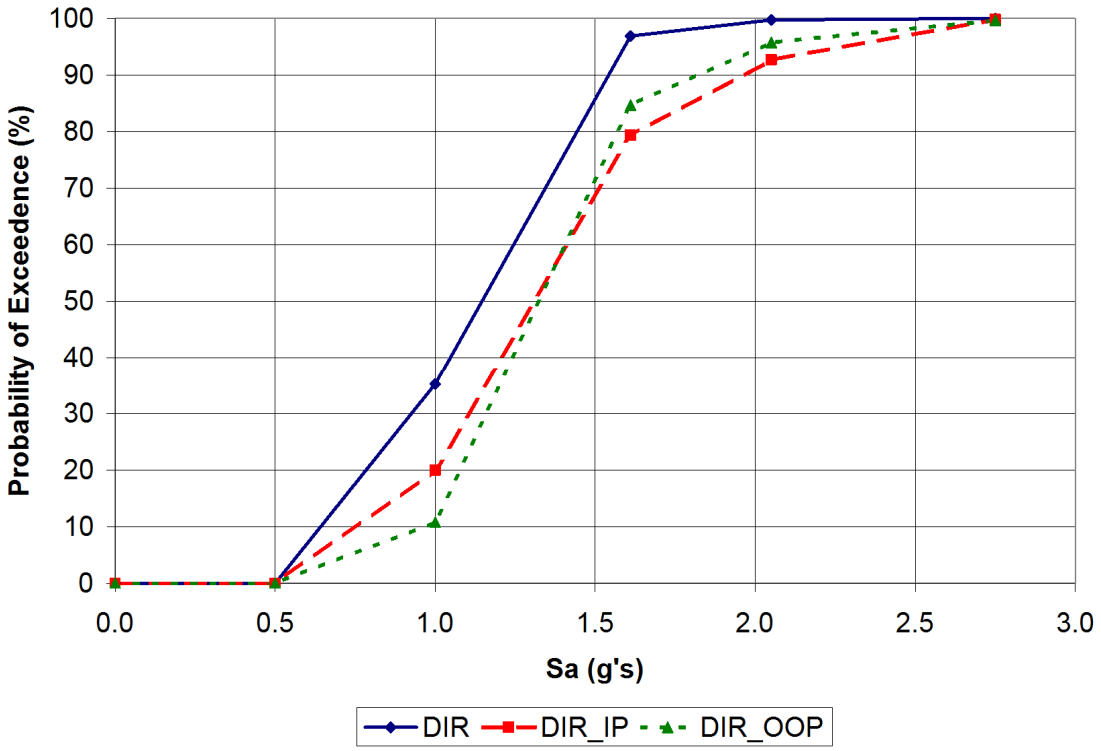

Fig. 4.11 CP fragility functions for third-story, center bay, infill panel.

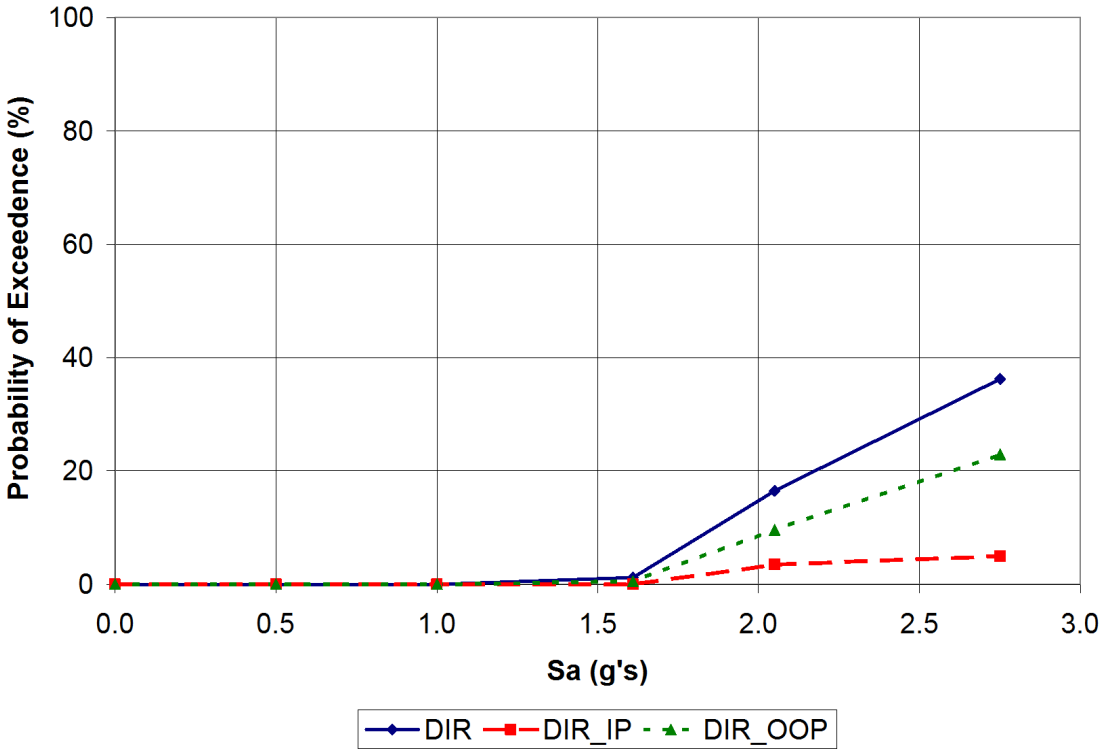

Fig. 4.12 CP fragility functions for fifth-story, center bay, infill panel.

It is also of some interest to compare the fragility functions developed in this chapter with the functions previously derived by Hashemi and Mosalam (2007). This is presented in Figure 4.13, where the fragility function derived in this report for the center bay of the first story (labeled "CP fragility") is compared with that derived by Hashemi and Mosalam (2007) (labeled "H&M — original"). Although the two functions appear to be similar, this similarity is not meaningful. One reason for this is that the fragility function from the previous investigation by Hashemi and Mosalam (2007) is not defined as the probability of reaching deformations necessary to cause collapse, as it is in this report. Rather, the infill struts were modeled as elastic, compression-only members, and were assumed to have "failed" when the loads in them reached their capacities (based on the interaction relationship), using the envelope of recorded demand IP and OOP forces. Thus, the previous fragilities may be described as force-based "yield" fragilities rather than CP fragilities as defined in this study.

A second difference between the fragilities derived in the present study and those from Hashemi and Mosalam (2007) is the fact that this study uses an IP capacity equal to approximately 70% of the capacity used in the earlier investigation, and an OOP capacity that is approximately half that used before. This is due to a different interpretation of the FEMA 356 provisions. In order to assess this effect, a Monte Carlo simulation (MCS) is applied to the model used by Hashemi and Mosalam (2007), with the exception that the IP and OOP capacities are taken as similar to this study (see Appendix F for more details and an example MCS). The results of this updated fragility evaluation are shown in Figure 4.13, labeled as "H & M — modified." The difference between the updated Hashemi and Mosalam fragility and the current report fragility is because they are based on different limit states. The probability of exceeding the "yield" limit state is obviously greater than the probability of exceeding the CP limit state.

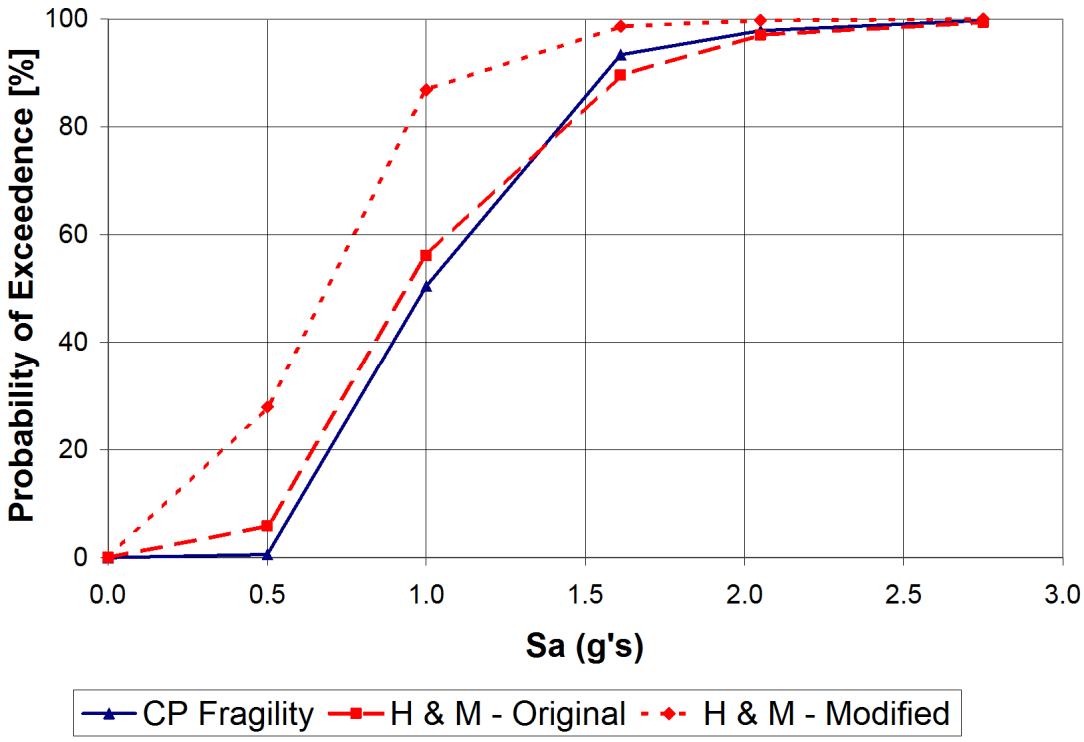

Fig. 4.13 Comparison of fragility functions.

4.4 EFFECTS OF INFILL STRENGTH VARIBILITY

The probabilities of exceedence calculated above are based on the assumption that the only random variable involved is that of the ground motion profile (GMP), i.e., the record-to-record variability. This is equivalent to assuming that the remaining parameters, such as strength, stiffness, and damping, are deterministic. Of course, this is not true in general structural engineering applications (Lee and Mosalam 2004, 2005, and 2006). As a simple extension, the effect of including the URM infill strength variability is investigated. It is to be noted that the material and geometrical properties of the bounding RC frame should also be treated as random variables. However, for simplicity, these are treated in this study as deterministic.

A common method for determining the variability in response due to the variability in the input parameters is the first-order, second-moment (FOSM) reliability analysis [see Lee and Mosalam (2005) for details]. In this method the relationship between the variance of the response and those of the input parameters is expanded in a Taylor series, and only the first order terms are retained, giving a linear relationship. Since the GMP and strength are uncorrelated, the variance in the response, ln(*DIR*), is given by

$$(\sigma_{\ln DIR})^2 = (\sigma_{GMP})^2 + (\sigma_{strength})^2 \tag{4.7}$$

where

$(\sigma_{GMP})^2 =$ variance in ln(*DIR*) due to GMP variability, calculated in Section 4.3 above, where it was designated $(\sigma_{\ln DIR})^2$, i.e., the 20 analyses at each *Sa* level are considered to be the different realizations in hypothetical Monte Carlo Simulations

$(\sigma_{strength})^2 =$ variance due to the variability in strength to be obtained from the knowledge of the URM material variability

From the FOSM theory:

$$(\sigma_{strength})^2 = \left(\frac{\partial G}{\partial f_m}\right)^2 \times \sigma_{fm}^2 \tag{4.8}$$

where

$\sigma_{fm} =$ standard deviation of the URM prism strength, f_m.

$G =$ function for determining ln(*DIR*), i.e., $\ln(DIR) = G(GMP, f_m)$

It is assumed that both the IP and the OOP capacities of the infill are fully correlated with f_m. The partial derivative of G is calculated numerically using finite differences as suggested by Lee and Mosalam (2005), as follows:

$$\frac{\partial G}{\partial f_m} = \frac{G(GMP_0, f_{me} + \Delta f_m) - G(GMP_0, f_{me} - \Delta f_m)}{2\Delta f_m} \tag{4.9}$$

where

$GMP_0 =$ the "median" ground motion profile, taken for this study as the time history set which produces the 11th-largest *DIR* at the location of interest

$f_{me} =$ the expected URM prism strength, taken as 2.46 ksi in this study based on material tests reported in (Hashemi and Mosalam 2007)

$\Delta f_m =$ numerical variation of the prism strength

The value of Δf_m is taken to be equal to $0.05\sigma_{fm}$ as recommended by Lee and Mosalam (2005). Following Hashemi and Mosalam (2007), $\sigma_{fm} = 0.231 f_{me}$. This results in $\Delta f_m = 0.01155 f_{me}$, i.e., about 1.2% numerical variation in strength for a 23.1% coefficient of variation of the strength. Substituting into Equations (4.8) and (4.9) gives

$$\left(\sigma_{strength}\right)^2 = \left(\frac{G(GMP_0, f_{me} + \Delta f_m) - G(GMP_0, f_{me} - \Delta f_m)}{2(0.05)} \right)^2 \tag{4.10}$$

The seismic analysis is performed twice at each value of *Sa,* once with the f_m set at $f_{me}+\Delta f_m$, and the other with it set at $f_{me}-\Delta f_m$.

An example of calculations for input parameters, leading to new fiber element models for the infill panels, is given in Appendix G, which considers a positive variation in f_m. Calculations for a negative variation in f_m are similar. The ln(*DIR*) response is calculated for each case, and substituted into Equation (4.10). Then Equation (4.7) is used to calculate $\sigma_{\ln DIR}$, and Equation (4.4) is used to calculate the probability that the *DIR* exceeds the CP limit state. The resulting fragility function is shown in Figure 4.15 (labeled "GMP + Strength"), plotted with the fragility function derived in Section 4.3, where the only random variable is assumed to be the GMP (labeled "GMP only"). It is observed that the consideration of the variability of the strength of the URM infill wall increases the probability of exceedence at probability levels below 50%, and decreases this probability at higher levels. This is a consequence of the fact that increasing uncertainty does not change the median *DIR* but does increase its variance; thus, the fragility function flattens, and "spreads out" horizontally from its median point. The effect of considering strength variability, however, is very small. This observation agrees with the work of other investigators, e.g., Lee and Mosalam (2005), who have found that GMP is the major source of uncertainty in structural response at a given spectral acceleration.

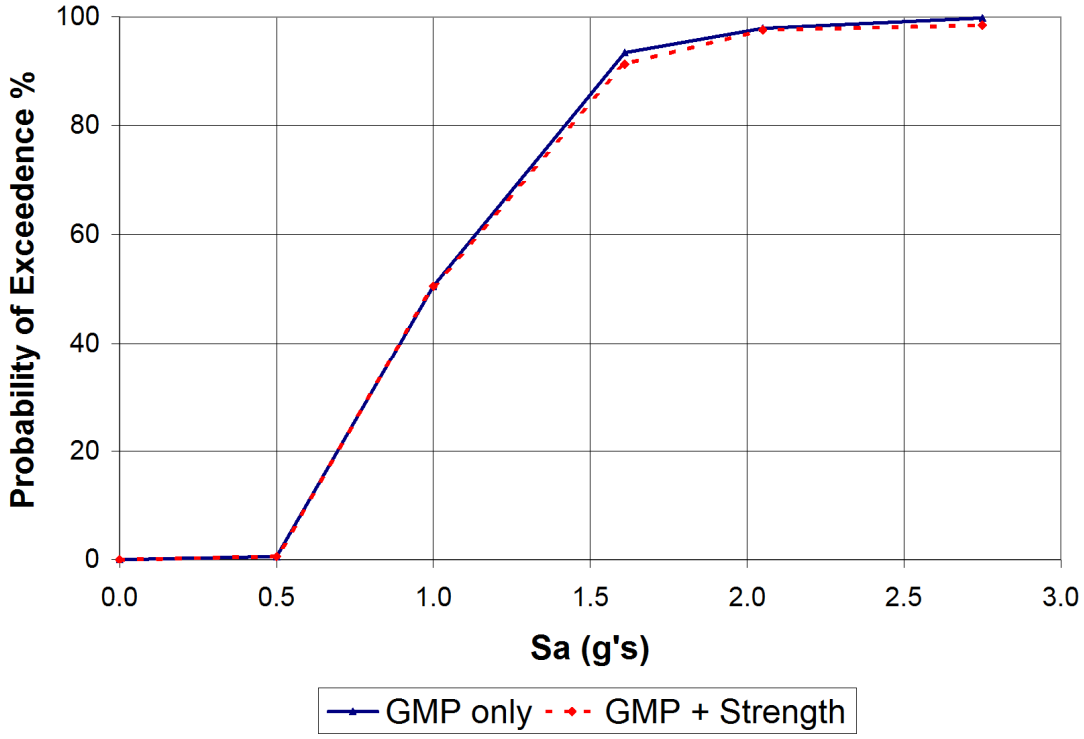

Fig. 4.14 Fragility functions (probability of DIR exceeding 1.0) including effect of infill strength variability.

Since the effect of strength variability is so small, it is difficult to see in Figure 4.14, especially for values of *Sa* less than the median. Figure 4.15 plots the ratio *R(Sa)*:

$$R(Sa) = \frac{\Pr_{GMP+strength}(Sa)}{\Pr_{GMP}(Sa)} \tag{4.11}$$

where

$\Pr_{GMP+strength}(Sa) =$ Vulnerability function calculated considering the variability of both the ground motion profile and the infill wall strength

$\Pr_{GMP}(Sa) =$ Vulnerability function calculated considering the variability of the ground motion profile only

It is seen that the ratio *R(Sa)* is greater than unity at values of *Sa* less than the median, which occurs at about 1.0g, and less than unity when *Sa* is greater than the median. It is also seen that the vulnerability functions vary by, at most, 2.2%. It is believed that irregularities in the shape of the function *R(Sa)* are due to randomness in the analysis results.

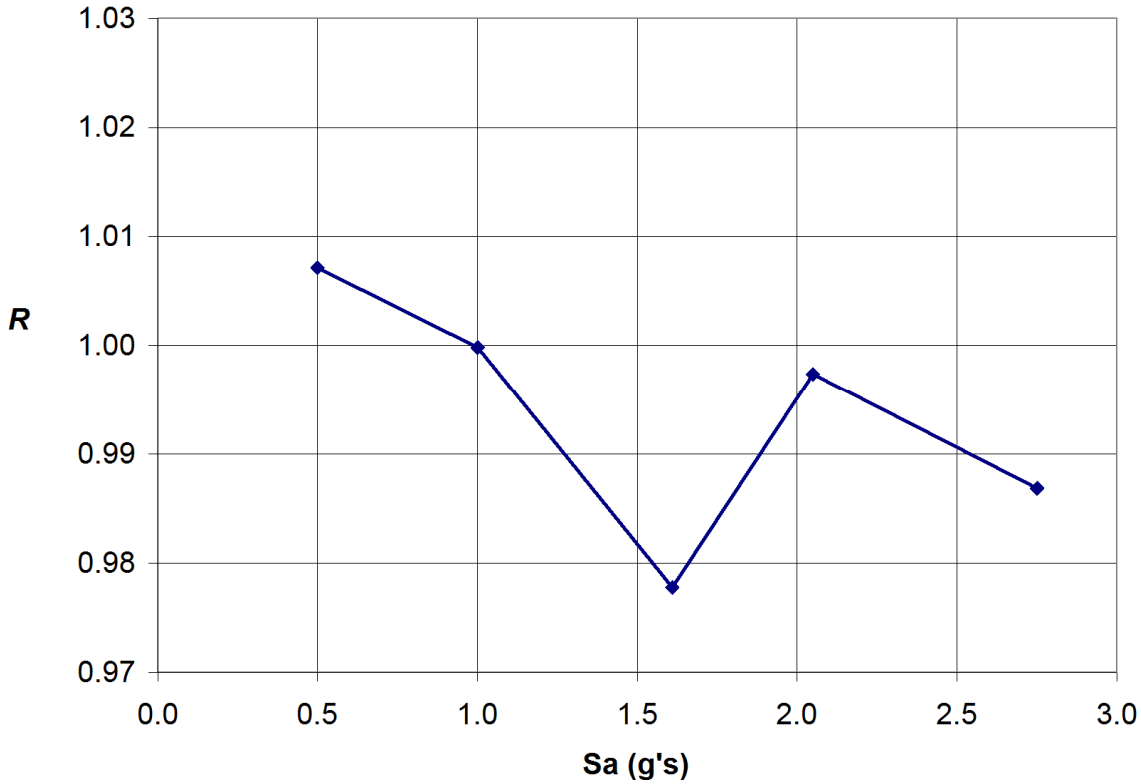

Fig. 4.15 Variation of ratio *R(Sa),* defined by Eq. (4.11).

4.5 INTERSTORY DRIFT RATIO RESULTS

As an example of the global responses of the building model, the interstory drift ratio (IDR) is calculated for each of the five stories. The IDR is defined as displacement of the top of a given story, relative to the bottom of that story, divided by the story height. The IDR is calculated for each time step in the dynamic analysis, and the maximum value is recorded. For example, the x-direction (longitudinal) IDR envelopes (lines connecting maximum values irrespective of their possibly different temporal occurrences), calculated for the 20 analyses with *Sa* = 1.0g, are shown in Figure 4.16. This figure illustrates the scatter in responses for a single spectral acceleration level. The IDRs increase from the fifth story to the ground with the exception that the first-story IDR is smaller than that of the second story. This is believed to be because the building columns are fixed against rotation at the ground level, causing the first story to be stiffer than the second.

As with the local infill panel responses discussed above, statistical analysis was applied to the IDR results. Figure 4.17 presents the average IDRs for the 20 records, as a function of the

five spectral acceleration levels. It is, of course, possible to derive fragility functions for the obtained IDRs with respect to chosen threshold values for the limit states defined for these global metrics. Figure 4.18 gives the probability that the IDR at a given story exceeds a value of 0.002. This value is chosen based on the work of Mosalam et al. (1997), in which this value was used to define the "heavy damage" limit state, corresponding approximately to the CP limit state used in this report, for RC frames with URM infill. The results imply that, for this model, the second story is critical (see Section 4.2).

As an illustration of the relationship between the local and global fragilities, Figure 4.19 compares the first-story CP fragility (taken from Fig. 4.9) with the first-story IDR = 0.002 fragility from Figure 4.18. It is seen that the two fragility functions are quite similar, leading to the conclusion that they are strongly correlated.

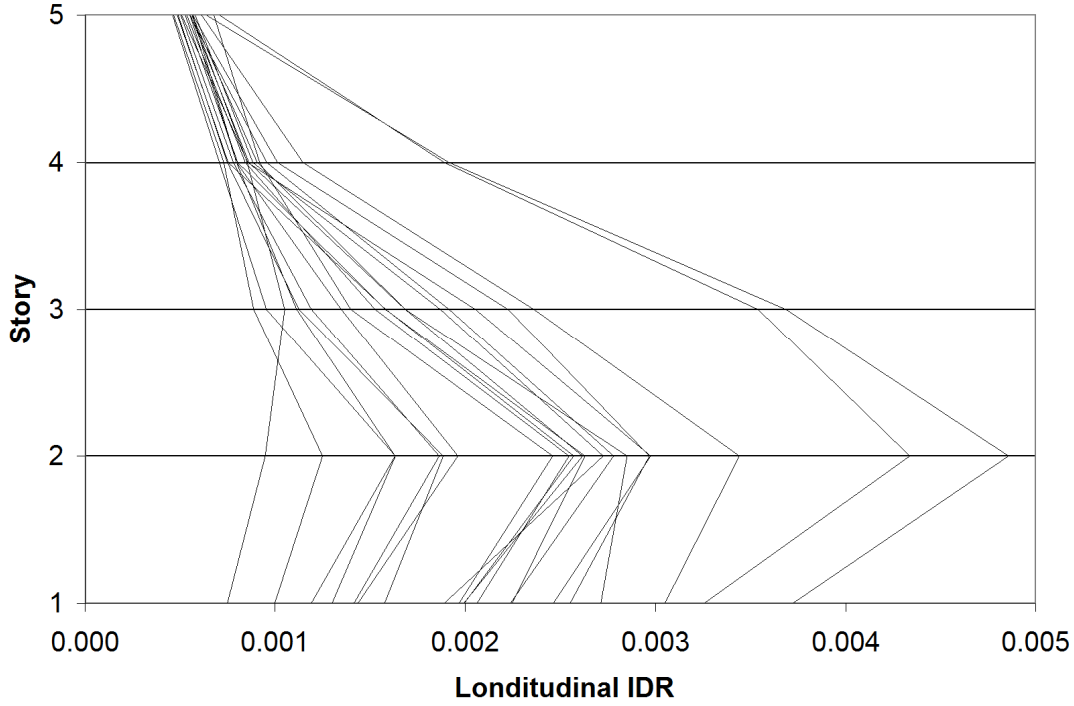

Fig. 4.16 Longitudinal IDRs for *Sa* = 1.0.

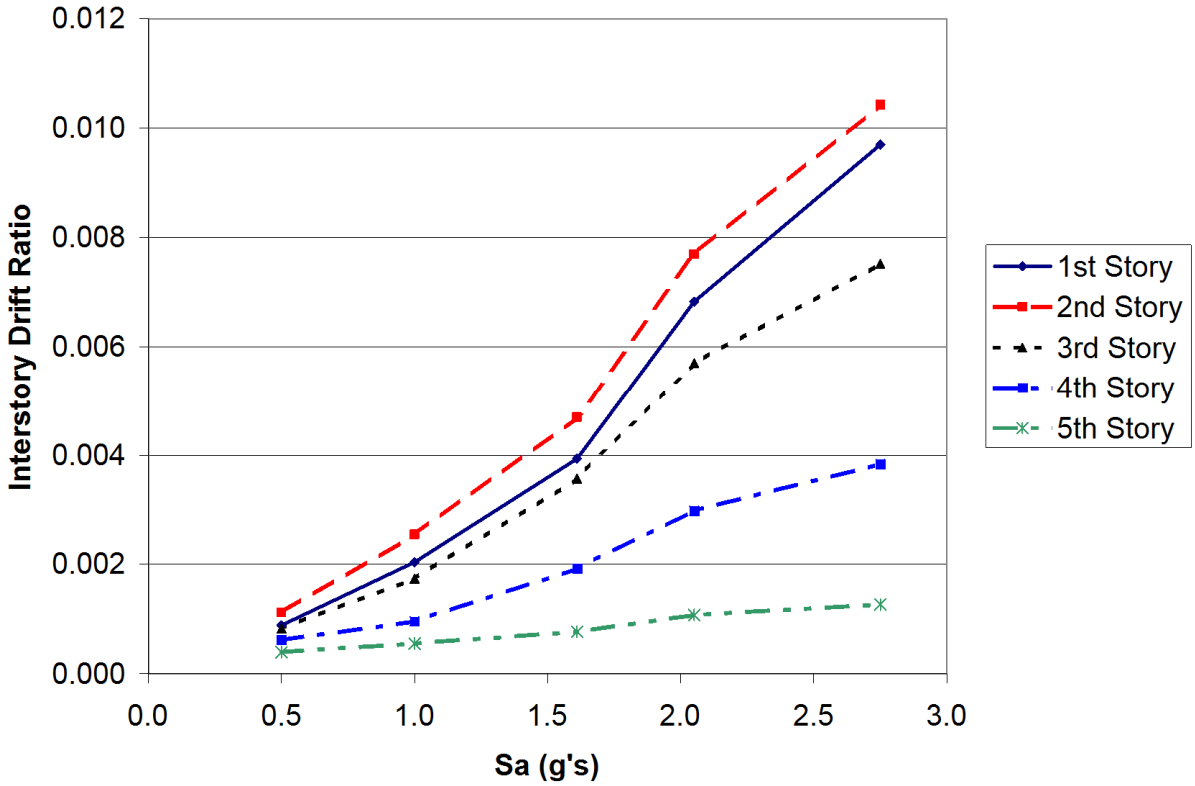

Fig. 4.17 Average interstory drift ratios.

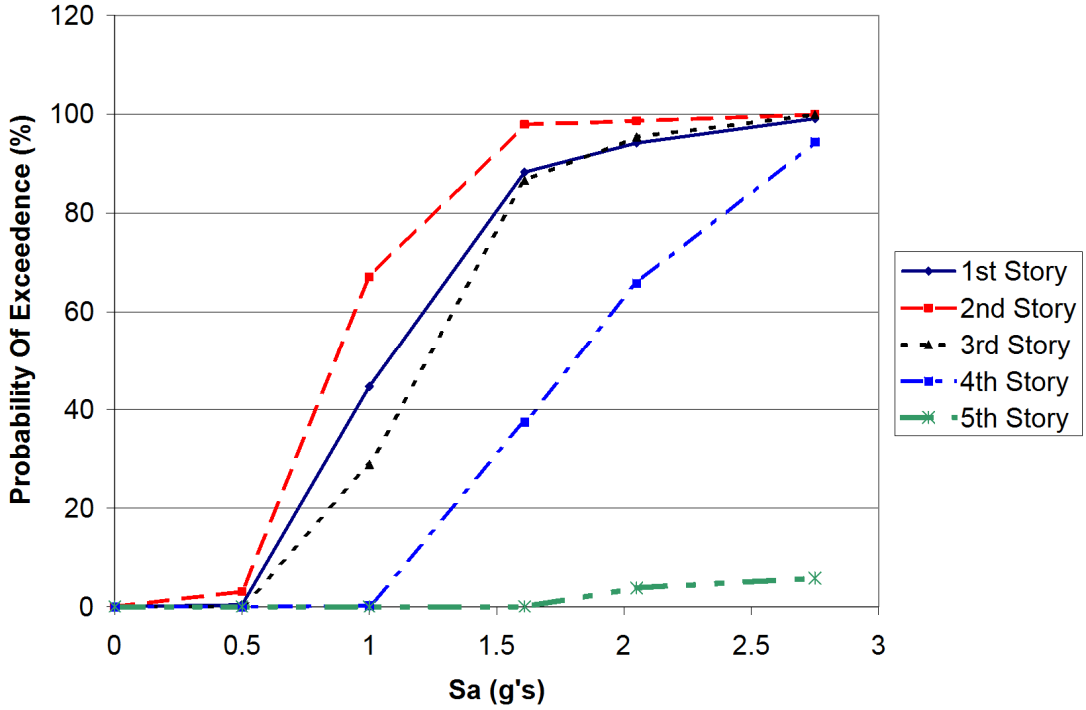

Fig. 4.18 Fragility functions for IDR exceeding 0.002.

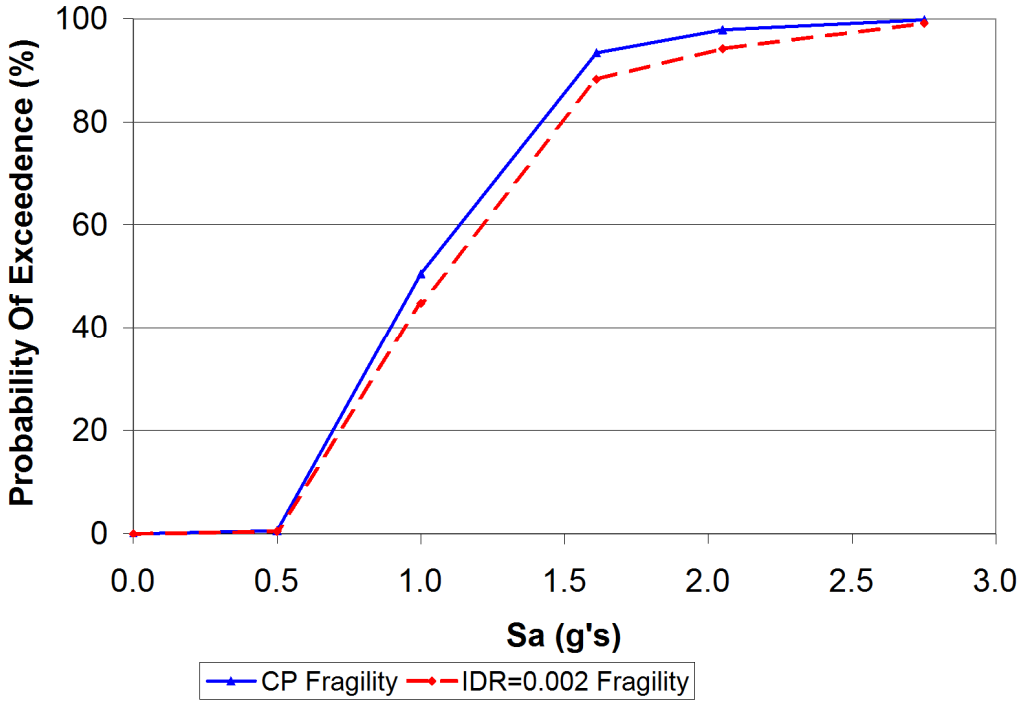

Fig. 4.19 Comparison of CP fragility and IDR=0.002 fragility for first story.

5 Summary, Conclusions, and Future Extensions

5.1 SUMMARY

This report is part of a larger study of reinforced concrete (RC) frame structures with unreinforced masonry (URM) infill walls. The purpose of the report is to develop a practical analytical model of the infill walls that can be used in a nonlinear time history analysis of the overall structure and that properly considers the interaction between the in-plane (IP) and out-of-plane (OOP) strengths of the wall. The interaction function is taken from finite element analyses (FEA) reported by Hashemi and Mosalam (2007).

The behavior of a strut and tie (SAT) infill model previously proposed by Hashemi and Mosalam (2007) is examined. That model was shown to correctly satisfy the interaction relationship when displaced monotonically in the IP direction while a constant force is applied in the OOP direction, i.e., a conventional pushover analysis. However, in this report, it is found that under certain circumstances this SAT model can produce forces that will violate the prescribed interaction boundary surface. In addition, the SAT model has a limited number of input parameters, and it becomes somewhat difficult to simultaneously satisfy requirements for IP and OOP elastic stiffness (and hence frequencies), along with the IP and OOP strengths and their interaction functions.

This report proposes a new infill model, based on a beam-column element with a cross section consisting of a collection of nonlinear fibers. Each infill wall panel is modeled as a single diagonal with two members, with an OOP mass at the center to represent the OOP inertia of the wall. A method for calculating the properties of the individual cross-section fibers is derived, such that the pure "axial strut" IP capacity, the pure "bending" OOP capacity, and their interaction function are reproduced. A theoretical basis is established for ensuring dynamic equivalence between the actual infill wall panel and the panel model. It is demonstrated that with an OOP mass equal to the modal effective mass of the actual infill panel, and a model with an

OOP frequency equal to that of the actual panel, the reactions at the support points of the infill model (the floor diaphragms) will also be duplicated. Thus, the global behavior of the overall structural model is preserved.

A case study single panel model is developed, with strengths for pure IP and pure OOP behavior based on the provisions of FEMA 356 (FEMA 2000). The model behavior is demonstrated by several loading configurations. One configuration is a duplication of the pushover analysis used by Hashemi and Mosalam (2007). Another configuration is a "double displacement" pushover, in which both the IP and OOP displacements are prescribed. Finally, the model is exposed to a time history base acceleration. It is shown that the model correctly satisfies the strength and interaction criteria under all circumstances. The behavior of the model in the inelastic region is studied, and a criteria is developed for determining when the wall panel reaches the "collapse prevention" (CP) limit state defined by FEMA 356 (FEMA 2000). This CP limit state is defined by limits on the infill model ductility, and is not an inherent property of the model; i.e., the model capacities do not drop to zero when it is reached. The limitations of the model in the post-yield and post-CP states are discussed.

As an example of the general use of the proposed model, it is incorporated into a five-story RC frame building model previously studied by Hashemi and Mosalam (2007), with the proposed infill model in this report substituted for their infill model. The building model is then subjected to a suite of 20 time histories of ground accelerations. The individual time histories within the suite are scaled so that their spectral accelerations at the fundamental natural frequency of the building are equal to a common value. These analyses are performed for a range of five different spectral acceleration values, for a total of 100 analyses. Based on the results of these analyses, vulnerability curves are generated, giving the probability that selected infill panels will reach the CP limit state, as a function of spectral acceleration level. These vulnerability curves are compared to those generated previously by Hashemi and Mosalam (2007), and it is found that they predict lower probabilities at all values of the spectral accelerations. This is primarily because the previous vulnerability study by Hashemi and Mosalam (2007) was based on strength rather than ductility, and thus represents a lower level of damage than CP. It is also noted that the effect of including the strength interaction function, relative to an analysis in which it is not considered (which is common practice in engineering design offices), may not be negligible.

Since the 100 analyses described above used deterministic (non-varying) stiffness, damping, and strength properties in the structural model, the uncertainty in the generated vulnerability curves derives solely from the record-to-record variability (also known as ground motion profile variability). In order to illustrate the procedure for determining the effects of other uncertainties, a first-order, second-moment (FOSM) analysis is conducted for uncertainty in the strength of the infill panels. It is found that the effect of strength uncertainty is very small compared to that for the ground motion profile.

5.2 CONCLUSIONS

Based on the results presented in this report, the following conclusions are drawn:

1. The behavior of the infill model previously proposed by Hashemi and Mosalam (2007) is somewhat problematic. Under certain circumstances, the IP and OOP forces in the infill model may exceed the specified interaction surface. Additionally, it may be difficult to match the elastic properties of the model with those of the actual infill panel.
2. Using a beam-column element with a cross section composed of nonlinear fibers, it is possible to capture the IP and OOP strengths of the infill panel, as well as its elastic stiffness properties. Based on the procedures developed in this report, it is possible to specify the infill model mass, strength, and stiffness properties so that the global behavior of the overall structural model is essentially preserved.
3. Some undesired numerical damping may be introduced into the model while it is still in the nominally “elastic” range. This is due to the fact that it does not appear to be possible to specify fiber properties such that the transition from elastic to plastic behavior is “sharp," i.e., occurs over an arbitrarily small increment of deflection. This leads to early yielding of some of the fibers, and consequent hysteretic behavior under cyclic loading to displacements near the yield level.
4. The main limitations of the model occur in the post-elastic range. First, control of the shape of the load-deflection curves in the post-yield state, i.e., whether the behavior is hardening, softening, flat, or some combination of the three, is not possible using the elastic–perfectly plastic fiber elements used in this report. While it may be possible to control the behavior by adjusting the post-yield properties of the fibers, a straightforward methodology for doing so is not immediately obvious.

5. Second, the fact that the infill panel model retains strength and stiffness after exceeding the CP limit state is unrealistic, and leads to errors in the calculated global responses of the building model. This is because the "collapsed" panels will still be carrying load in the analysis, which will lead to an underestimation of the load in the other panels and elements of the surrounding frame. It may be possible to work around this limitation, as discussed in Section 3.7, but this increases the complexity of the analysis.
6. With due attention to these limitations, it is practical to use the model in vulnerability analyses, since it behaves in a stable fashion, and appears to give reasonable results.
7. Based on the results of the vulnerability analyses in this report, it appears that the interaction between the IP and OOP strengths of the infill wall has a measurable impact on vulnerabilities, and may need to be considered, at least in an informal manner. This would represent a change in the typical evaluation procedure, e.g., using FEMA 356 (FEMA 2000), as it is practiced today.
8. The major source of uncertainty in the vulnerability study is the record-to-record variability of the input acceleration time histories, with strength uncertainties making a much smaller contribution.

5.3 FUTURE EXTENSIONS

While the proposed URM infill model is successful in modeling the elastic stiffness and the strength of the wall, including interaction effects, questions remain regarding its behavior in the post-elastic range of deformation. Resolution of these questions would present opportunities for further work on this subject.

One current limitation is the lack of knowledge concerning the actual behavior of URM infill panels under combined IP and OOP loads in the post-elastic range, for both monotonic and cyclic loads. Experimental investigations, supplemented by FEA, are needed to gain an understanding of this behavior, and thereby establish the goals for the practical model to meet. It should be noted that one goal of this study was a model in which post-yield displacements occur at constant loads; this goal was chosen for convenience, due to a lack of more complete understanding of the actual behavior.

Once an understanding of the actual post-elastic behavior is established, it is then necessary to modify the proposed model to provide realistic responses. As discussed, it may be

possible to achieve this by modifying the post-yield properties of the cross-section fibers; such a solution should be attempted. If this does not prove satisfactory, then other solutions, e.g., the direct element removal approach (Talaat and Mosalam 2008), may be employed. Unfortunately, these alternative solutions increase the complexity of the analysis.

It may be noted that while the previously-proposed SAT model (Hashemi and Mosalam 2007) was shown in this study to exhibit some undesirable attributes, it may still be fruitful to pursue a model based on the SAT concept. This concept seems to best describe the physical processes taking place in URM infill panels under load. Such a model might be based on detailed nonlinear FEA, using these analyses to establish the location and properties of the constituent struts and ties. This is analogous to the sophisticated approach of "topology optimization." It would be useful to carry out additional vulnerability studies, considering the effects of different strength and geometric parameters other than those used in the case study of the five-story RC building with URM infill walls. In particular, for this case study used in this report, it was found that IP deformation was the dominant mode of failure at all locations. However, it has been observed that OOP failure of infill panels occurs in many earthquakes, and it would be instructive to investigate the behavior of panels whose parameters are such that OOP failure dominates.

REFERENCES

Blevins, R.D. (1979), "Formulas for Natural Frequency and Mode Shape," Van Nostrand Reinhold Company, Inc.

Chopra, A. (2007), "Dynamics of Structures," Third Edition, Prentice Hall Inc.

Elkhoraibi, T. and Mosalam, K.M. (2007), "Generalized Hybrid Simulation Framework for Structural Systems Subjected to Seismic Loading," Pacific Earthquake Engineering Research Center, PEER 2007/101.

Federal Emergency Management Agency (FEMA) (2000), "Prestandard and Commentary for the Seismic Rehabilitation of Buildings," FEMA 356, Washington, D.C.

Garvey, P. (1993), "A Family of Joint Probability Models for Cost and Schedule Uncertainties," *27th Annual Department of Defense Cost Analysis Symposium*, September.

Hashemi, S.A. and Mosalam, K.M. (2007), "Seismic Evaluation of Reinforced Concrete Buildings Including Effects of Infill Masonry Walls," Pacific Earthquake Engineering Research Center, PEER 2007/100.

Jaiswell, K.S., Sinha, R., Goyal, A. (2002), "Housing Report: Reinforced Concrete Frame Buildings with Masonry Infill Walls Designed for Gravity Loads," *World Housing Encyclopedia*, Earthquake Engineering Research Institute, http://www.world-housing.net.

Kircher, C. A., Seligson, H.A., Bouabid, J., and Morrow, G.C. (2007), "When the Big One Strikes Again — Estimated Losses Due to a Repeat of the 1906 San Francisco Earthquake," *Earthquake Spectra*, Special Issue II, Vol. 22, November.

Lee, T.-H. and Mosalam, K.M. (2004), "Probabilistic Fiber Element Modeling of Reinforced Concrete Structures," *Computers and Structures* , Vol. 82, No. 27, 2285-2299.

Lee, T.-H. and Mosalam, K.M. (2005), "Seismic Demand Sensitivity of Reinforced Concrete Shear-Wall Building Using FOSM Method," *Earthquake Engineering and Structural Dynamics*, Vol. 34, No. 14, 1719-1736.

Lee, T.-H. and Mosalam, K.M. (2006), "Probabilistic Seismic Evaluation of Reinforced Concrete Structural Components and Systems," Pacific Engineering Research Center, 2006/04.

Li, B., Wang, Z., Mosalam, K. M., and Xie, H. (2008), "Wenchuan Earthquake Field Reconnaissance on Reinforced Concrete Framed Buildings With and Without Masonry Infill Walls," *The 14th World Conference on Earthquake Engineering*, Beijing, China.

MathSoft, Inc. (1997), "MathCad User's Guide," May.

Mazzoni, S., McKenna, F., Scott, M.H., and Fenves, G.L. (2006), "Open System for Earthquake Engineering Simulation (OpenSees), User Command-Language Manual," Pacific Earthquake Engineering Research Center, http://opensees.berkeley.edu/OpenSees/manuals/.

Mosalam, K.M., Ayala, G., White, R.N., and Roth, C. (1997), "Seismic Fragility of LRC Frames With and Without Masonry Infill Walls," *Journal of Earthquake Engineering*, Vol. 1, No. 4, 693-720.

Mosalam, K.M. and Sitar, N. (2008), "Observations After 5/12/2008 Wenchuan Earthquake Based on Field Reconnaissance from 7/4/2008 to 7/7/2008," http://peer.berkeley.edu/news/2008/china_eq_2008.html, July.

Paulay, T. and Priestley, M.J.N. (1992), "Seismic Design of Reinforced Concrete and Masonry Buildings," John Wiley & Sons, Inc.

Sharif, I., Meisl, C.S., and Elwood, K.J. (2007), “Assessment of ASCE 41 Height-to-Thickness Ratio Limits for URM Walls," *Earthquake Spectra*, Vol. 23, No. 4, November.

Talaat, M. M. and Mosalam, K.M. (2008), “Computational Modeling of Progressive Collapse in Reinforced Concrete Frame Structures," Pacific Earthquake Engineering Research Center, PEER 2007/10.

Appendix A: Strut and Tie Model Deformation and Force Relationships

This appendix presents the geometrical relationships for the analysis of the Hashemi and Mosalam (2007) model. Deformations of the model are calculated on the basis of finite displacement theory. Force resultants are calculated as well.

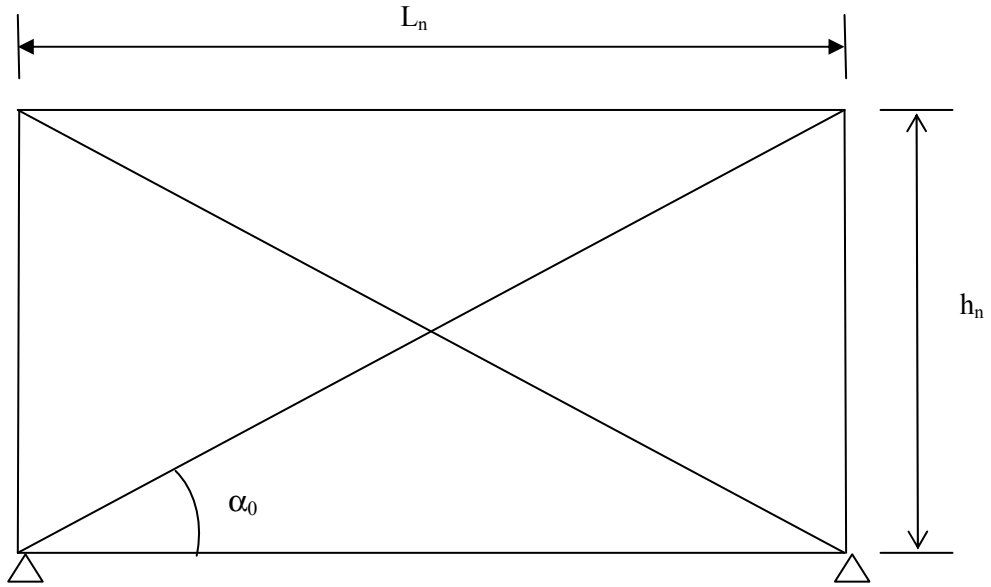

Fig. A.1 Elevation of model in undeformed state.

In Figure A.1,

$h_n =$ undeformed height of the model = 101 in.,
$L_n =$ undeformed length of the model = 162 in., and
$D_0 = \sqrt{h_n^{\,2} + L_n^{\,2}} =$ undeformed length of the diagonals.

The horizontal and vertical perimeter members are assumed rigid, and we define (Fig. A.2):

$h =$ deformed (instantaneous) height (note that the boundary members are assumed rigid) $h = \sqrt{h_n^{\,2} - \Delta_H^{\,2}}$,
$\Delta_H =$ in-plane displacement.

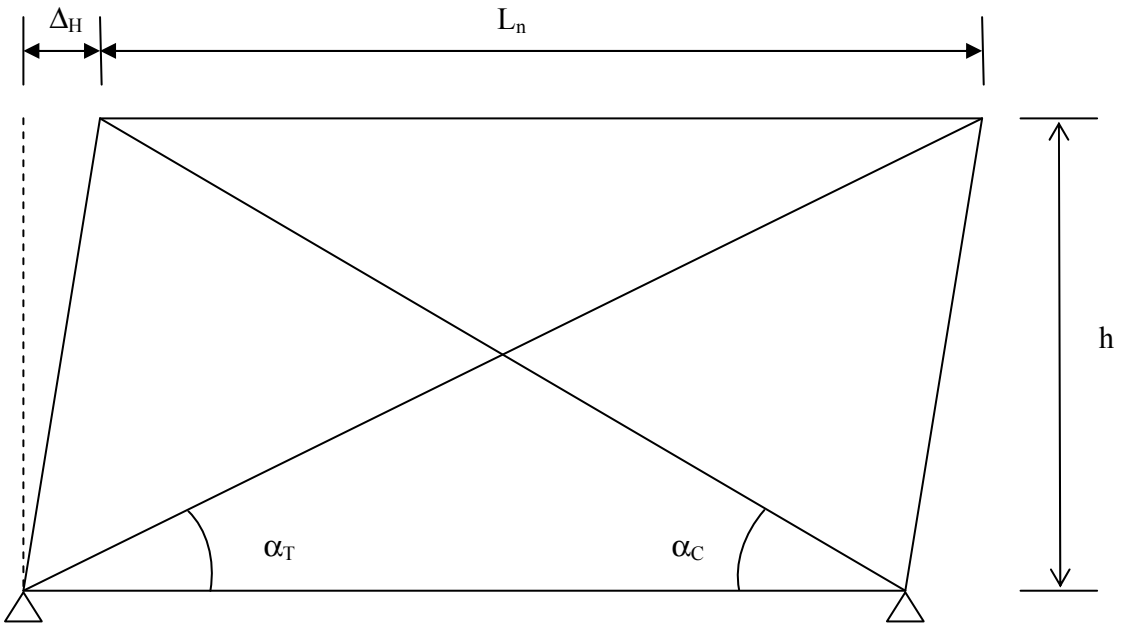

Fig. A.2 Elevation of model in deformed configuration.

Calculating the deformed length of the tension diagonal (Fig. A.2),

$$D_T = \sqrt{h^2 + (L_n + \Delta_H)^2}$$

$$= \sqrt{h_n{}^2 - \Delta_H{}^2 + L_n{}^2 + 2L_n\Delta_H + \Delta_H{}^2}$$

$$= \sqrt{h_n{}^2 + L_n{}^2 + 2L_n\Delta_H}$$

$$= \sqrt{D_0{}^2 + 2L_n\Delta_H{}^2} \qquad \text{(A.1)}$$

$$= D_0\sqrt{1 + 2\frac{L_n}{D_0}\frac{\Delta_H}{D_0}}$$

Similarly, for the compression diagonal,

$$D_C = D_0\sqrt{1 - 2\frac{L_n}{D_0}\frac{\Delta_H}{D_0}} \qquad \text{(A.2)}$$

Calculating the instantaneous angle of the diagonals with the horizontal plane (see Figs. A.1 and A.2 for angle definitions),

$$\sin\alpha_T = \frac{h(\Delta_H)}{D_T(\Delta_H)} \qquad \sin\alpha_C = \frac{h(\Delta_H)}{D_C(\Delta_H)} \qquad \sin\alpha_0 = \frac{h(\Delta_H)}{D_0(\Delta_H)} \qquad \text{(A.3)}$$

Each diagonal consists of four struts with a tie member common to both diagonals.

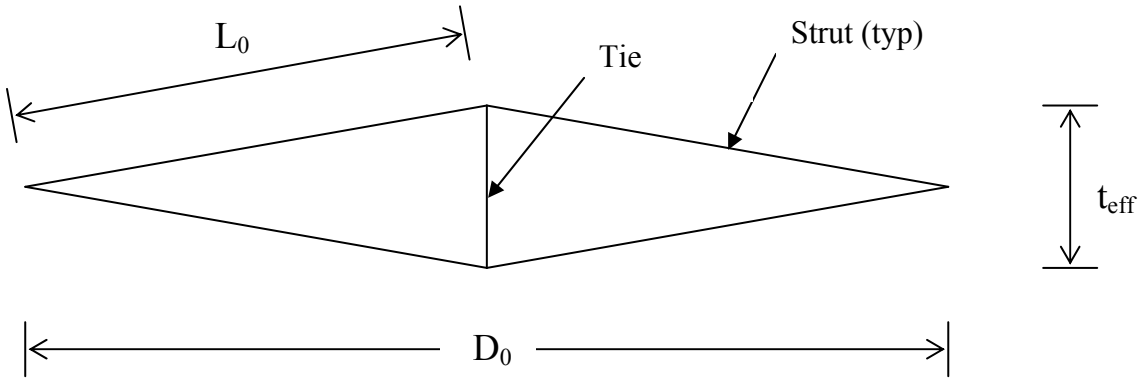

Fig. A.3 Undeformed configuration.

The undeformed length of a strut, from Figure A.3, is defined as

$$L_0 = \sqrt{\left(\frac{D_0}{2}\right)^2 + \left(\frac{t_{eff}}{2}\right)^2} = \frac{1}{2}\sqrt{D_0^{\,2} + t_{eff}^{\,2}} = \frac{1}{2}\sqrt{L_n^{\,2} + h_n^{\,2} + t_{eff}^{\,2}} \qquad \text{(A.4)}$$

t_{eff} = width of the SAT model = 20 in.
(Note that this is not the same definition as used by Hashemi and Mosalam (2007). However, the equations have been changed to account for the difference.)

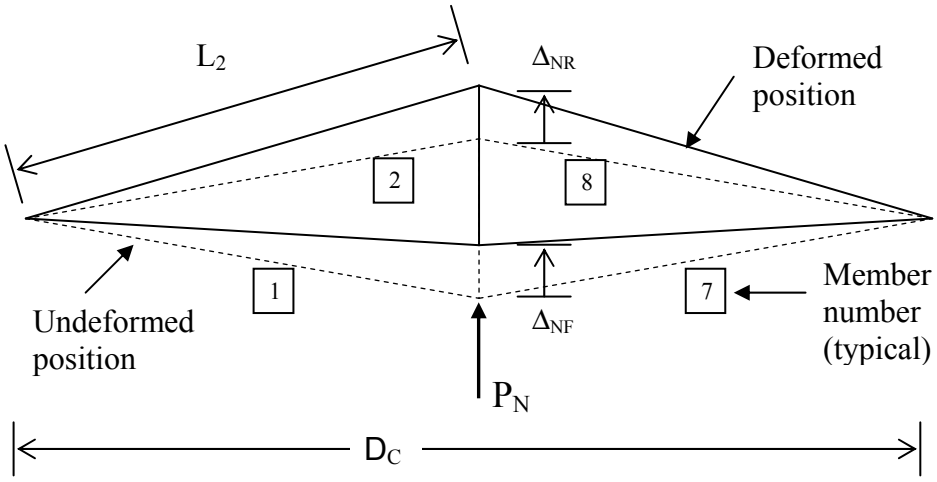

Fig. A.4 Member struts making up compression diagonal, and OOP deformations.

Calculating the instantaneous deformed length of the members in the compression diagonal (see Fig. A.4), taking into account the effect of both the OOP and IP displacement,

$$L_1 = L_7 = \sqrt{\left(\frac{D_C}{2}\right)^2 + \left(\frac{t_{eff}}{2} - \Delta_{NF}\right)^2} = \frac{1}{2}\sqrt{D_C{}^2 + \left(t_{eff} - 2\Delta_{NF}\right)^2} \quad \text{(A.5)}$$

$$L_2 = L_8 = \frac{1}{2}\sqrt{D_C{}^2 + \left(t_{eff} + 2\Delta_{NR}\right)^2} \quad \text{(A.6)}$$

where:

$L_j =$ instantaneous deformed length of the jth strut

$\Delta_{NF} =$ front OOP deflection of the midpoint on the side where the force is applied

$\Delta_{NR} =$ rear OOP deflection of the midpoint on the side opposite where the force is applied

It should be noted that since the tie is a tension-only rigid element, $\Delta_{NR} \le \Delta_{NF}$ and also that the struts are compression-only. Thus, none of the struts in the rear face is able to exert a compression force on the tie as long as the rear face has not experienced "snap-through," defined here as $\Delta_{NR} < - t_{eff} / 2$. However, if one of the rear struts is in compression (as may be caused by IP displacements), it will exert a tension force in the tie, which then leads to $\Delta_{NR} = \Delta_{NF}$. Thus, there are two possibilities in the force-deflection relationship of the SAT model:

1. There is at least one strut in the rear that is in compression, and therefore ΔNR = ΔNF.
2. None of the rear struts is in compression, and therefore $\Delta_{NR} \le \Delta_{NF}$. However, the rear struts will have no forces and will not contribute to the resultant resisting forces in the SAT model. In this case, there is no error in calculating the forces based on the assumption that $\Delta_{NR} = \Delta_{NF}$, since this will simply increase the extension in the rear struts.

The conclusion is that, for reasonable OOP displacements ($< t_{eff}/2 = 10$ in.), there will be no loss of accuracy in the force-displacement relationship if it is assumed that the tie is rigid in tension and compression, and that $\Delta_{NR} = \Delta_{NF} = \Delta_N$. This assumption will be made in the computational analysis, resulting in a two- degree-of-freedom system.

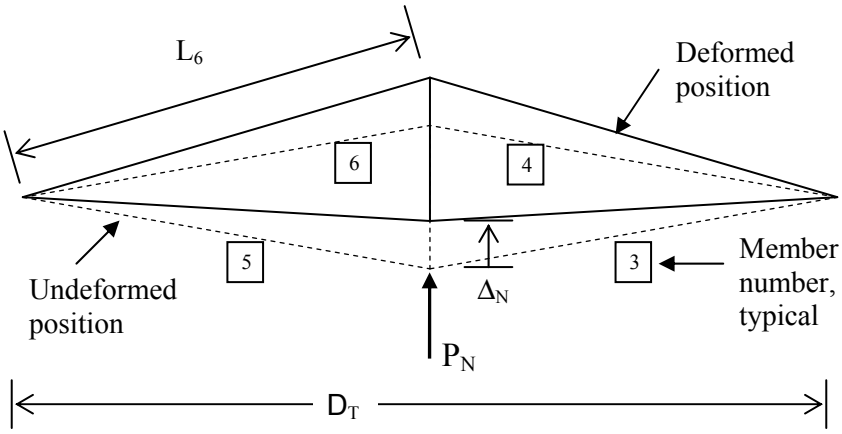

Fig. A.5 Member struts making up tension diagonal, and OOP deformations.

Calculating the instantaneous deformed length of the struts in the tension diagonal (see Fig. A.5), and taking into account the effect of both the OOP and IP displacement,

$$L_5 = L_3 = \sqrt{\left(\frac{D_T}{2}\right)^2 + \left(\frac{t_{eff}}{2} - \Delta_N\right)^2} = \frac{1}{2}\sqrt{D_T{}^2 + \left(t_{eff} - 2\Delta_N\right)^2} \tag{A.7}$$

$$L_6 = L_4 = \frac{1}{2}\sqrt{D_T{}^2 + \left(t_{eff} + 2\Delta_N\right)^2} \tag{A.8}$$

Next, it is necessary to determine the angle that the struts make with a vertical plane located at the center of the SAT model. The β-angles are defined in Figure A.7. Note that the subscript of the β-angle matches the element number:

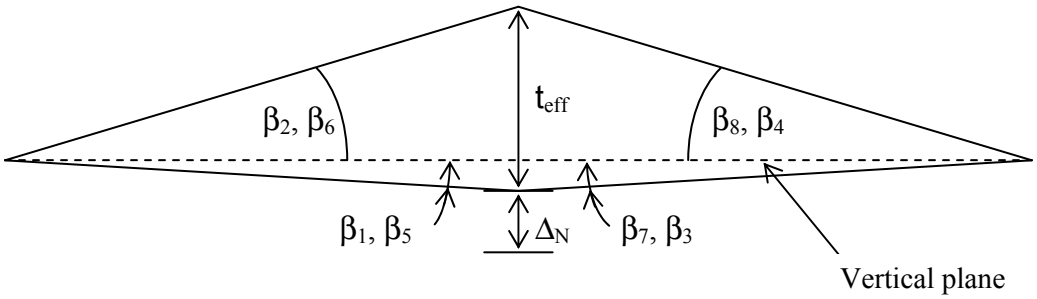

Fig. A.7 Defining β-angles.

$$\sin\beta_1 = \frac{\frac{t_{eff}}{2} - \Delta_N}{L_1} \qquad \sin\beta_2 = \frac{\frac{t_{eff}}{2} + \Delta_N}{L_2} \qquad \sin\beta_3 = \frac{\frac{t_{eff}}{2} - \Delta_N}{L_3}$$

$$\sin\beta_4 = \frac{\frac{t_{eff}}{2} + \Delta_N}{L_4} \qquad \sin\beta_5 = \frac{\frac{t_{eff}}{2} - \Delta_N}{L_5} \qquad \sin\beta_6 = \frac{\frac{t_{eff}}{2} + \Delta_N}{L_6} \tag{A.9}$$

$$\sin\beta_7 = \frac{\frac{t_{eff}}{2} - \Delta_N}{L_7} \qquad \sin\beta_8 = \frac{\frac{t_{eff}}{2} + \Delta_N}{L_8}$$

The static resultant forces on the SAT model, P_H and P_N, will be vector combinations of the forces in the individual struts. The force in a given strut is a function of the strain, measured as the engineering strain, which is a function of the deformation in each strut. The deformation is a function of Δ_H and Δ_N. Accordingly (see Fig. A.8), the force in the jth strut (compression is positive), is given by

$$F_j = \sigma\left(\varepsilon_j(\Delta_H, \Delta_N)\right) \times A_{strut} \tag{A.10}$$

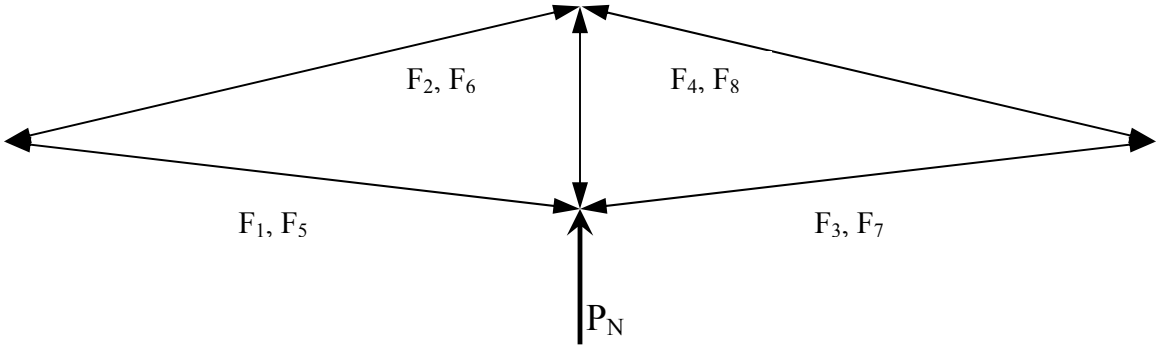

Fig. A.8 Static equilibrium for calculating OOP force, P_N.

$$P_N = -\sum_{j=1}^{8} F_j \sin\beta_j (-1)^j \tag{A.11}$$

where the β-angles are defined in Figure A.7. Note that the odd-numbered struts are on the same side as the load.

Defining (see Fig. A.9),

$P_C =$ IP resultant of forces from struts on the compression diagonal

$P_T =$ IP resultant of forces from struts on the tension diagonal

$T_L =$ Tension in the left vertical rigid member

$T_R =$ Tension in the right vertical rigid member

Therefore,

$$P_C = \sum_{j=1}^{2} F_j \cos\beta_j \qquad P_T = \sum_{j=3}^{4} F_j \cos\beta_j \qquad T_L = P_C \frac{\sin\alpha_C}{\cos\gamma} \qquad T_R = P_T \frac{\sin\alpha_T}{\cos\gamma} \quad \text{(A.12)}$$

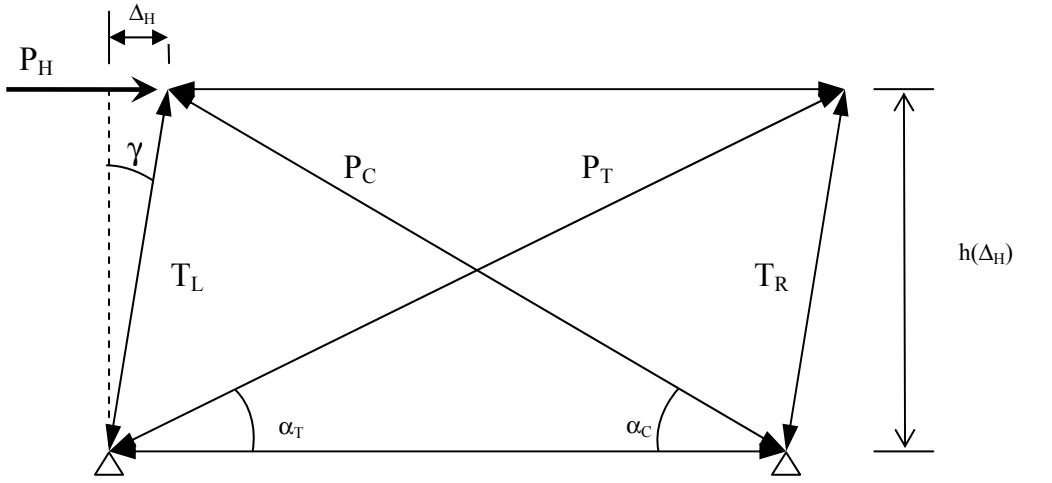

Fig. A.9 Static equilibrium for calculating IP horizontal resultant force, P_H.

Taking the horizontal component of the above four forces, and equilibrating to P_H ,

$$P_H = \left(\sum_{j=1}^{2} F_j \cos\beta_j\right)\left[\cos\alpha_C + \sin\alpha_C \frac{\Delta_H}{h(\Delta_H)}\right] - \left(\sum_{j=3}^{4} F_j \cos\beta_j\right)\left[\cos\alpha_T - \sin\alpha_T \frac{\Delta_H}{h(\Delta_H)}\right] \quad \text{(A.13)}$$

In this equation use has been made, for instance, of the fact that the horizontal component of the tension in the left vertical member is given by

$$T_L \sin\gamma = P_C \frac{\sin\alpha_C}{\cos\gamma} \sin\gamma = \left(\sum_{j=1}^{2} F_j \cos\beta_j\right) \sin\alpha_C \tan\gamma = \left(\sum_{j=1}^{2} F_j \cos\beta_j\right) \sin\alpha_C \frac{\Delta_H}{h(\Delta_H)} \quad \text{(A.14)}$$

A similar term gives the horizontal component of the tension in the right vertical member. The relationships and equations in this appendix are used in calculating the force-displacement relationships given in Appendices B and C.

Appendix B: Evaluation of Hashemi's Model (Displacement-Based Approach)

This Appendix analyzes the in-plane out-of-plane behavior of Hashemi's infill model (Hashemi and Mosalam 2007). For derivations of the equations, see Appendix A.

Case considered: Displacement Controlled Case 1

In-Plane Displacement = 3 in.

Out-of-Plane Displacement = 3 in.

Dimensions of the model:

$L_n := 150\ in$ Length of the panel

$h_n := 101\ in$ Height of the panel

$D_0 := \sqrt{L_n^2 + h_n^2}$ Original, unstressed length of the diagonal

$D_0 = 180.834\ in$

$t_{eff} := 20\ in$ Effective thickness of the model (out-to-out)

$A_{strut} := 21.22\ in^2$ Area (assumed) for each of the eight struts

Strength and deformation parameters of the model:

$\varepsilon_{mo} := 0.0028$ These three parameters match those from Hashemi and Mosalam (2007)

$f_{mo} := 2.46\ ksi$

$\varepsilon_y := 2 \cdot \varepsilon_{mo}$

Number of strut elements:

$N_{elem} := 8$

$i := 1 .. N_{elem}$

Input the prescribed displacement sequence: Major points for the in-plane displacement:

$Delta_H := (0.0 \quad 3.0)^T\ in$

Major points for the out-of-plane displacement sequence:

$\text{Delta}_N := (\ 0.0 \quad 3.0\ )^T \text{ in}$

Note that the corresponding displacement points are assumed to occur together (in-phase)

$N_{sub} := 100$

Number of subdivisions between major points. Again, the corresponding subdivision points are assumed to occur together.

Fill in the intermediate points:

$N_{points} := \left(\text{rows}\left(\text{Delta}_H\right) - 1\right) \cdot \left(N_{sub}\right) + 1$

$N_{points} = 101$

Number of rows in the full displacement matrix

Check to make sure that there are the same number of major points for the in-plane and out-of-plane displacements. Make N_{points} an imaginary number if not, so that the analysis will not continue.

$N_{points} := \text{if}\left(\text{rows}\left(\text{Delta}_H\right) = \text{rows}\left(\text{Delta}_N\right), N_{points}, 1 \cdot i\right) \qquad N_{points} = 101$

$$\Delta_H := \left| \begin{array}{l} \text{for } k \in 1 .. \text{rows}\left(\text{Delta}_H\right) \\ \quad \Delta H_{1+(k-1)\cdot N_{sub}} \leftarrow \text{Delta}H_k \\ \text{for } k \in 1 .. \left(\text{rows}\left(\text{Delta}_H\right) - 1\right) \\ \quad \text{for } r \in 1 .. N_{sub} - 1 \\ \quad\quad \Delta H_{1+(k-1)\cdot N_{sub}+r} \leftarrow \Delta H_{1+(k-1)\cdot N_{sub}} + \frac{r}{N_{sub}} \cdot \left[\Delta H_{1+k\cdot N_{sub}} - \Delta H_{1+(k-1)\cdot N_{sub}}\right] \\ \Delta_H \end{array} \right.$$

$$\Delta_N := \left| \begin{array}{l} \text{for } k \in 1 .. \text{rows}\left(\text{Delta}_N\right) \\ \quad \Delta N_{1+(k-1)\cdot N_{sub}} \leftarrow \text{Delta}N_k \\ \text{for } k \in 1 .. \left(\text{rows}\left(\text{Delta}_N\right) - 1\right) \\ \quad \text{for } r \in 1 .. N_{sub} - 1 \\ \quad\quad \Delta N_{1+(k-1)\cdot N_{sub}+r} \leftarrow \Delta N_{1+(k-1)\cdot N_{sub}} + \frac{r}{N_{sub}} \cdot \left[\Delta N_{1+k\cdot N_{sub}} - \Delta N_{1+(k-1)\cdot N_{sub}}\right] \\ \Delta_N \end{array} \right.$$

$j := 1 .. N_{points}$

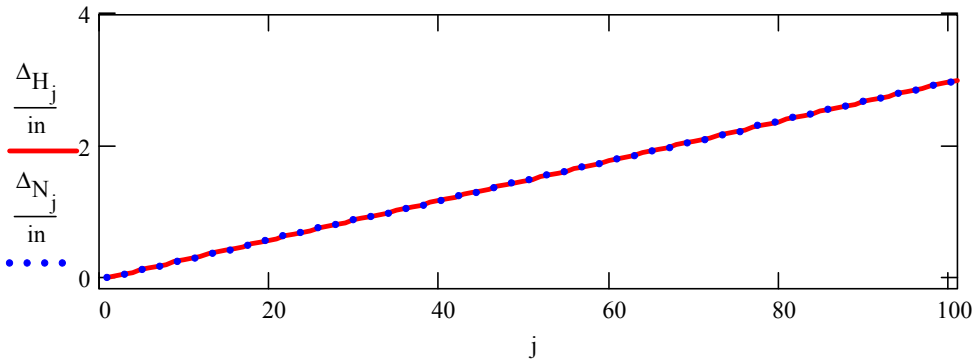

Calculate the deformations and strains in the model:

$h(\Delta_H) := \sqrt{h_n^2 - \Delta_H^2}$ Instantaneous height of the panel

$D_T(\Delta_H) := D_0 \cdot \sqrt{1 + \frac{2 \cdot L_n \cdot \Delta_H}{D_0^2}}$ Instantaneous length of the tension diagonal

$D_C(\Delta_H) := D_0 \cdot \sqrt{1 - \frac{2 \cdot L_n \cdot \Delta_H}{D_0^2}}$ Instantaneous length of the compression diagonal

$L_0 := \frac{1}{2} \cdot \sqrt{L_n^2 + h_n^2 + t_{eff}^2}$ Unstressed original length of an individual strut

$L_0 = 90.968$ in

Calculate the instantaneous angle that the diagonals make with the horizontal:

$\alpha_T(\Delta_H) := \text{asin}\left(\frac{h(\Delta_H)}{D_T(\Delta_H)}\right)$ $\alpha_T(1\text{ in}) = 33.776$ deg

$\alpha_C(\Delta_H) := \text{asin}\left(\frac{h(\Delta_H)}{D_C(\Delta_H)}\right)$ $\alpha_C(1\text{ in}) = 34.13$ deg

Initial angle: $\alpha_0 := \operatorname{asin}\left(\frac{h_n}{D_0}\right)$ $\alpha_0 = 33.954 \quad \text{deg}$

Calculate the instantaneous length of the struts, including both the in-plane and the out-of-plane displacements:

$$f\_L(\Delta_H, \Delta_N) := \begin{bmatrix} \frac{1}{2}\cdot\sqrt{D_C(\Delta_H)^2 + (t_{eff} - 2\cdot\Delta_N)^2} \\ \frac{1}{2}\cdot\sqrt{D_C(\Delta_H)^2 + (t_{eff} + 2\cdot\Delta_N)^2} \\ \frac{1}{2}\cdot\sqrt{D_T(\Delta_H)^2 + (t_{eff} - 2\cdot\Delta_N)^2} \\ \frac{1}{2}\cdot\sqrt{D_T(\Delta_H)^2 + (t_{eff} + 2\cdot\Delta_N)^2} \\ \frac{1}{2}\cdot\sqrt{D_T(\Delta_H)^2 + (t_{eff} - 2\cdot\Delta_N)^2} \\ \frac{1}{2}\cdot\sqrt{D_T(\Delta_H)^2 + (t_{eff} + 2\cdot\Delta_N)^2} \\ \frac{1}{2}\cdot\sqrt{D_C(\Delta_H)^2 + (t_{eff} - 2\cdot\Delta_N)^2} \\ \frac{1}{2}\cdot\sqrt{D_C(\Delta_H)^2 + (t_{eff} + 2\cdot\Delta_N)^2} \end{bmatrix}$$

Instantaneous lengths of the struts

$f\_L(1.0\ \text{in}, 0\ \text{in})^T = (90.555 \quad 90.555 \quad 91.38 \quad 91.38 \quad 91.38 \quad 91.38 \quad 90.555 \quad 90.555)\ \text{in}$

$\Delta_{Nplot} := 0.0\ \text{in}, 0.01 \cdot t_{eff} .. 0.5 \cdot t_{eff}$

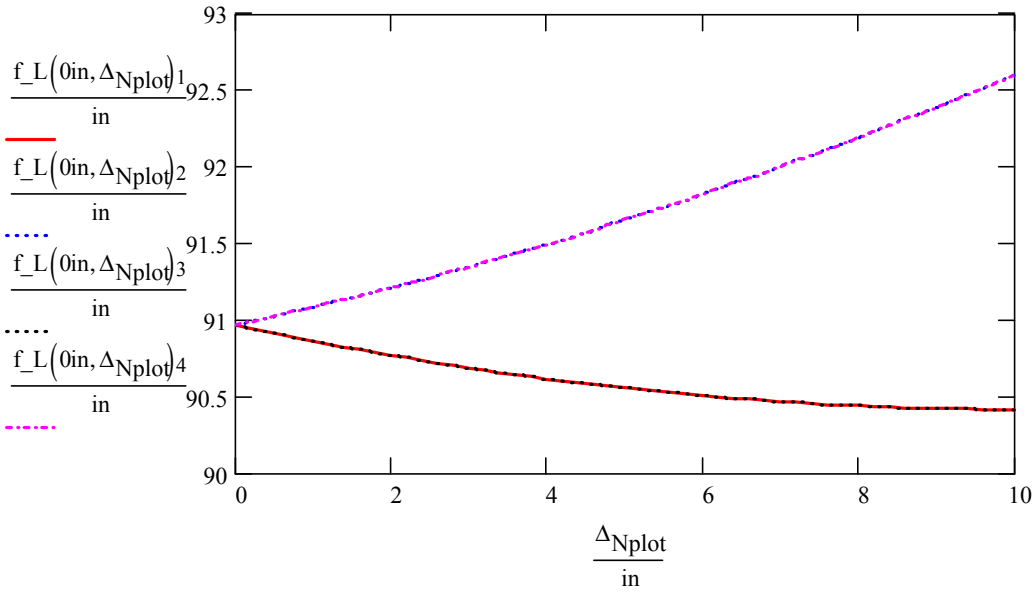

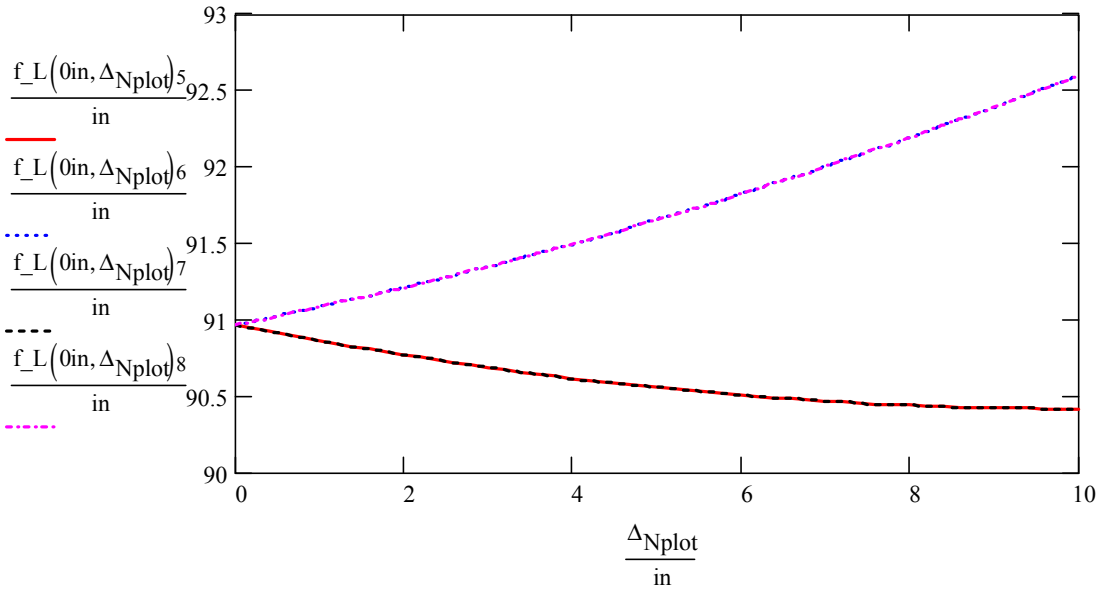

Calculate the strains in the struts. Compressive strain is positive.

$$f\_\varepsilon(\Delta_H,\Delta_N) := \left| \begin{array}{l} \text{for } i \in 1..8 \\ \quad \varepsilon_i \leftarrow \dfrac{L_0 - f\_L(\Delta_H,\Delta_N)_i}{L_0} \\ \varepsilon \end{array} \right.$$

Calculate the stresses in the individual struts as a function of the strains. Compressive stress is positive.

$$f\_1\_\sigma(\varepsilon) := f_{mo}\cdot\left[2\cdot\left(\frac{\varepsilon}{\varepsilon_y}\right) - \left(\frac{\varepsilon}{\varepsilon_y}\right)^2\right]$$

Make the stress-strain relationship compression-only:

$$f\_\sigma(\varepsilon) := \text{if}\left(\varepsilon < 0.0\text{ksi}, 0.0, \text{if}\left(\varepsilon > 2.0\cdot\varepsilon_y, 0.0, f\_1\_\sigma(\varepsilon)\right)\right)$$

$$f\_\beta(\Delta_H,\Delta_N) := \begin{pmatrix} \text{asin}\left(\dfrac{\frac{t_{eff}}{2} - \Delta_N}{f\_L(\Delta_H,\Delta_N)_1}\right) \\ \text{asin}\left(\dfrac{\frac{t_{eff}}{2} + \Delta_N}{f\_L(\Delta_H,\Delta_N)_2}\right) \\ \text{asin}\left(\dfrac{\frac{t_{eff}}{2} - \Delta_N}{f\_L(\Delta_H,\Delta_N)_3}\right) \\ \text{asin}\left(\dfrac{\frac{t_{eff}}{2} + \Delta_N}{f\_L(\Delta_H,\Delta_N)_4}\right) \\ \text{asin}\left(\dfrac{\frac{t_{eff}}{2} - \Delta_N}{f\_L(\Delta_H,\Delta_N)_5}\right) \\ \text{asin}\left(\dfrac{\frac{t_{eff}}{2} + \Delta_N}{f\_L(\Delta_H,\Delta_N)_6}\right) \\ \text{asin}\left(\dfrac{\frac{t_{eff}}{2} - \Delta_N}{f\_L(\Delta_H,\Delta_N)_7}\right) \\ \text{asin}\left(\dfrac{\frac{t_{eff}}{2} + \Delta_N}{f\_L(\Delta_H,\Delta_N)_8}\right) \end{pmatrix}$$

Beta angles between the individual struts and the vertical plane.

Calculate the force in each strut as a function of displacement. Compression is positive.

$$f\_F(\Delta_H,\Delta_N) := \left| \begin{array}{l} \text{for } i \in 1..N_{elem} \\ \quad F_i \leftarrow f\_\sigma\left(f\_\varepsilon(\Delta_H,\Delta_N)_i\right)\cdot A_{strut} \\ F \end{array} \right.$$

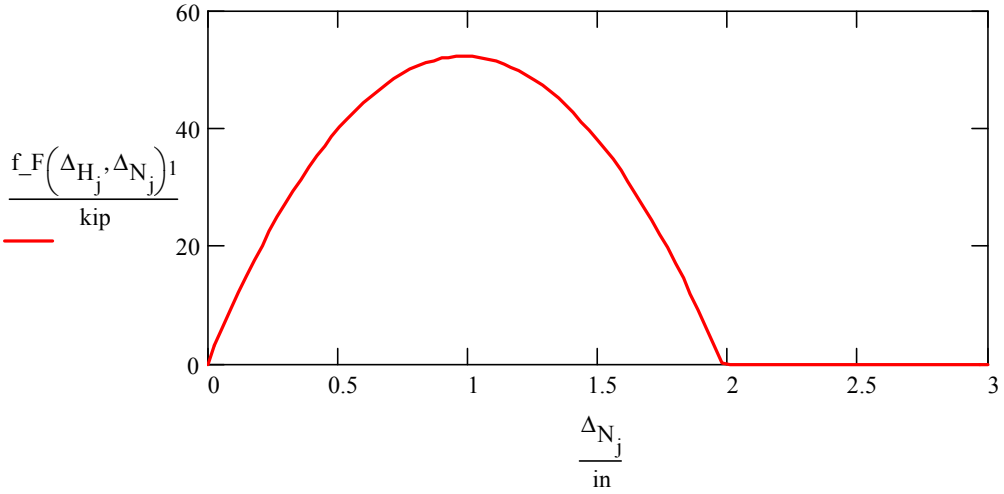

Calculate the in-plane force as a function of displacements:

$$P_H(\Delta_H,\Delta_N) := \left[\sum_{i=1}^{2}\left[\left[\left(f\_F(\Delta_H,\Delta_N)_i\right)\cdot\cos\left(f\_\beta(\Delta_H,\Delta_N)\right)_i\right]\cdot\begin{pmatrix}\cos\left(\alpha_C(\Delta_H)\right) & \dots \\ +\sin\left(\alpha_C(\Delta_H)\right)\cdot\dfrac{\Delta_H}{h(\Delta_H)}\end{pmatrix}\right]\right] \dots$$
$$+(-1)\cdot\sum_{i=3}^{4}\left[\left(f\_F(\Delta_H,\Delta_N)_i\cdot\cos\left(f\_\beta(\Delta_H,\Delta_N)\right)_i\right)\cdot\begin{pmatrix}\cos\left(\alpha_T(\Delta_H)\right) & \dots \\ +-\sin\left(\alpha_T(\Delta_H)\right)\cdot\dfrac{\Delta_H}{h(\Delta_H)}\end{pmatrix}\right]$$

Calculate the out-of-plane force as a function of displacements:

$$P_N(\Delta_H,\Delta_N) := \sum_{i=1}^{8}\left[\left(f\_F(\Delta_H,\Delta_N)_i\cdot\sin\left(f\_\beta(\Delta_H,\Delta_N)_i\right)\right)(-1)\cdot(-1)^i\right]$$

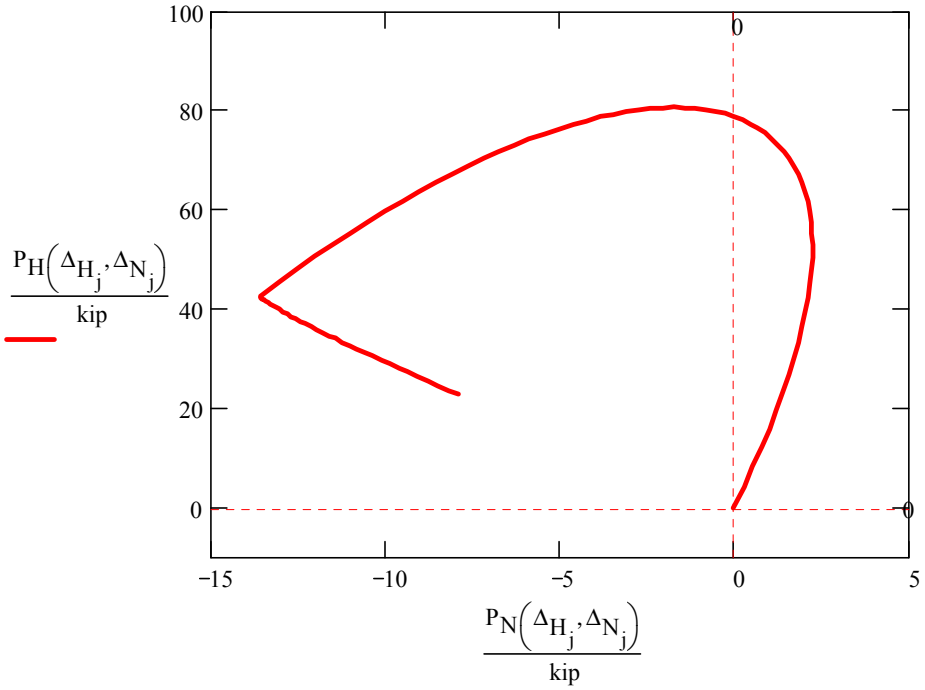
100
80
60
40
20
0
0
0
−15
−10
−5
0
5
$\frac{P_H(\Delta_{H_j},\Delta_{N_j})}{kip}$
$\frac{P_N(\Delta_{H_j},\Delta_{N_j})}{kip}$

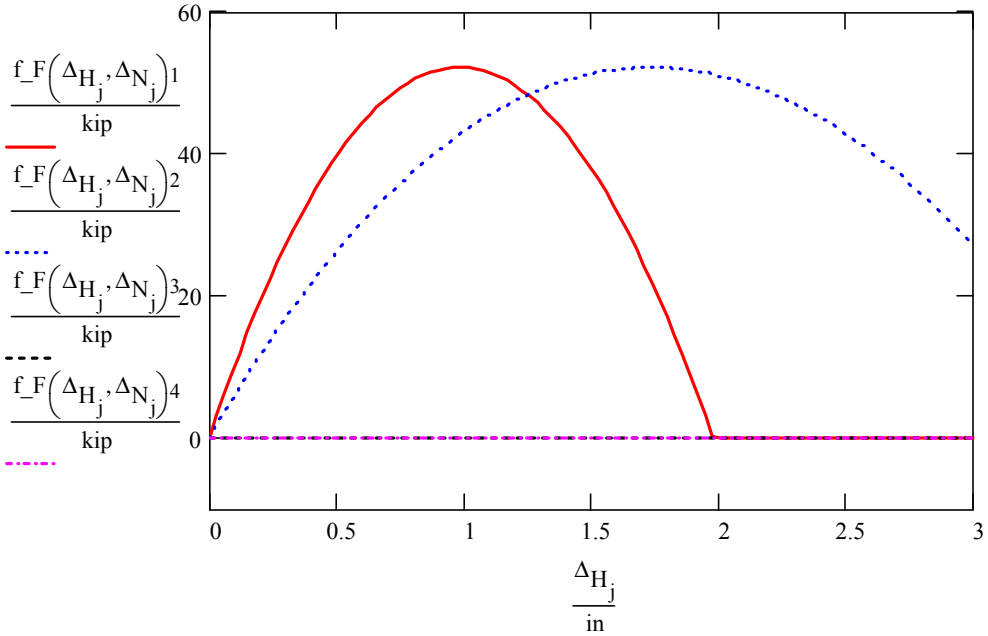
60
40
20
0
0
0.5
1
1.5
2
2.5
3
$\frac{f\_F(\Delta_{H_j},\Delta_{N_j})_1}{kip}$
$\frac{f\_F(\Delta_{H_j},\Delta_{N_j})_2}{kip}$
$\frac{f\_F(\Delta_{H_j},\Delta_{N_j})_3}{kip}$
$\frac{f\_F(\Delta_{H_j},\Delta_{N_j})_4}{kip}$
$\frac{\Delta_{H_j}}{in}$

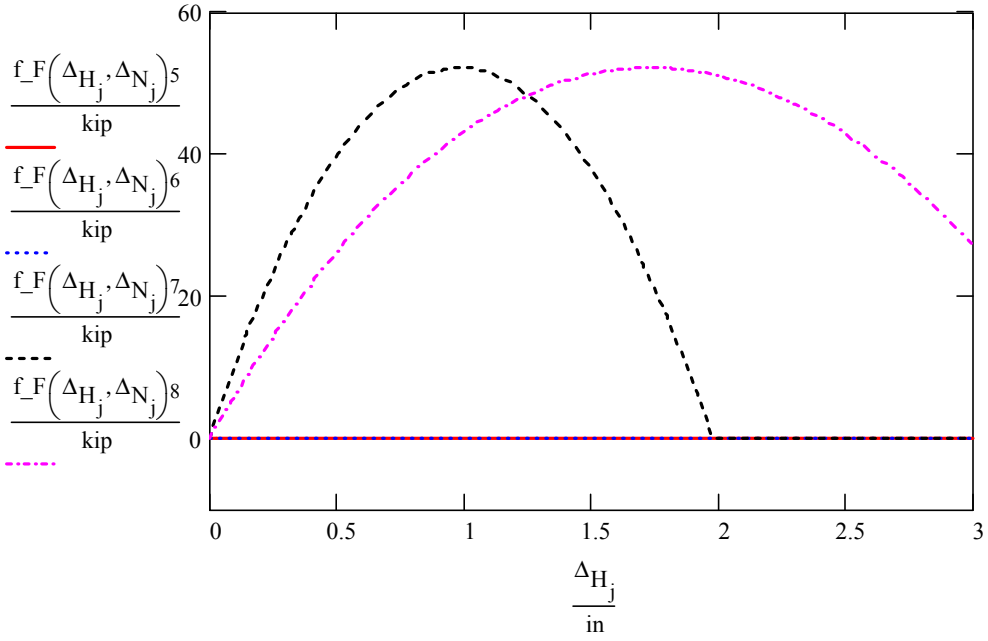
60
40
20
0
0
0.5
1
1.5
2
2.5
3
f_F(Δ_Hj, Δ_Nj)5 / kip
f_F(Δ_Hj, Δ_Nj)6 / kip
f_F(Δ_Hj, Δ_Nj)7 / kip
f_F(Δ_Hj, Δ_Nj)8 / kip
Δ_Hj / in

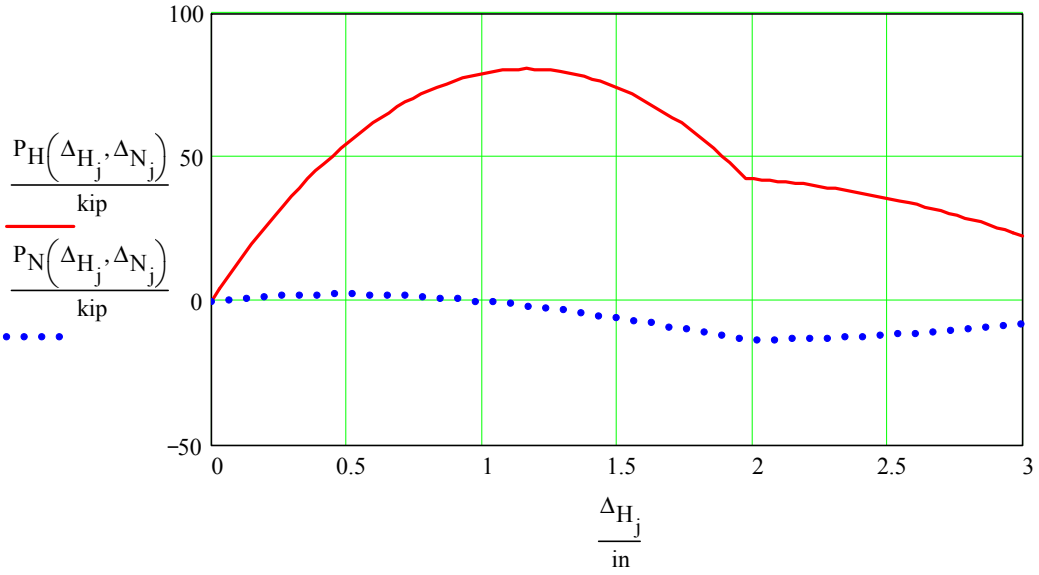
100
50
0
−50
0
0.5
1
1.5
2
2.5
3
P_H(Δ_Hj, Δ_Nj) / kip
P_N(Δ_Hj, Δ_Nj) / kip
Δ_Hj / in

Appendix C: Evaluation of Hashemi's Model (In-Plane Controlled Displacement, Out-of-Plane Constant Force)

This workbook analyzes the in-plane / out-of-plane behavior of the Hashemi Infill Model (Hashemi and Mosalam 2007). For a derivation of the equations used here, see Appendix A.

Case considered:

Displacement Controlled In-Plane, Force Controlled
Out-of-plane Case 11
Out-of-Plane Force = 7.5 kips
Constant Out-of-Plane Force

Constant out-of-plane force to be applied throughout the pushover sequence

$F_N := 7.5\ kip$

$N_{sub} := 100$ Number of subdivisions between major points.

Note: For brevity, input data and equations that are identical to those used in Appendix B are not repeated here.

Step 1: First Calculate the maximum value of in-plane displacement which may be reached, given the out-of-plane force specified. This is done graphically:

Case considered:

Displacement Controlled In-Plane, Force Controlled
Out-of-plane Case 11
Out-of-Plane Force = 7.5 kips
Constant Out-of-Plane Force

Constant out-of-plane force to be applied throughout the pushover sequence

$F_N := 7.5\ kip$

$N_{sub} := 100$ Number of subdivisions between major points.

Note: For brevity, input data and equations that are identical to those used in Appendix B are not repeated here.

Step 1: First Calculate the maximum value of in-plane displacement which may be reached, given the out-of-plane force specified. This is done graphically:

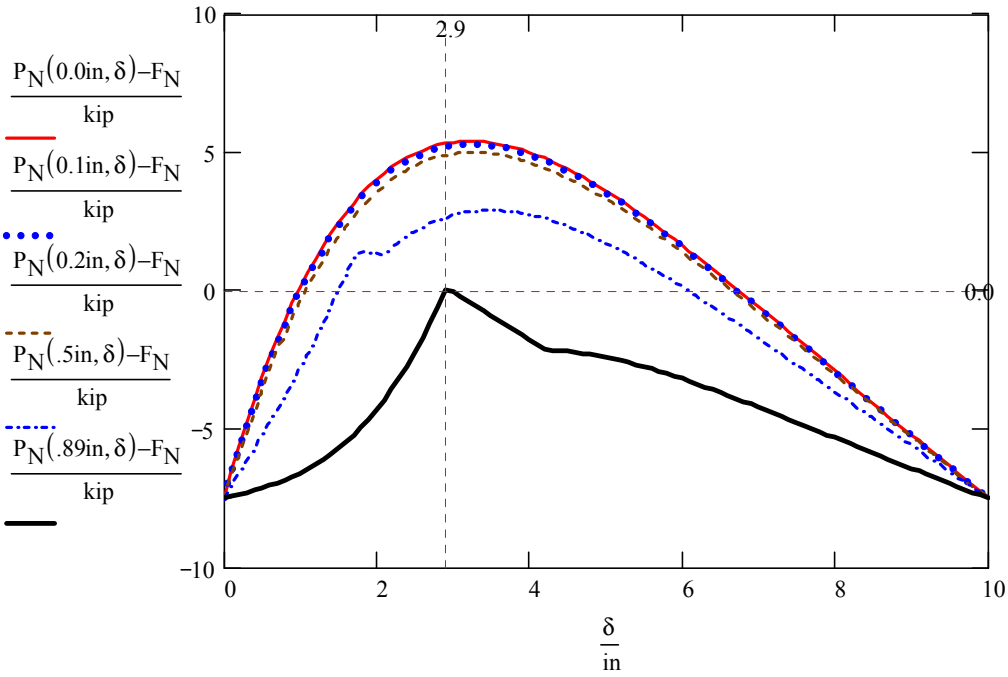

$\Delta_{H\_max} := 0.89\ in$ Found graphically: this is the maximum value of in-plane displacement for a given out-of-plane force, for which a solution exists

$\Delta_{N\_max} := 2.9\ in$ Found graphically: this is the highest upper estimate of out-of-plane displacement.

Major Points for the in-plane displacement:

$Delta_H := (0.0in\ \ \Delta_{H\_max})^T$

Fill in the intermediate points: Number of rows in the full displacement matrix

$N_{points} := (rows(Delta_H) - 1)\cdot(N_{sub}) + 1$

$N_{points} = 101$

$$\Delta_H := \left| \begin{array}{l} \text{for } k \in 1 .. \text{rows}\left(\text{Delta}_H\right) \\ \quad \Delta H_{1+(k-1)\cdot N_{sub}} \leftarrow \text{Delta}H_k \\ \text{for } k \in 1 .. \left(\text{rows}\left(\text{Delta}_H\right) - 1\right) \\ \quad \text{for } r \in 1 .. N_{sub} - 1 \\ \quad\quad \Delta H_{1+(k-1)\cdot N_{sub}+r} \leftarrow \Delta H_{1+(k-1)\cdot N_{sub}} + \frac{r}{N_{sub}} \cdot \left[\Delta H_{1+k\cdot N_{sub}} - \Delta H_{1+(k-1)\cdot N_{sub}}\right] \\ \Delta_H \end{array} \right.$$

$$j := 1 .. N_{points}$$

Step 2: Calculate the out-of-plane displacement at each value of in-plane displacement:

$$\Delta_N := \left| \begin{array}{l} \text{for } j \in 1 .. N_{points} \\ \quad \Delta N_j \leftarrow \text{root}\left(P_N\left(\Delta H_j, \Delta_N\right) - F_N, \Delta_N, 0.0\text{in}, \Delta_{N\_max}\right) \\ \Delta_N \end{array} \right.$$

Plot the displacement path:

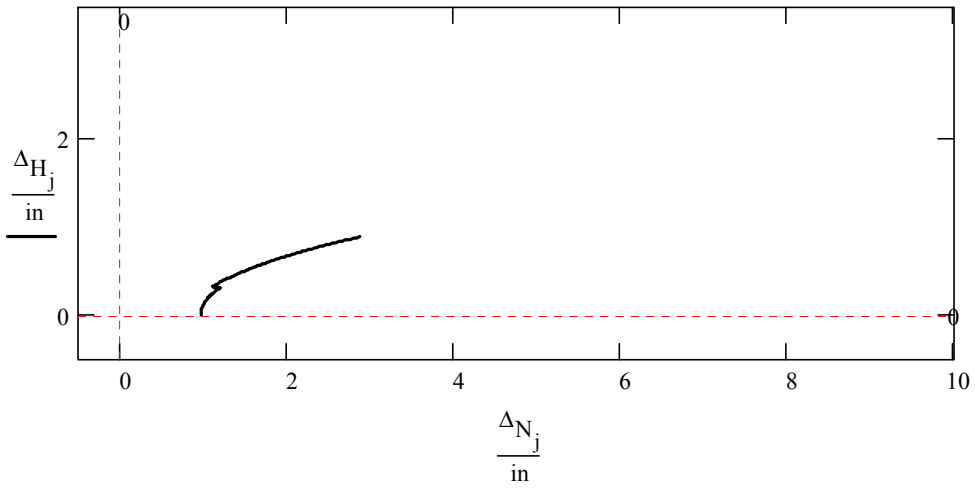

Plot the number of members in compression as a function of displacement:

$$N_{comp} := \left| \begin{array}{l} \text{for } j \in 1 .. N_{points} \\ \quad N_{comp_j} \leftarrow \sum_{i=1}^{N_{elem}} \text{if}\left(f\_F\left(\Delta H_j, \Delta N_j\right)_i > 0.0, 1.0, 0.0\right) \\ N_{comp} \end{array} \right.$$

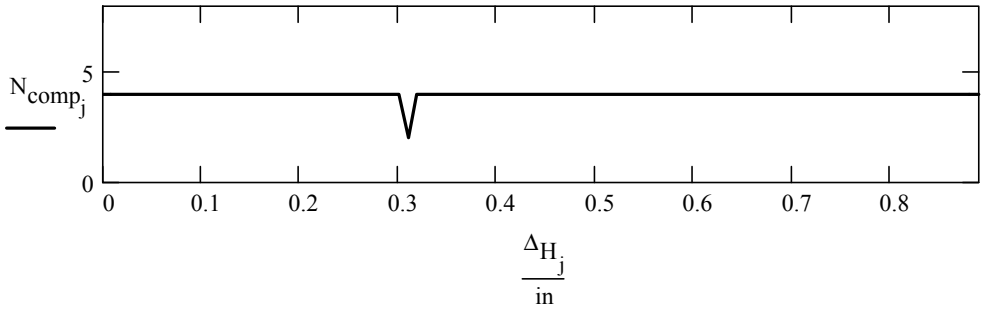

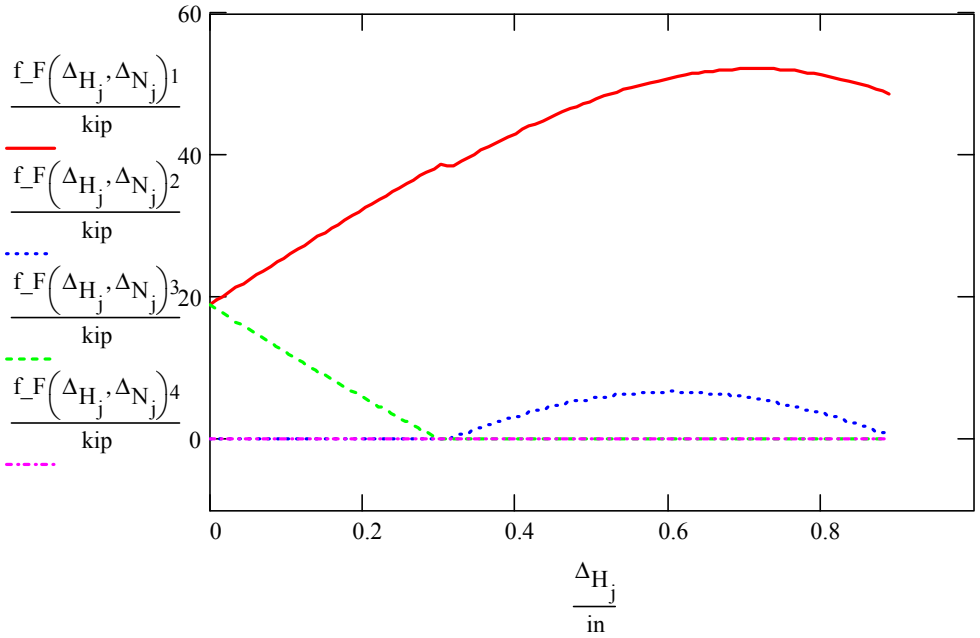

$$P_{N\_alt}(\Delta H, \Delta N) := \sum_{i=1}^{N_{elem}} \left[f\_F_N(\Delta H, \Delta N)_i \cdot (-1)^{i+1} \right]$$

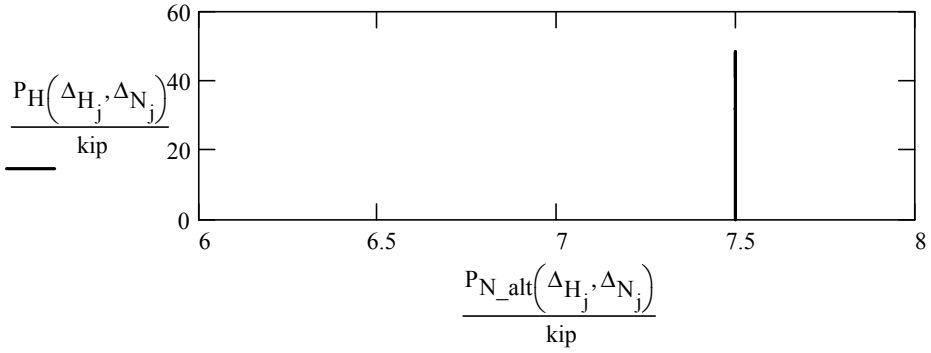

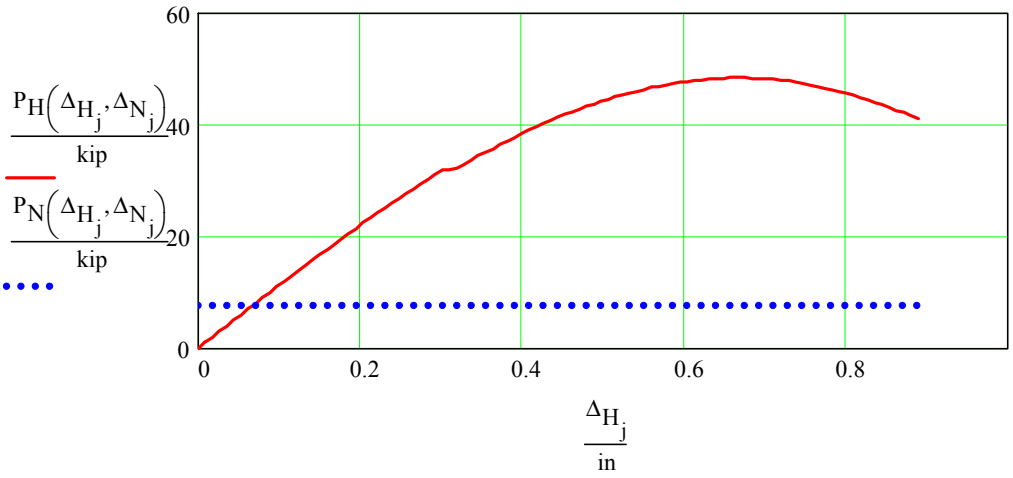
60
40
20
0
$\frac{P_H(\Delta_{H_j},\Delta_{N_j})}{kip}$
$\frac{P_N(\Delta_{H_j},\Delta_{N_j})}{kip}$
0
0.2
0.4
0.6
0.8
$\frac{\Delta_{H_j}}{in}$

Appendix D: Development of an Equivalent Model for Out-of-Plane Behavior of URM Infill Panel

The purpose of this appendix is to present some details of the development of the equivalent infill panel model used in Chapter 3. As shown in Figure D.1, a diagonal member with an out-of-plane (OOP) mass at its midpoint is used to represent both the in-plane (IP) and OOP behavior of the infill panel. This appendix discusses the calculation of the OOP elastic and inelastic properties of the beam-column element, as well as the value of OOP mass to place at the midpoint.

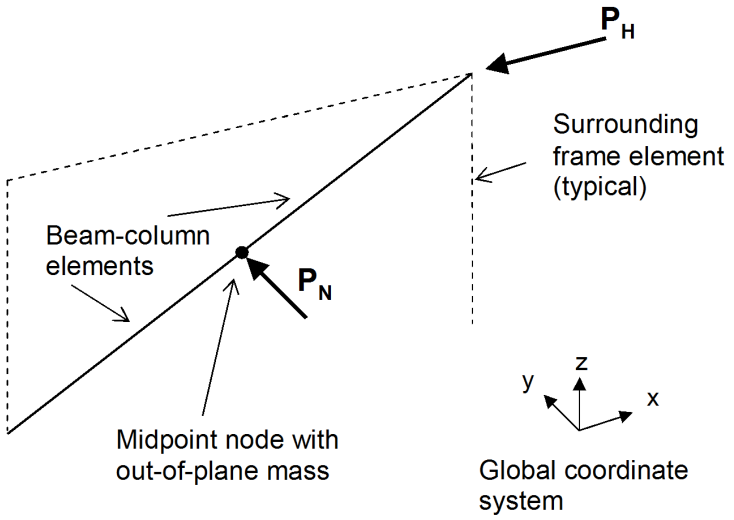

Fig. D.1 Proposed infill model using beam-column elements with fiber discretization.

The purpose of introducing the OOP mass and selecting the beam-column properties is to accurately represent the inertial and stiffness properties of the URM infill wall panel. This is performed keeping in mind that the infill panel model is part of a larger model of the structure in which the panel is located.

The infill wall panel in this study is a single wythe wall with a nominal thickness of 4 in., and with a weight per unit area of approximately 40 psf. The wall is assumed to span in the vertical direction, with simple supports at the top and bottom (where it connects to the floor beams). It is further assumed that its dynamic response to OOP motions at the floor levels can be accounted for by considering only its first mode of vibration. Note that these assumptions already represent a significant idealization (yet reasonable for design purposes) of the actual behavior.

It is desired to represent the OOP behavior of the infill wall with the OOP properties of the equivalent diagonal member, in which the mass is lumped at the midspan, and the member, instead of spanning vertically, spans diagonally. Conceptually, the two systems may be viewed as shown in Figure D.2. Note that the infill wall height, h, is defined elsewhere in this report as h_{inf}. The subscript is omitted here for convenience.

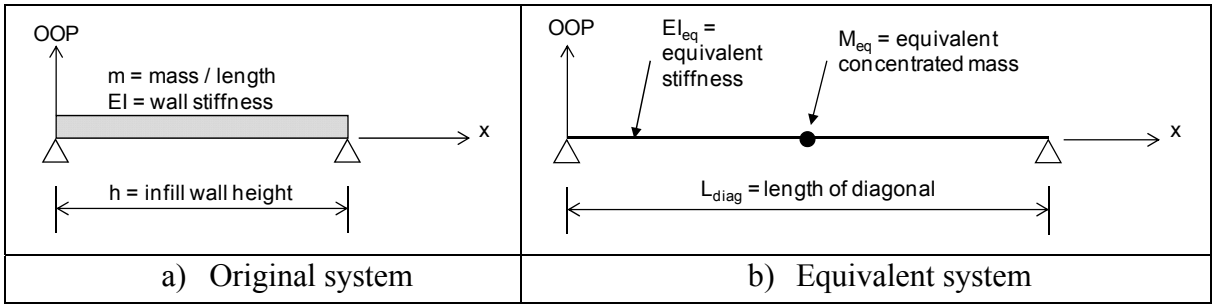

Fig. D.2 Original versus equivalent systems for OOP response.

It is assumed that the support motions for the two systems are equal, despite the fact that they are attached to slightly different locations in the overall structure. This implies that the floor diaphragms are stiff, with little, i.e., negligible, torsional motion.

There are several objectives in the development of the equivalent model. The model should have the same natural frequency as the infill wall. Locally, the model should produce the same support reactions, where it is attached to the surrounding frame, for a given support motion. Moreover, it should exhibit initial yielding at the same level of support motion that causes the original infill wall to yield.

The natural frequency of the original system (the URM wall spanning vertically, as described above in Fig. D.2a) can be determined from the well-known equation of motion for a distributed-mass elastic system without damping, assuming non-moving supports (Chopra 2007):

$$m\frac{\partial^2 u}{\partial t^2} + EI\frac{\partial^4 u}{\partial x^4} = 0 \tag{D.1}$$

By assuming a solution of the form:

$$u(x,t) = \phi(x)q(t) \tag{D.2}$$

Substituting into Equation (D.1), using the method of separation of variables, the following equations are derived:

$$\ddot{q}(t) + \omega^2 q(t) = 0 \qquad \frac{\partial^4 \phi(x)}{\partial x^4} + \frac{m\omega^2}{EI}\phi(x) = 0 \tag{D.3}$$

Solving Equation (D.3b) and applying the simple support boundary conditions leads to the mode shapes:

$$\phi_i(x) = C_i \sin\left(\frac{i\pi}{h}x\right) i = 1, 2, 3,... \tag{D.4}$$

The general solution is:

$$u(x,t) = \sum_{i=1}^{\infty} \phi_i(x) q_i(t) \tag{D.5}$$

Assuming that the response can be described by the first mode only, the mode shape and circular natural frequency are:

$$\phi_1(x) = C_1 \sin\left(\frac{\pi}{h}x\right) \qquad \text{and} \qquad \omega_1 = \frac{\pi^2}{h^2}\sqrt{\frac{EI}{m}} \tag{D.6}$$

Note that $\phi_1(x)$ is symmetric with respect to the beam midspan. For the base excitation problem, consider the infill wall to experience deflections at the supports as shown in Figure D.3. In this figure, $u_L(t)$ and $u_R(t)$ are the absolute support motions (displacements relative to an inertial reference frame), of the left and right support points, respectively, and $u^t(x,t)$ is the absolute displacement of the beam at an arbitrary point x along the wall height.

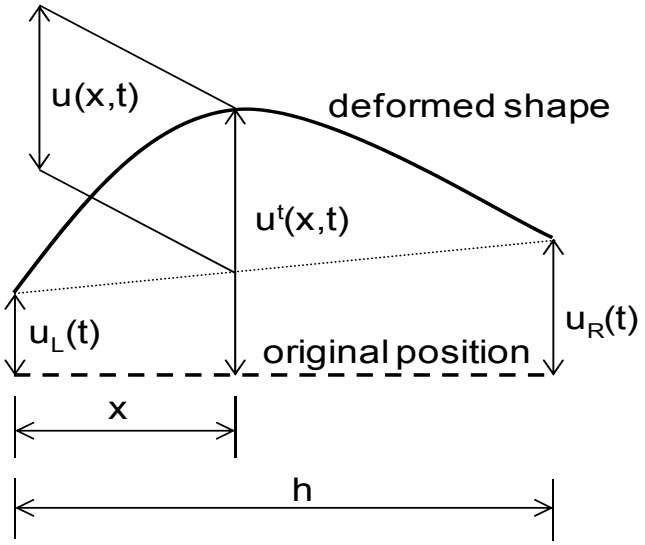

Fig. D.3 First-mode deformation of original system with base excitation.

If we define the relative displacement, $u(x,t)$, of an arbitrary point on the beam as its displacement from the instantaneous tangent joining the left and right supports, we have:

$$u^t(x,t) = u(x,t) + u_L(t) + [u_R(t) - u_L(t)]\frac{x}{h} \qquad \text{or}$$

$$u^t(x,t) = \frac{1}{2}[u_L(t) + u_R(t)] - [u_L(t) - u_R(t)]\left(\frac{x}{h} - \frac{1}{2}\right) + u(x,t) \tag{D.7}$$

Note that the first term on the RHS is constant with respect to x, and that the second term is anti-symmetric about the midspan, $x = h/2$. In terms of the absolute accelerations, the equation of motion for the support excitation problem is:

$$m\frac{\partial^2 u^t}{\partial t^2} + EI\frac{\partial^4 u^t}{\partial x^4} = 0 \tag{D.8}$$

Applying Equation (D.7) to each term in Equation (D.8) gives:

$$m\frac{\partial^2 u}{\partial t^2} + EI\frac{\partial^4 u}{\partial x^4} = -m\left\{\frac{1}{2}[\ddot{u}_L(t) + \ddot{u}_R(t)] - [\ddot{u}_L(t) - \ddot{u}_R(t)]\left(\frac{x}{h} - \frac{1}{2}\right)\right\} \tag{D.9}$$

Substituting Equation (D.5) into Equation (D.9), multiplying both sides by $\phi_1(x)$ and integrating over the length of the beam, then applying the orthogonality conditions yields:

$$\begin{aligned}\left[\ddot{q}_1(t) + \omega_1^2 q_1(t)\right]\int_{x=0}^{h} m\phi_1^2(x)dx = & -\frac{1}{2}[\ddot{u}_L(t) + \ddot{u}_R(t)]\int_{x=0}^{h} m\phi_1(x)dx \\ & + [\ddot{u}_L(t) - \ddot{u}_R(t)]\int_{x=0}^{h} m\phi_1(x)\left(\frac{x}{h} - \frac{1}{2}\right)dx\end{aligned} \tag{D.10}$$

The second integral on the RHS is zero, since the integrand is the product of a function which is symmetric about the midspan, and another function which is anti-symmetric, and the limits of integration are symmetric. Define the participation factor as follows:

$$\Gamma_1 = \frac{\int_{x=0}^{h} m\phi_1(x)dx}{\int_{x=0}^{h} m\phi_1{}^2(x)dx} \tag{D.11}$$

Taking $C_1 = 1$ (i.e., the maximum ordinate of mode shape equals unity) gives $\Gamma_1 = 1.2732$. Accordingly, Equation (D.10) becomes:

$$\ddot{q}_1(t) + \omega_1^2 q_1(t) = -\left[\frac{\ddot{u}_L(t) + \ddot{u}_R(t)}{2}\right]\Gamma_1 \tag{D.12}$$

Thus, we arrive at the remarkable result that the OOP response of the wall, when only the first mode is included in the analysis, can be determined by assuming that both the top and bottom supports experience the same, in-phase, acceleration time history. That time history is equal at each point in time to the average of the top and bottom accelerations. This is somewhat similar to the procedure used by Hashemi and Mosalam (2007), where the average floor-level accelerations were used to calculate the OOP response, although in that case the infill panel was considered rigid in the OOP direction.

The maximum response of the wall may be determined using the response spectrum analysis method, where the maximum value of the modal coordinate $q_1(t)$ is:

$$q_{1\max} = \Gamma_1 S_{d1} \tag{D.13}$$

where S_{d1} is the displacement response spectrum for a single-degree-of-freedom (SDOF) system excited by the average (as mentioned above) support acceleration. The bending moment and the shear force are then calculated from the following relationships based on elementary beam theory (Chopra 2007):

$$M(x,t) = EI\frac{\partial^2 u(x,t)}{\partial x^2} \qquad V(x,t) = EI\frac{\partial^3 u(x,t)}{\partial x^3} \tag{D.14}$$

First, determine the maximum total force exerted on the beam by the surrounding structure. This force, at time t, is equal to $V(0,t) - V(h,t)$, i.e., the sum of the shears at the ends of the beam with proper consideration of signs.

$$V(0,t)-V(h,t)=EI\left[\frac{\partial^3 u(0,t)}{\partial x^3}-\frac{\partial^3 u(h,t)}{\partial x^3}\right]=-EI\int_{x=0}^{h}\frac{\partial^4 u(x,t)}{\partial x^4}dx=-EI\int_{x=0}^{h}\frac{\partial^4 \phi(x)}{\partial x^4}q(t)dx$$
$$=F(t)=-\omega^2\left\{\int_{x=0}^{h}m\phi(x)dx\right\}q(t) \qquad \text{(D.15)}$$

where modal subscripts have been dropped, since only the first mode is considered to contribute to the response, and use has been made of the second equation in (D.3). The maximum absolute value of the sum of the support forces is:

$$F_{\max}=\omega^2\left\{\int_{x=0}^{h}m\phi(x)dx\right\}q_{\max}=\omega^2\left\{\int_{x=0}^{h}m\phi(x)dx\right\}\Gamma S_d=\left\{\int_{x=0}^{h}m\phi(x)dx\right\}\Gamma S_a=MEM\times S_a \qquad \text{(D.16)}$$

where $S_a=\omega^2 S_d$ is the spectral acceleration, and MEM is the modal effective mass, defined as:

$$MEM=\left\{\int_{x=0}^{h}m\phi(x)dx\right\}\Gamma=\frac{\left(\int_{x=0}^{h}m\phi(x)dx\right)^2 dx}{\int_{x=0}^{h}m\phi^2(x)dx} \qquad \text{(D.17)}$$

In other words, the MEM is the mass value that, when multiplied by the spectral acceleration, will give the maximum total support force caused by the base acceleration. For the first-mode shape given in Equation (D.6), Equation (D.17) gives:

$MEM=0.81mh$

That is, the modal effective mass for the first mode is 81% of the total mass of the beam.

Next, the maximum midspan moment is calculated:

$$M\left(\frac{h}{2},t\right)=EI\left.\frac{\partial^2\phi(x)}{\partial x^2}\right|_{x=\frac{h}{2}}q(t) \qquad \text{(D.19)}$$

$$M\left(\frac{h}{2},t\right)\Big|_{\max}=EI\left.\frac{\partial^2\phi(x)}{\partial x^2}\right|_{x=\frac{h}{2}}q_{\max}=EI\left.\frac{\partial^2\phi(x)}{\partial x^2}\right|_{x=\frac{h}{2}}\frac{\Gamma S_a}{\omega^2} \qquad \text{(D.20)}$$

Substituting from the first equation in (D.6) and differentiating (taking $C_1=1$),

$$\left.\frac{\partial^2\phi(x)}{\partial x^2}\right|_{x=\frac{h}{2}}=-\frac{\pi^2}{h^2} \qquad \text{(D.21)}$$

Rearranging the second equation in (D.6), one obtains $\frac{\omega^2 h^4 m}{\pi^4 EI}=1$. Therefore, from this rearrangement and using Equation (D.21), Equation (D.20) becomes:

$$M\left(\frac{h}{2},t\right)\Big|_{\max} = \left[EI\frac{\partial^2\phi(x)}{\partial x^2}\Big|_{x=\frac{h}{2}}\right]\times\frac{\Gamma S_a}{\omega^2} = EI\left(\frac{\pi^2}{h^2}\right)\frac{\Gamma S_a}{\omega^2}\left[\frac{\omega^2 h^4 m}{\pi^4 EI}\right] = \frac{\Gamma S_a h^2 m}{\pi^2} \tag{D.22}$$

Here, the absolute value is taken, particularly in the use of the result from Equation (D.21). For the first mode, with $\Gamma_1 = 1.2732$, the maximum absolute midspan moment is:

$$M\left(\frac{h}{2},t\right)\Big|_{\max} = \frac{(mS_a)h^2}{7.752} \tag{D.23}$$

It is interesting to note that the first-mode midspan moment in Equation (D.23) is nearly equal to the moment that would be found by applying a uniform load of mS_a, for which the denominator would be 8 instead of 7.752, i.e., a ratio of 0.969. As a last step for the original system, calculate the spectral acceleration, S_{ay}, at which the beam reaches incipient yield at midspan, assuming that the expected OOP strength of the infill wall, in terms of a uniform pressure, q_{ine}, is known:

$$M_y = \frac{q_{ine}L_{\inf}h^2}{8} = \frac{(mS_{ay})h^2}{7.752} \tag{D.24}$$

where $L_{\inf}$ is the horizontal length of the infill panel. Rearranging,

$$S_{ay} = 0.969\ \frac{q_{ine}L_{\inf}}{m} \tag{D.25}$$

Next, consider the response of the equivalent system (Fig. D.4). It has one OOP DOF, which is denoted Δ_{OOP}. This is the displacement of the midspan OOP mass. First, assume that the midspan mass is equal to the *MEM* derived above for the original system. Subsequently, calculate the bending stiffness required to produce the same frequency as the original system. Next, show that the base reaction for the equivalent system is equal to the original system. Finally, calculate the yield moment for the equivalent system, such that both the original system and the equivalent system experience incipient yielding at the same spectral acceleration.

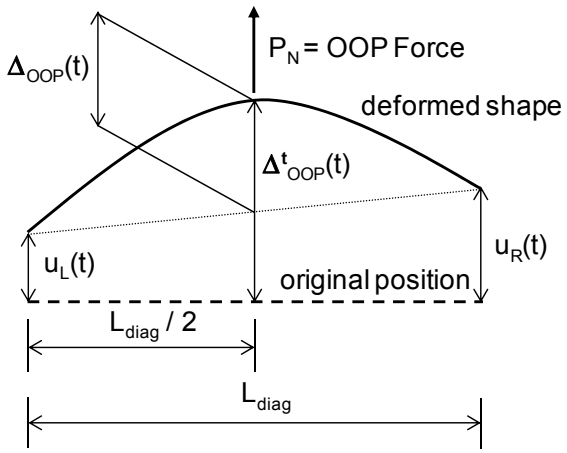

Fig. D.4 First-mode deformation of equivalent system with base excitation.

The OOP stiffness of the equivalent system, k_{eq}, defined as the OOP force, P_N, required to produce a unit deflection, is well known for a simply supported beam from structural analysis as:

$$k_{eq} = \frac{P_N}{\Delta_{OOP}} = \frac{48 E I_{eq}}{L_{diag}^3} \tag{D.26}$$

where I_{eq} is the equivalent moment of inertia of the section, and E is the URM elastic modulus. The circular natural frequency of the equivalent system, assuming a mass at the midspan equal to the first-mode effective mass, MEM, is given by

$$\omega_{eq} = \sqrt{\frac{k_{eq}}{MEM}} \qquad \text{or} \qquad k_{eq} = MEM \times \omega_{eq}^2 \tag{D.27}$$

Equating this frequency to the circular frequency of the original system, second equation in (D.6), and substituting into Equation (D.26) yields:

$$I_{eq} = \frac{MEM\ \omega_{eq}^2 L_{diag}^3}{48E} = \frac{MEM\ \pi^4 E I L_{diag}^3}{48 h^4 m E} = \frac{0.81\pi^4}{48}\left(\frac{L_{diag}}{h}\right)^3 I = 1.644\left(\frac{L_{diag}}{h}\right)^3 I \tag{D.28}$$

where use has been made of Equation (D.18). This provides the moment of inertia of the equivalent system in terms of the moment of inertia of the original infill panel cross section, I, equal to $\left(\kappa L_{\text{inf}} t_{\text{inf}}^{\ 3}\right)/12$, where t_{inf} is the thickness of the infill, and κ is a factor to account for cracking.

From the well-known principles of structural mechanics, the equation of motion for the equivalent system (with OOP mass equal to MEM) is given by

$$MEM\ \ddot{\Delta}_{OOP} + k_{eq}\Delta_{OOP} = -MEM\left[\frac{\ddot{u}_L(t) + \ddot{u}_R(t)}{2}\right] \qquad \text{or}$$

$$\ddot{\Delta}_{OOP} + \omega_{eq}^2 \Delta_{OOP} = -\left[\frac{\ddot{u}_L(t) + \ddot{u}_R(t)}{2}\right] \tag{D.29}$$

The solution for maximum displacement is given by

$$\Delta_{OOP,\max} = S_d \tag{D.30}$$

where S_d is the SDOF response for the average support motion, as defined for the original system. The maximum structural base force is then given by

$$F_{\max} = k_{eq}\Delta_{OOP,\max} = MEM \times \omega_{eq}^2 S_d = MEM \times S_a \tag{D.31}$$

Thus, the base force for the equivalent system is equal to the equivalent force for the original system, as given in Equation (D.16). The maximum midspan moment is given by

$$M_{\max} = \frac{F_{\max} L_{diag}}{4} = MEM \times S_a \times \frac{L_{diag}}{4} \tag{D.32}$$

For equivalence, the yield moment in the equivalent system beam is reached when the support spectral acceleration, S_a, equals the yield spectral acceleration of the original system, S_{ay}, defined by Equation (D.25). Thus:

$$M_{eq\_y} = MEM \times S_{ay} \times \frac{L_{diag}}{4} \tag{D.33}$$

Using Equations (D.18) and (D.24), this can be simplified to the following:

$$M_{eq\_y} = 0.81mh \times \frac{7.752 M_y}{mh^2} \times \frac{L_{diag}}{4} = 1.570 \frac{L_{diag}}{h} M_y \tag{D.34}$$

where M_y is the yield moment in the original system. Finally, calculate the OOP force that causes the equivalent beam to yield, using Equations (D.18), (D.25), and (D.31), one obtains the following:

$$F_{eq\_y} = \frac{4M_{eq\_y}}{L_{diag}} = MEM \times S_{ay} = 0.81mh \times 0.969 \frac{q_{ine} L_{\inf}}{m} = 0.785\left[q_{ine}\, L_{\inf}\, h\right] \tag{D.35}$$

Note that the term in square brackets is the expected static OOP capacity (in terms of total force) of the infill panel, based on FEMA equations (FEMA 2000). The coefficient 0.785 is the product of two factors. One factor, 0.81, is the ratio between the first-mode effective mass and the total wall weight (see Equations (D.17) and (D.18)). It results from the fact that only the first mode is being used in the analysis. The second factor, 0.969, is the ratio between the moment due to a uniformly applied quasi-static load and the moment caused by the first mode (see Equation (D.24)).

The equations derived above are applied in Appendix E to the infill panel case study used in Chapters 3 and 4.

Appendix E: Calculation of Model Parameters

This appendix contains the detailed calculations for the model parameters. Input data are highlighted. Note: references to specific pages in Hashemi and Mosalam (2007) are shown as "(H&M, p. xx)."

Input properties:

$f'_{me} := 2.46\ ksi$ Masonry expected compressive strength (from H&M, p.45).

$t_{inf} := 3.75\ in$ Thickness of infill masonry (H&M, p.133).

$h_{inf} := 101.5\ in$ Height of infill (H&M, p.133).

$L_{inf} := 150\ in$ Length of infill (H&M, p.133).

$h_{col} := 108\ in$ Floor-to-floor height (H&M, p. 133).

$L_{col} := 13.5\ ft$ Centerline distance between columns (H&M, p.10).

$E_m := 550\ f'_{me}$ FEMA 356 formula for masonry elastic modulus (expected and lower bound) (Tables 7-1 and 7-2).

$E_m = 1353.00\ ksi$

For this case, match Hashemi's E_m, in order to match the frequency of his model:

$E_m := 1770\ ksi$ Elastic modulus from H&M, p.179

$E_{fe} := 4250\ ksi$ Expected elastic modulus of frame concrete (H&M, p. 133).

$I_g := \frac{12\,in \cdot (12\,in)^3}{12}$ Gross moment of inertia of the concrete columns (H&M, p.10).

$I_{col} := 0.5 \cdot I_g$ Effective cracked moment of inertia of the concrete columns. (FEMA 356, Table 6-5).

$I_{col} = 864\ in^4$

$r_{inf} := \sqrt{h_{inf}^2 + L_{inf}^2}$ Diagonal length of the infill.

$r_{inf} = 181.114 \text{ in}$

$\theta_{inf} := \text{atan}\left(\frac{h_{inf}}{L_{inf}}\right)$ Angle of the diagonal for the infill.

$\theta_{inf} = 34.085 \text{ deg}$

$L_{diag} := \sqrt{h_{col}^2 + L_{col}^2}$ Diagonal length between column centerlines and floor centerlines.

$L_{diag} = 194.7 \text{ in}$

$\theta_{diag} := \text{atan}\left(\frac{h_{col}}{L_{col}}\right)$ Angle of the diagonal between beam-column workpoints.

$\theta_{diag} = 33.69 \text{ deg}$

$\Gamma := 1.2732$ First OOP mode participation factor (see Appendix D)

Calculate the width of the compression strut which represents the infill, based on the method given in FEMA 356, Section 7.5.2:

$\lambda_1 := \left(\frac{E_m \cdot t_{inf} \cdot \sin(2 \cdot \theta_{inf})}{4 \cdot E_{fe} \cdot I_{col} \cdot h_{inf}}\right)^{\frac{1}{4}}$ $\lambda_1 = 0.045 \text{ in}^{-1}$

$a := 0.175 \cdot (\lambda_1 \cdot h_{col})^{-0.4} \cdot r_{inf}$ Width of the compression strut.

$a = 16.827 \text{ in}$

Calculate the axial stiffness of the infill strut:

$k_{inf} := \frac{a \cdot t_{inf} \cdot E_m}{r_{inf}}$ Axial stiffness for a member which is located on the diagonal between the corners of the infilled area.

$k_{inf} = 616.662 \frac{\text{kip}}{\text{in}}$ Note that this will also be the stiffness of the equivalent beam-column member which will be located between the workpoints, with a length of L_{diag}.

Calculate the axial strength of the infill strut:

(Based on FEMA 356, Section 7.5.2.2)

$P_{ce} := 41.4\ kip$ — Expected gravity compressive force applied to wall panel (from H&M, p.133).

$v_{te} := 90\ psi$ — Average bed joint shear strength (from H&M, p. 133).

$A_n := t_{inf} \cdot L_{inf}$ — Net bedded area of the infill.

$A_n = 562.5\ in^2$

$v_{me} := \frac{0.75 \cdot \left(v_{te} + \frac{P_{ce}}{A_n} \right)}{1.5}$ — Expected masonry shear strength

$v_{me} = 81.8\ psi$

$Q_{ce} := v_{me} \cdot A_n$ — Expected horizontal shear capacity of infill. (Equation 7-15, FEMA 356).

$Q_{ce} = 46.013\ kip$

$P_{n0} := \frac{Q_{ce}}{\cos(\theta_{diag})}$ — Axial capacity of the equivalent compression strut, which will run between workpoints in the concrete frame.

$P_{n0} = 55.3\ kip$

Calculate the "yield point," i.e., the axial deformation in the equivalent strut at the point where the initial tangent stiffness line intersects the element capacity:

$\delta_{Ay0} := \frac{P_{n0}}{k_{inf}}$ (assumes no OOP load)

$\delta_{Ay0} = 0.09\ in$

Calculate the IP horizontal deflection of the panel at the yield point:

$u_{Hy0} := \frac{\delta_{Ay0}}{\cos(\theta_{diag})}$

$u_{Hy0} = 0.108\ in$ — Note: assumes that the vertical deflections of the endpoints are zero

---

Calculate the lateral deflection of the panel at the collapse prevention (CP) limit state:

Based on FEMA 356, Section 7.5.3.2.4, including Table 7-9:

1) Estimate $\beta < 0.7$ Where β is defined as V_{fre} / V_{ine}, the ratio of frame to infill expected strengths

2) $\frac{L_{inf}}{h_{inf}} = 1.478$

3) $d := .35\ \%$ (Interpolated in Table 7-9. It is assumed that the CP limit state is reached when the element drift reaches point "d" as shown in Figure 7-1 of FEMA 356)

$u_{Hcp0} := d \cdot h_{inf}$ Displacement of the panel at the CP limit state

$u_{Hcp0} = 0.355\ in$

$\mu_{H0} := \frac{u_{Hcp0}}{u_{Hy0}}$ Implied ductility at the collapse prevention level.

$\mu_{H0} = 3.296$

Calculate the required area of the equivalent element, which will span between workpoints, and will have an elastic modulus equal to E_m:

$A_{elem} := \frac{k_{inf} \cdot L_{diag}}{E_m}$

$A_{elem} = 67.833\ in^2$

Calculate the Out-of-Plane (OOP) parameters of the infill:

$\gamma_{inf} := 120\ \frac{lbf}{ft^3}$ Weight density of the infill bricks (assumed).

Calculate the OOP frequency of the infill, assuming that it spans vertically, with simply-supported ends:

$I_{inf\_g} := \frac{L_{inf} \cdot t_{inf}^{3}}{12}$ Moment of inertia of the uncracked infill (gross moment)

$I_{inf} := \frac{1}{2} \cdot I_{inf\_g}$ Estimated moment of inertia of the cracked infill

$I_{inf} = 329.59\ in^4$

$w_{inf} := L_{inf} \cdot t_{inf} \cdot \gamma_{inf}$ Weight per unit of length (measured vertically) of the infill.

$w_{inf} = 39.063\ \frac{lbf}{in}$

$f_{ss} := \frac{\pi}{2 \cdot h_{inf}^{2}} \cdot \sqrt{\frac{E_m \cdot I_{inf} \cdot g}{w_{inf}}}$ First natural frequency of the infill, spanning in the vertical direction, with top and bottom ends simply supported. (Blevins 1979, Table 8-1).

$f_{ss} = 11.578\ Hz$

Calculate the OOP effective weight:

The OOP effective weight is based on the modal effective mass of the vertically spanning, simply supported (assumed) infill wall. For simple-simple conditions, the modal effective weight is equal to 81% of the total infill weight. See Appendix D for a derivation of this value.

$W_{inf} := \gamma_{inf} \cdot t_{inf} \cdot h_{inf} \cdot L_{inf}$ Total weight of the infill.

$W_{inf} = 3.965\ kip$

$MEW := 0.81 \cdot W_{inf}$ Modal effective weight, assuming that the wall spans vertically, and is simply supported top and bottom. (First mode). See Appendix D.

$MEW = 3.212\ kip$

Calculate the equivalent OOP spring which will provide the identical frequency.

$k_{eq\_N} := \left(2 \cdot \pi \cdot f_{ss}\right)^{2} \cdot \frac{MEW}{g}$

$k_{eq\_N} = 44.018\ \frac{kip}{in}$

Calculate the moment of inertia of the equivalent beam element, such that it will provide the correct value of k_{eq_N}:

$$I_{eq} := \frac{k_{eq\_N} \cdot \left(L_{diag}^{3} \right)}{48 \cdot E_m}$$

$I_{eq} = 3824.0 \ in^{4.0}$ $\qquad I_{elem} := I_{eq}$

Using Equation D.28 from Appendix D:

$$1.644 \cdot \left(\frac{L_{diag}}{h_{inf}} \right)^{3} \cdot I_{inf} = 3824.5 \ in^{4}$$ (Same results)

Calculate the OOP capacity of the infill:

The OOP capacity is based on FEMA 356, Section 7.5.3.2.

$$\frac{h_{inf}}{t_{inf}} = 27.067$$

Since this value is outside the range used in FEMA 356, Table 7-11, for determining λ, perform an extrapolation:

Array of values from Table 7-11:

$$FEMA\_Array := \begin{pmatrix} 5 & 0.129 \\ 10 & 0.060 \\ 15 & 0.034 \\ 25 & 0.013 \end{pmatrix}$$

$$\lambda_2 := linterp\left(FEMA\_Array\ \langle 1 \rangle, FEMA\_Array\ \langle 2 \rangle, \frac{h_{inf}}{t_{inf}} \right) \qquad \lambda_2 = 0.00866$$

Check by graphing the values:

$$Array := \begin{pmatrix} 5 & 0.129 \\ 10 & 0.060 \\ 15 & 0.034 \\ 25 & 0.013 \\ \frac{h_{inf}}{t_{inf}} & \lambda_2 \end{pmatrix} \qquad k := 1 .. rows(Array)$$

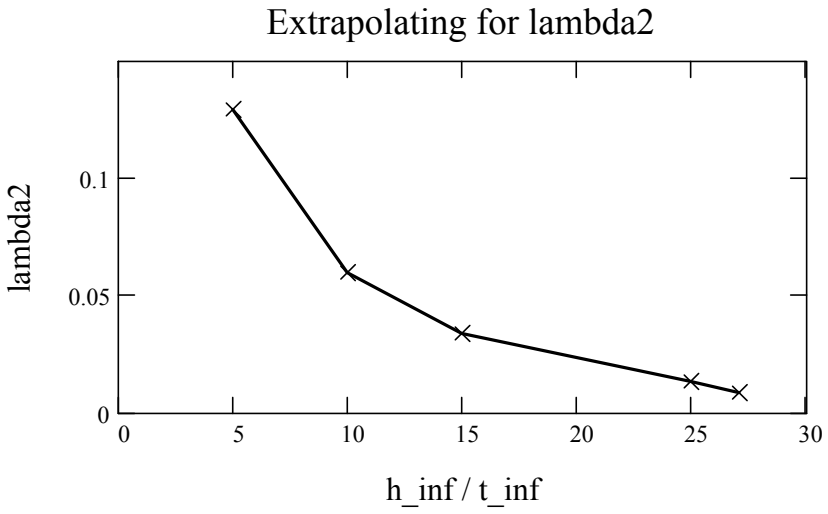

$$q_{in} := \frac{0.7 \cdot f'_{me} \cdot \lambda_2}{\frac{h_{inf}}{t_{inf}}}$$

Note: the expected, rather than the lower bound value, of masonry compressive strength is used here, since the expected OOP strength will be used in later calculations.

$q_{in} = 79.338 \frac{lbf}{ft^2}$ $q_{in} = 0.551$ psi

$q_{in} \cdot h_{inf} \cdot L_{inf} = 8.388$ kip Total OOP force on the wall at capacity.

Calculate the moment in the infill wall at the time that it reaches its capacity:

$$M_y := \frac{q_{in} \cdot L_{inf} \cdot h_{inf}^2}{8}$$

Assumes simple support at the top and bottom.

$M_y = 106.426$ in·kip

Calculate the required yield moment for the equivalent element, such that the same base motion will bring it and the original wall to incipient yield:

$M_{eq\_y} := 1.570 \cdot \frac{L_{diag}}{h_{inf}} \cdot M_y$ Note: for derivation of this equation, see Appendix D.

$M_{eq\_y} = 320.515$ in·kip

$M_{n0} := M_{eq\_y}$ Defines the OOP "yield" moment for the equivalent member when the IP axial force is zero.

Determine the OOP point force, applied at the midspan of the equivalent element, to cause yielding:

$$F_{Ny0} := \frac{4 \cdot M_{eq\_y}}{L_{diag}}$$

$F_{Ny0} = 6.585 \quad kip$

Calculate the displacement of the equivalent element at first yield and at the collapse prevention limit state, assuming no IP axial force:

$$u_{Ny0} := \frac{F_{Ny0}}{k_{eq\_N}}$$ OOP "yield" displacement, assuming no IP axial force.

$u_{Ny0} = 0.15 \quad in$

The displacement at collapse prevention limit state:

FEMA 356, Section 7.5.3.3 gives a maximum OOP deflection based on an OOP story drift ratio of 5%.

$u_{Ncp0} := 0.05 \cdot h_{inf}$

$u_{Ncp0} = 5.075 \quad in$

This value seems too high, since it's larger than the thickness of the infill itself. Instead, define the CP displacement as equal to one half the thickness of the infill.

$$u_{Ncp0} := \min\left(0.05 \cdot h_{inf}, \frac{t_{inf}}{2}\right)$$

$u_{Ncp0} = 1.875 \quad in$

The implied ductility ratio is:

$$\mu_{Ncp0} := \frac{u_{Ncp0}}{u_{Ny0}}$$ $\mu_{Ncp0} = 12.534$

This ductility seems too high. Based on judgment, use a (conservative) ductility of 5:

$\mu_{Ncp0} := 5$ $u_{Ncp0} := u_{Ny0} \cdot \mu_{Ncp0}$ $u_{Ncp0} = 0.748 \quad in$

Calculating the axial force–moment interaction curve for specific values of P_{n0} and M_{n0}:

Using the exponent relationship:

$$f\_P_n(M_n, P_{n0}, M_{n0}) := P_{n0}\cdot\left[1-\left(\frac{M_n}{M_{n0}}\right)^{\frac{3}{2}}\right]^{\frac{2}{3}}$$

This is the target P-M relationship for the equivalent member, located on the diagonal between structural workpoints.

$P_{n0} = 55.3 \text{ kip}$ Axial capacity of the member under pure compression (calculated above).

$M_{n0} = 320.515 \text{ in·kip}$ Moment capacity of the member under pure bending (calculated above).

$N_{interaction} := 6$ Number of points on the interaction curve to be used for calculating fiber properties (should be an even number).

$N_{fiber} := 2\cdot(N_{interaction} - 1)$ $N_{fiber} = 10$

$M_n :=$ for $q \in 1 .. N_{interaction}$

$M_{n_q} \leftarrow (q-1)\cdot\frac{M_{n0}}{N_{interaction}-1}$

M_n

$P_n :=$ for $q \in 1 .. N_{interaction}$

$P_{n_q} \leftarrow f\_P_n(M_{n_q}, P_{n0}, M_{n0})$

P_n

$M_n^T = (0.0 \quad 64.1 \quad 128.2 \quad 192.3 \quad 256.4 \quad 320.5) \text{ in·kip}$ $P_n^T = (55.3 \quad 52.0 \quad 45.5 \quad 36.5 \quad 23.9 \quad 0.0) \text{ kip}$

$q := 1 .. N_{interaction}$

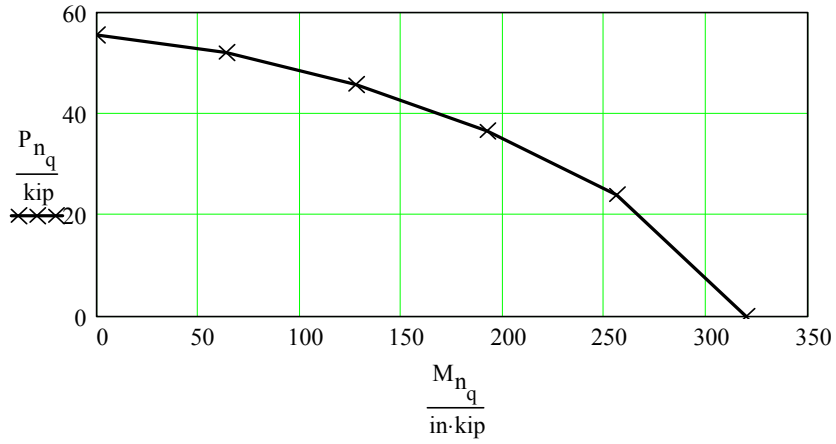

Calculate the required strength and location of the various fibers:

$$F_y := \left| \begin{array}{l} \text{for } p \in 1 .. N_{interaction} - 1 \\ \quad F_{y_p} \leftarrow \dfrac{P_{n_p} - P_{n_{p+1}}}{2} \\ \text{for } p \in N_{interaction} .. 2 \cdot (N_{interaction} - 1) \\ \quad F_{y_p} \leftarrow F_{y_{2 \cdot N_{interaction} - 1 - p}} \\ F_y \end{array} \right.$$

$F_y =$ kip

	1
1	1.674
2	3.212
3	4.536
4	6.268
5	11.959
6	11.959
7	6.268
8	4.536
9	3.212
10	1.674

$$\sum_{p=1}^{N_{fiber}} F_{y_p} = 55.3 \text{ kip}$$

$$z := \left| \begin{array}{l} \text{for } p \in 1 .. N_{interaction} - 1 \\ \quad z_p \leftarrow \dfrac{M_{n_{p+1}} - M_{n_p}}{2 \cdot F_{y_p}} \\ \text{for } p \in N_{interaction} .. 2 \cdot (N_{interaction} - 1) \\ \quad z_p \leftarrow -\left(z_{2 \cdot N_{interaction} - 1 - p}\right) \\ z \end{array} \right.$$

$z =$ in

	1
1	19.143
2	9.98
3	7.065
4	5.113
5	2.68
6	-2.68
7	-5.113
8	-7.065
9	-9.98
10	-19.143

$abs(x) := if(x \geq 0.0, x, -x)$ Absolute function (since the MathCad absolute function has some bugs).

Solve block for the determining the values of the parameters γ and η:

Estimate the values of the parameters: $\gamma := 30$ $\eta := -.2$

Given

$$\sum_{p=1}^{N_{fiber}} \left[\gamma \cdot \left(abs\left(\frac{z_p}{in} \right)^{\eta} \right) \right] = \frac{A_{elem}}{in^2} \qquad \sum_{p=1}^{N_{fiber}} \left[\left(\gamma \cdot abs\left(\frac{z_p}{in} \right)^{\eta} \right) \cdot \left(\frac{z_p}{in} \right)^2 \right] = \frac{I_{elem}}{in^4}$$

$\text{Result} := \text{Find}(\gamma, \eta)$

$\gamma := \text{Result}_1 \cdot \text{in}^2 \qquad \gamma = 32.273 \ \text{in}^2$

$\eta := \text{Result}_2 \qquad \eta = -0.875$

$$A := \left| \begin{array}{l} \text{for } p \in 1 .. N_{fiber} \\ \quad A_p \leftarrow \gamma \cdot \text{abs}\left(\frac{z_p}{\text{in}}\right)^{\eta} \\ A \end{array} \right.$$

$A^T =$

	1	2	3	4	5	6	7
1	2.435	4.306	5.827	7.734	13.615	13.615	7.734

in^2

Check the results above:

$\sum_{p=1}^{N_{fiber}} A_p = 67.833 \ \text{in}^2 \qquad \sum_{p=1}^{N_{fiber}} \left[A_p \cdot (z_p)^2\right] = 3823.978 \ \text{in}^4$

Determine the stress at yield:

$$\sigma_y := \left| \begin{array}{l} \text{for } p \in 1 .. N_{fiber} \\ \quad \sigma_p \leftarrow \frac{F_{y_p}}{A_p} \\ \sigma \end{array} \right.$$

$\sigma_y^T =$

	1	2	3	4	5
1	0.688	0.746	0.779	0.811	0.878

ksi

Yield stress for Elements 6-10 are symmetric

Calculate the strain at first yield:

$$\varepsilon_y := \left| \begin{array}{l} \text{for } p \in 1 .. N_{fiber} \\ \quad \varepsilon_{y_p} \leftarrow \frac{\sigma_{y_p}}{E_m} \\ \varepsilon_y \end{array} \right.$$

Summary of Fiber Properties:

Elastic Modulus: $E_m = 1770$ ksi

Fiber yield strength:

$F_y =$

	1
1	1.674
2	3.212
3	4.536
4	6.268
5	11.959
6	11.959
7	6.268
8	4.536
9	3.212
10	1.674

kip

Fiber Area:

$A =$

	1
1	2.435
2	4.306
3	5.827
4	7.734
5	13.615
6	13.615
7	7.734
8	5.827
9	4.306
10	2.435

$in^{2.000}$

Fiber location (distance from CL):

$z =$

	1
1	19.143
2	9.98
3	7.065
4	5.113
5	2.68
6	-2.68
7	-5.113
8	-7.065
9	-9.98
10	-19.143

in

Fiber yield stress:

$\sigma_y =$

	1
1	0.688
2	0.746
3	0.779
4	0.811
5	0.878
6	0.878
7	0.811
8	0.779
9	0.746
10	0.688

ksi

Fiber yield strain:

$\varepsilon_y =$

	1
1	0.000389
2	0.000421
3	0.000440
4	0.000458
5	0.000496
6	0.000496
7	0.000458
8	0.000440
9	0.000421
10	0.000389

Verify that the given parameters will produce the desired section properties:

$$A_{calc} := \sum_{p=1}^{N_{fiber}} A_p \qquad A_{calc} = 67.833\ in^2 \qquad \frac{A_{calc}}{A_{elem}} = 1.000$$

$$I_{calc} := \sum_{p=1}^{N_{fiber}} \left[A_p \cdot (z_p)^2\right] \qquad I_{calc} = 3823.9775\ in^4 \qquad \frac{I_{calc}}{I_{eq}} = 1.000$$

$$P_{0\_calc} := \sum_{p=1}^{N_{fiber}} \left(A_p \cdot \sigma_{y_p}\right) \qquad P_{0\_calc} = 55.3\ kip \qquad \frac{P_{0\_calc}}{P_{n0}} = 1.000$$

$$M_{0\_calc} := \sum_{p=1}^{N_{fiber}} \left(\sigma_{y_p} \cdot A_p \cdot abs(z_p)\right) \qquad M_{0\_calc} = 320.515\ in \cdot kip \qquad \frac{M_{0\_calc}}{M_{n0}} = 1.000$$

Appendix F: Monte Carlo Simulations

The purpose of this appendix is to provide examples of the Monte Carlo simulation (MCS) analyses used to re-calculate the fragility functions for the five-story model used by Hashemi and Mosalam (2007). In that model the infill panels were represented by compression-only struts, which were composed of linear elastic materials.

The Hashemi and Mosalam (2007) model was based on an infill OOP strength of 155 psf, as given in Appendix D of that reference. For this report, an OOP strength of 79 psf is judged to be more appropriate (see Appendix E). The ratio is 79 / 155 = 0.51. In addition, the IP strength of the Hashemi and Mosalam (2007) model was 69.4 kips, while for this report it is taken as (see Chapter 3) 46.0 kips, based on a factor of 1/1.5.

It is desired to compare the fragility functions generated by the Hashemi and Mosalam (2007) model with the functions generated by this report. In order to make a valid comparison, it is necessary to compare functions calculated on an equivalent basis, i.e., for the same IP and OOP force-based capacities. Hashemi and Mosalam (2007) used a reliability analysis to calculate fragilities. For this report, it is decided to use MCS.

First, in order to confirm the MCS validity, the fragilities are re-calculated, using MathCAD (MathSoft 1997), with the original IP and OOP capacities. This analysis begins on the next page. The analysis shown is for the first-story infill panel, with the spectral acceleration, *Sa* = 1.61g (5/50). The resulting probabilities of exceedence are the same as those given by Hashemi and Mosalam (2007), thus confirming the validity of MCS. Next, the MCS is applied to the same case, except that the OOP capacity is factored by 0.51 and the IP capacity is factored by 1/1.5. These results, along with the results from the other four *Sa* levels, are reported in Section 4.3.

Worksheet for calculating points on the fragility curve:

This worksheet uses a MCS to calculate the probability of failure of a wall due to in-plane loads, out-of-plane loads, and a combination of the two effects. The first analysis uses the original strength values from Hashemi and Mosalam (2007).

Case: First story, Sa = 1.61g

$N := 200000$ Number of Monte Carlo Trials

Statistics for the in-plane and out-of-plane strengths:

$\mu_{RH} := 309$ Mean in-plane strength (kN)

$\sigma_{RH} := 71.2$ Standard deviation of in-plane strength (kN)

$\mu_{RN} := 36.4$ Mean out-of-plane strength (kN)

$\sigma_{RN} := 8.40$ Standard deviation of out-of-plane strength (kN)

$\rho_{HN} := .30$ Correlation coefficient between in-plane and out-of-plane strengths

Notes:

(1) The probability equations used in this appendix are taken from Garvey (1993).

(2) The original demand and capacity parameters are from Hashemi and Mosalam (2007).

Statistics for the in-plane and out-of-plane loads:

$\mu_{PH} := 558$ Mean in-plane loads (kN)

$\sigma_{PH} := 234$ Standard deviation of in-plane loads (kN)

$\mu_{PN} := 3.03$ Mean out-of-plane loads (kN)

$\sigma_{PN} := 1.40$ Standard deviation of out-of-plane loads (kN)

$\rho_{PH\_PN} := -0.11$ Correlation coefficient between in-plane and out-of-plane loads

Sets of lognormally distributed loads and capacities are created using the MathCad random number generator. First, the statistics given above, which are given in the linear domain, must be converted to log-domain statistics:

For the **capacities**:

$$\beta_{RH} := \sqrt{\ln\left(\frac{\sigma_{RH}^2}{\mu_{RH}^2} + 1\right)} \qquad \beta_{RH} = 0.227$$ Standard deviation of the LNs

$$\alpha_{RH} := \ln\left(\frac{\mu_{RH}}{\sqrt{\frac{\sigma_{RH}^2}{\mu_{RH}^2} + 1}}\right) \qquad \alpha_{RH} = 5.707$$ Mean of the LNs

$$Med_{RH} := e^{\alpha_{RH}} \qquad Med_{RH} = 301.11$$

$$\beta_{RN} := \sqrt{\ln\left(\frac{\sigma_{RN}^2}{\mu_{RN}^2} + 1\right)} \qquad \beta_{RN} = 0.228$$ Standard deviation of the LNs

$$\alpha_{RN} := \ln\left(\frac{\mu_{RN}}{\sqrt{\frac{\sigma_{RN}^2}{\mu_{RN}^2} + 1}}\right) \qquad \alpha_{RN} = 3.569$$ Mean of the LNs

$$Med_{RN} := e^{\alpha_{RN}} \qquad Med_{RN} = 35.468$$

$f_{RN}(RN) := dlnorm(RN, \alpha_{RN}, \beta_{RN})$ MathCad lognormal function. Confirm by plotting.

$RN_{plot} := 0.0, 0.02 .. 1000$ Plot the out-of-plane strengths:

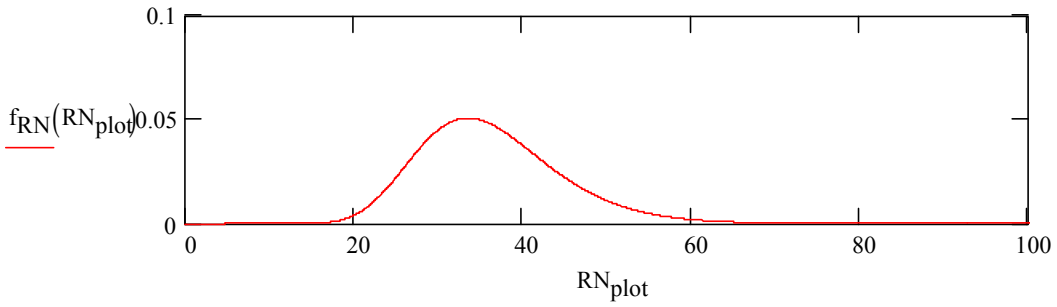

The properties may be checked as follows:

$$\int_0^{10000} f_{RN}(RN)\,dRN = 1.00000 \qquad \frac{1}{\mu_{RN}}\cdot\int_0^{10000} RN\cdot f_{RN}(RN)\,dRN = 1.000$$

$$f_{RH}(RH) := dlnorm\left(RH, \alpha_{RH}, \beta_{RH}\right) \qquad \frac{1}{\sigma_{RN}^{\,2}}\cdot\int_0^{10000} \left(RN - \mu_{RN}\right)^2\cdot f_{RN}(RN)\,dRN = 1.000$$

Create the joint probability distribution:

First, calculate the correlation coefficient for the log domain:

$$\rho_{12} := \frac{1}{\beta_{RH}\cdot\beta_{RN}}\cdot ln\left[1 + \rho_{HN}\cdot\left(\sqrt{e^{\beta_{RH}^{\,2}} - 1}\right)\cdot\left(\sqrt{e^{\beta_{RN}^{\,2}} - 1}\right)\right] \qquad \rho_{12} = 0.305$$

$$w(RH, RN) := \frac{1}{1 - \rho_{12}^{\,2}}\cdot\left[\left(\frac{\ln(RH) - \alpha_{RH}}{\beta_{RH}}\right)^2 \ldots + -2\cdot\rho_{12}\cdot\left(\frac{\ln(RH) - \alpha_{RH}}{\beta_{RH}}\right)\cdot\left(\frac{\ln(RN) - \alpha_{RN}}{\beta_{RN}}\right) \ldots + \left(\frac{\ln(RN) - \alpha_{RN}}{\beta_{RN}}\right)^2\right]$$

Create the joint lognormal distribution for the strengths:

$$f_{RH\_RN}(RH, RN) := \frac{1}{(2\cdot\pi)\cdot\beta_{RH}\cdot\beta_{RN}\cdot\sqrt{1 - \rho_{12}^{\,2}}\cdot RH\cdot RN}\cdot e^{\frac{-1}{2}\cdot w(RH, RN)}$$

Creating sets of random strength values:

First, create lognormally random values of the in-plane strength:

$RH := rlnorm\left(N, \alpha_{RH}, \beta_{RH}\right)$ MathCad function for producing random values of RH

Generate the properly correlated random values for RN (out-of-plane strength):

$$RN := \left| \begin{array}{l} \text{for } i \in 1..N \\ \quad \left| \begin{array}{l} b \leftarrow \alpha_{RN} + \dfrac{\beta_{RN}}{\beta_{RH}} \cdot \rho_{12} \cdot \left(\ln(RH_i) - \alpha_{RH} \right) \\ RN_i \leftarrow \text{rlnorm}\left(1, b, \beta_{RN} \cdot \sqrt{1 - \rho_{12}^{\,2}} \right)_1 \end{array} \right. \\ RN \end{array} \right.$$

(This uses the conditional lognormal distribution for RN, based on the value of RH and the correlation coefficient)

Create the random number pairs for the **loads**, using the same procedure:

$$\beta_{PH} := \sqrt{\ln\left(\frac{\sigma_{PH}^{\,2}}{\mu_{PH}^{\,2}} + 1 \right)} \qquad \beta_{PH} = 0.402$$

Standard deviation of the LNs

$$\alpha_{PH} := \ln\left(\frac{\mu_{PH}}{\sqrt{\dfrac{\sigma_{PH}^{\,2}}{\mu_{PH}^{\,2}} + 1}} \right) \qquad \alpha_{PH} = 6.243$$

Mean of the LNs

$$\text{Med}_{PH} := e^{\alpha_{PH}} \qquad \text{Med}_{PH} = 514.584$$

$$\beta_{PN} := \sqrt{\ln\left(\frac{\sigma_{PN}^{\,2}}{\mu_{PN}^{\,2}} + 1 \right)} \qquad \beta_{PN} = 0.44$$

$$\alpha_{PN} := \ln\left(\frac{\mu_{PN}}{\sqrt{\dfrac{\sigma_{PN}^{\,2}}{\mu_{PN}^{\,2}} + 1}} \right) \qquad \alpha_{PN} = 1.012$$

$$\text{Med}_{PN} := e^{\alpha_{PN}} \qquad \text{Med}_{PN} = 2.751$$

$$f_{PN}(PN) := \text{dlnorm}\left(PN, \alpha_{PN}, \beta_{PN} \right)$$

Create the joint probability distribution:

$$\rho_{12} := \frac{1}{\beta_{PH} \cdot \beta_{PN}} \cdot \ln\left[1 + \rho_{PH\_PN} \cdot \left(\sqrt{e^{\beta_{PH}^{2}} - 1}\right) \cdot \left(\sqrt{e^{\beta_{PN}^{2}} - 1}\right)\right] \qquad \rho_{12} = -0.122$$

$$w(PH, PN) := \frac{1}{1 - \rho_{12}^{2}} \cdot \left[\begin{array}{l} \left(\frac{\ln(PH) - \alpha_{PH}}{\beta_{PH}}\right)^{2} \ldots \\ + -2 \cdot \rho_{12} \cdot \left(\frac{\ln(PH) - \alpha_{PH}}{\beta_{PH}}\right) \cdot \left(\frac{\ln(PN) - \alpha_{PN}}{\beta_{PN}}\right) \ldots \\ + \left(\frac{\ln(PN) - \alpha_{PN}}{\beta_{PN}}\right)^{2} \end{array}\right]$$

$$f_{PH\_PN}(PH, PN) := \frac{1}{(2 \cdot \pi) \cdot \beta_{PH} \cdot \beta_{PN} \cdot \sqrt{1 - \rho_{12}^{2}} \cdot PH \cdot PN} \cdot e^{\frac{-1}{2} \cdot w(PH, PN)}$$

$$PH := \text{rlnorm}\left(N, \alpha_{PH}, \beta_{PH}\right)$$

$$PH_{ave} := \frac{1}{N} \cdot \left(\sum_{i=1}^{N} PH_i\right) \qquad PH_{ave} = 557.967$$

$$PH_{sigma} := \sqrt{\frac{1}{N} \cdot \sum_{i=1}^{N} \left(PH_i - PH_{ave}\right)^{2}} \qquad PH_{sigma} = 233.808$$

Generate the properly correlated random values for PN:

$$PN := \left|\begin{array}{l} \text{for } i \in 1 .. N \\ \quad \left|\begin{array}{l} b \leftarrow \alpha_{PN} + \frac{\beta_{PN}}{\beta_{PH}} \cdot \rho_{12} \cdot \left(\ln\left(PH_i\right) - \alpha_{PH}\right) \\ PN_i \leftarrow \text{rlnorm}\left(1, b, \beta_{PN} \cdot \sqrt{1 - \rho_{12}^{2}}\right)_1 \end{array}\right. \\ PN \end{array}\right.$$

$$PN_{ave} := \frac{1}{N} \cdot \sum_{i=1}^{N} PN_i \qquad PN_{ave} = 3.029$$

$$PN_{sigma} := \sqrt{\frac{1}{N} \cdot \sum_{i=1}^{N} \left(PN_i - PN_{ave}\right)^2} \qquad PN_{sigma} = 1.396$$

$$Corr_{PH\_PN} := \frac{1}{N} \cdot \sum_{i=1}^{N} \left[\frac{\left(PH_i - PH_{ave}\right) \cdot \left(PN_i - PN_{ave}\right)}{PH_{sigma} \cdot PN_{sigma}} \right] \qquad Corr_{PH\_PN} = -0.109848$$

Check the g1 (IP) criterion:

Note: See Hashemi and Mosalam (2007) for a complete discussion of the g1, g2, and g3 criteria.

$$Prob\_Fail\_g1 := \left| \begin{array}{l} failcount \leftarrow 0 \\ \text{for } i \in 1 .. N \\ \quad failcount \leftarrow failcount + 1 \text{ if } \frac{PH_i}{RH_i} > 1.00 \\ \frac{failcount}{N} \end{array} \right. \qquad Prob\_Fail\_g1 = 87.713\%$$

(Corresponding probability from Hashemi and Mosalam (2007): 87.70%)

Check the g2 (OOP) criterion:

$$Prob\_Fail\_g2 := \left| \begin{array}{l} failcount \leftarrow 0 \\ \text{for } i \in 1 .. N \\ \quad failcount \leftarrow failcount + 1 \text{ if } \frac{PN_i}{RN_i} > 1.00 \\ \frac{failcount}{N} \end{array} \right. \qquad Prob\_Fail\_g2 = 0.000000\%$$

(Corresponding probability from Hashemi and Mosalam (2007): 0.0000128%)

Check the g3 criterion:

$\theta_1 := -0.114$ Given values of the g3 interaction function (Hashemi and Mosalam (2007), p.191)

$\theta_2 := .948$ $\theta_3 := -6.18$ $\theta_4 := 111$ $\theta_5 := 11.2$

g3 interaction function:

$$g_3(PH, RH, PN, RN) := \left[\theta_1 \cdot \left(\theta_5 \cdot \frac{PN}{RN}\right)^3 + \theta_2 \cdot \left(\theta_5 \cdot \frac{PN}{RN}\right)^2 + \theta_3 \cdot \left(\theta_5 \cdot \frac{PN}{RN}\right) + \theta_4\right] \cdot \frac{RH}{\theta_4} - PH$$

$$\text{Prob\_Fail\_g3} := \left| \begin{array}{l} \text{failcount} \leftarrow 0 \\ \text{for } i \in 1 .. N \\ \quad \text{failcount} \leftarrow \text{failcount} + 1 \text{ if } g_3\left(PH_i, RH_i, PN_i, RN_i\right) < 0.0 \\ \frac{\text{failcount}}{N} \end{array} \right.$$

Prob_Fail_g3 = 89.70250%

Note: This compares well with the probability given in Hashemi and Mosalam (2007) of 89.30%. Thus, the methodology is confirmed.

Next, calculate the corresponding probabilities for the capacities used in this report:

Calculating Points on the Fragility Curve:

This worksheet uses a MCS to calculate the probability of failure of a wall due to in-plane loads, out-of-plane loads, and a combination of the two effects. The first analysis uses the original strength values from Hashemi and Mosalam (2007).

Case: First story, Sa = 1.61g

$N := 200000$ Number of Monte Carlo Trials

Statistics for the in-plane and out-of-plane strengths:

$\mu_{RH} := 309 \cdot (0.5097)$ Mean in-plane strength (kN)

$\sigma_{RH} := 71.2$ Standard deviation of in-plane strength (kN)

$\mu_{RN} := 36.48\left(\frac{1}{1.5}\right)$ Mean out-of-plane strength (kN)

$\sigma_{RN} := 8.40$ Standard deviation of out-of-plane strength (kN)

$\rho_{HN} := .30$ Correlation coefficient between IP and OOP strengths

Statistics for the in-plane and out-of-plane loads:

$\mu_{PH} := 558$ Mean in-plane loads (kN)

$\sigma_{PH} := 234$ Standard deviation of in-plane loads (kN)

$\mu_{PN} := 3.03$ Mean out-of-plane loads (kN)

$\sigma_{PN} := 1.40$ Standard deviation of out-of-plane loads (kN)

$\rho_{PH\_PN} := -0.11$ Correlation coefficient between in-plane and out-of-plane loads

Sets of lognormally distributed loads and capacities are created using the MathCad random number generator. First, the statistics given above, which are given in the linear domain, must be converted to log-domain statistics:

For the **capacities**:

$$\beta_{RH} := \sqrt{\ln\left(\frac{\sigma_{RH}^2}{\mu_{RH}^2} + 1\right)} \qquad \beta_{RH} = 0.431 \qquad \text{Standard deviation of the LNs}$$

$$\alpha_{RH} := \ln\left(\frac{\mu_{RH}}{\sqrt{\frac{\sigma_{RH}^2}{\mu_{RH}^2} + 1}}\right) \qquad \alpha_{RH} = 4.966 \qquad \text{Mean of the LNs}$$

$$\text{Med}_{RH} := e^{\alpha_{RH}} \qquad \text{Med}_{RH} = 143.514$$

$$\beta_{RN} := \sqrt{\ln\left(\frac{\sigma_{RN}^2}{\mu_{RN}^2} + 1\right)} \qquad \beta_{RN} = 0.336 \qquad \text{Standard deviation of the LNs}$$

$$\alpha_{RN} := \ln\left(\frac{\mu_{RN}}{\sqrt{\frac{\sigma_{RN}^2}{\mu_{RN}^2} + 1}}\right) \qquad \alpha_{RN} = 3.135 \qquad \text{Mean of the LNs}$$

$$\text{Med}_{RN} := e^{\alpha_{RN}} \qquad \text{Med}_{RN} = 22.987$$

$f_{RN}(RN) := \text{dlnorm}(RN, \alpha_{RN}, \beta_{RN})$ MathCad lognormal function. Confirm by plotting.

$RN_{plot} := 0.0, 0.02 .. 1000$ Plot the out-of-plane strengths:

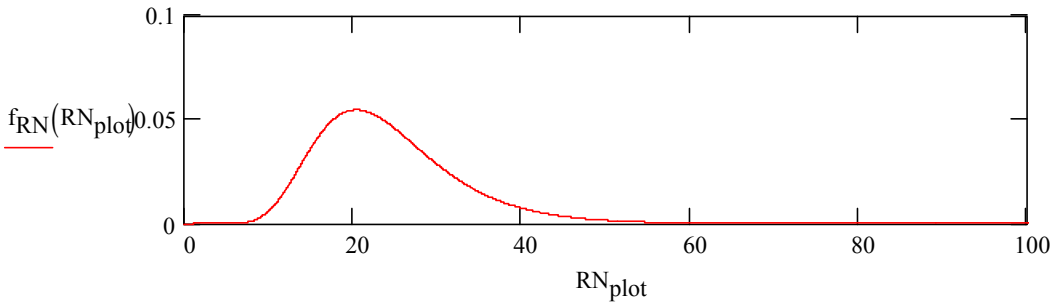

Create the joint probability distribution:

First, calculate the correlation coefficient for the log domain:

$$\rho_{12} := \frac{1}{\beta_{RH}\cdot\beta_{RN}}\cdot\ln\left[1+\rho_{HN}\cdot\left(\sqrt{e^{\beta_{RH}^{2}}-1}\right)\cdot\left(\sqrt{e^{\beta_{RN}^{2}}-1}\right)\right] \qquad \rho_{12} = 0.316$$

$$w(RH,RN) := \frac{1}{1-\rho_{12}^{2}}\cdot\left[\left(\frac{\ln(RH)-\alpha_{RH}}{\beta_{RH}}\right)^{2} \ldots + -2\cdot\rho_{12}\cdot\left(\frac{\ln(RH)-\alpha_{RH}}{\beta_{RH}}\right)\cdot\left(\frac{\ln(RN)-\alpha_{RN}}{\beta_{RN}}\right) \ldots + \left(\frac{\ln(RN)-\alpha_{RN}}{\beta_{RN}}\right)^{2}\right]$$

Create the joint lognormal distribution for the strengths:

$$f_{RH\_RN}(RH,RN) := \frac{1}{(2\cdot\pi)\cdot\beta_{RH}\cdot\beta_{RN}\cdot\sqrt{1-\rho_{12}^{2}}\cdot RH\cdot RN}\cdot e^{\frac{-1}{2}\cdot w(RH,RN)}$$

Creating sets of random strength values:

First, create lognormally random values of the in-plane strength:

$RH := rlnorm(N, \alpha_{RH}, \beta_{RH})$ MathCad function for producing random values of RH

Generate the properly correlated random values for RN (out-of-plane strength):

$RN :=$ for $i \in 1..N$

$b \leftarrow \alpha_{RN} + \frac{\beta_{RN}}{\beta_{RH}}\cdot\rho_{12}\cdot\left(\ln(RH_i)-\alpha_{RH}\right)$

$RN_i \leftarrow rlnorm\left(1, b, \beta_{RN}\cdot\sqrt{1-\rho_{12}^{2}}\right)_1$

RN

(This uses the conditional lognormal distribution for RN, based on the value of RH and the correlation coefficient)

Create the random number pairs for the **loads**, using the same procedure:

Note: Details of load generation are not repeated here, since they are identical to those shown earlier in this appendix.

$$PH := rlnorm\left(N, \alpha_{PH}, \beta_{PH}\right)$$

$$PH_{ave} := \frac{1}{N} \cdot \left(\sum_{i=1}^{N} PH_i \right) \qquad PH_{ave} = 558.817$$

$$PH_{sigma} := \sqrt{\frac{1}{N} \cdot \sum_{i=1}^{N} \left(PH_i - PH_{ave}\right)^2} \qquad PH_{sigma} = 234.34$$

Generate the properly correlated random values for PN:

$$PN := \left| \begin{array}{l} \text{for } i \in 1 .. N \\ \quad \left| \begin{array}{l} b \leftarrow \alpha_{PN} + \dfrac{\beta_{PN}}{\beta_{PH}} \cdot \rho_{12} \cdot \left(\ln\left(PH_i\right) - \alpha_{PH} \right) \\ PN_i \leftarrow rlnorm\left(1, b, \beta_{PN} \cdot \sqrt{1 - \rho_{12}^{\,2}}\right)_1 \end{array} \right. \\ PN \end{array} \right.$$

$$PN_{ave} := \frac{1}{N} \cdot \sum_{i=1}^{N} PN_i \qquad PN_{ave} = 3.032$$

$$PN_{sigma} := \sqrt{\frac{1}{N} \cdot \sum_{i=1}^{N} \left(PN_i - PN_{ave}\right)^2} \qquad PN_{sigma} = 1.408$$

$$Corr_{PH\_PN} := \frac{1}{N} \cdot \sum_{i=1}^{N} \left[\frac{\left(PH_i - PH_{ave}\right) \cdot \left(PN_i - PN_{ave}\right)}{PH_{sigma} \cdot PN_{sigma}} \right] \qquad Corr_{PH\_PN} = 0.294122$$

Check the g1 (IP) criterion: Note: See Hashemi and Mosalam (2007) for a complete discussion of the g1, g2, and g3 criteria.

$$\text{Prob\_Fail\_g1} := \left| \begin{array}{l} \text{failcount} \leftarrow 0 \\ \text{for } i \in 1..N \\ \quad \text{failcount} \leftarrow \text{failcount} + 1 \text{ if } \frac{PH_i}{RH_i} > 1.00 \\ \frac{\text{failcount}}{N} \end{array} \right. \qquad \text{Prob\_Fail\_g1} = 98.492\%$$

Check the g2 (OOP) criterion:

$$\text{Prob\_Fail\_g2} := \left| \begin{array}{l} \text{failcount} \leftarrow 0 \\ \text{for } i \in 1..N \\ \quad \text{failcount} \leftarrow \text{failcount} + 1 \text{ if } \frac{PN_i}{RN_i} > 1.00 \\ \frac{\text{failcount}}{N} \end{array} \right. \qquad \text{Prob\_Fail\_g2} = 5.500 \times 10^{-3}\%$$

Check the g3 criterion:

$\theta_1 := -0.114$ Given values of the g3 interaction function (Hashemi and Mosalam (2007), p. 191)

$\theta_2 := .948$ $\theta_3 := -6.18$ $\theta_4 := 111$ $\theta_5 := 11.2$

g3 interaction function:

$$g_3(PH, RH, PN, RN) := \left[\theta_1 \cdot \left(\theta_5 \cdot \frac{PN}{RN} \right)^3 + \theta_2 \cdot \left(\theta_5 \cdot \frac{PN}{RN} \right)^2 + \theta_3 \cdot \left(\theta_5 \cdot \frac{PN}{RN} \right) + \theta_4 \right] \cdot \frac{RH}{\theta_4} - PH$$

$$\text{Prob\_Fail\_g3} := \left| \begin{array}{l} \text{failcount} \leftarrow 0 \\ \text{for } i \in 1..N \\ \quad \text{failcount} \leftarrow \text{failcount} + 1 \text{ if } g_3(PH_i, RH_i, PN_i, RN_i) < 0.0 \\ \frac{\text{failcount}}{N} \end{array} \right.$$

$\text{Prob\_Fail\_g3} = 98.77150\%$ This value is used in Section 4.3 of this report.

Appendix G: Calculation of Model Parameters-FOSM Analysis (+0.05σ Strength)

This appendix presents the results of the calculations for the model parameters, following the procedure used in Appendix E. For this case the strength (but not stiffness) terms are increased by a factor, Δ_{fac}, in order to use the FOSM method to evaluate the effect of strength variability on the infill fragility. See Section 4.4, for a detailed description of the FOSM method.

Note: Data and calculations that are identical to those in Appendix E are omitted here, and only the significant results are presented below. See Appendix E for details of the calculation methodology.

$\Delta_{fac} = 1.01155$

$P_{n0} = 55.939 \ kip$

$u_{Hy0} = 0.109 \ in$

$u_{Hcp0} = 0.355 \ in$

$\mu_{H0} = 3.258$

$M_y = 107.656 \ in \cdot kip$

$M_{n0} = 324.217 \ in \cdot kip$

$F_{Ny0} = 6.661 \ kip$

$u_{Ny0} = 0.151 \ in$

$u_{Ncp0} = 0.757 \ in$

$\gamma = 32.273 \ in^2$

$\eta = -0.875$

A summary of the fiber properties is given on the next page.

Summary of Fiber Properties:

Elastic Modulus: $E_m = 1770$ ksi

Fiber yield strength:

$F_y =$

	1
1	1.694
2	3.249
3	4.589
4	6.341
5	12.098
6	12.098
7	6.341
8	4.589
9	3.249
10	1.694

kip

Fiber Area:

$A =$

	1
1	2.435
2	4.306
3	5.827
4	7.734
5	13.615
6	13.615
7	7.734
8	5.827
9	4.306
10	2.435

$in^{2.000}$

Fiber location (distance from CL):

$z =$

	1
1	19.143
2	9.98
3	7.065
4	5.113
5	2.68
6	-2.68
7	-5.113
8	-7.065
9	-9.98
10	-19.143

in

Fiber yield stress:

$\sigma_y =$

	1
1	0.696
2	0.754
3	0.788
4	0.820
5	0.889
6	0.889
7	0.820
8	0.788
9	0.754
10	0.696

ksi

Fiber yield strain:

$\varepsilon_y =$

	1
1	0.000393
2	0.000426
3	0.000445
4	0.000463
5	0.000502
6	0.000502
7	0.000463
8	0.000445
9	0.000426
10	0.000393

PEER REPORTS

PEER reports are available from the National Information Service for Earthquake Engineering (NISEE). To order PEER reports, please contact the Pacific Earthquake Engineering Research Center, 1301 South 46th Street, Richmond, California 94804-4698. Tel.: (510) 665-3405; Fax: (510) 665-3420.

PEER 2008/08 *Toward Earthquake Resistant Design of Concentrically Braced Steel Structures.* Patxi Uriz and Stephen A. Mahin. November 2008.

PEER 2008/07 *Using OpenSees for Performance-Based Evaluation of Bridges on Liquefiable Soils.* Stephen L. Kramer, Pedro Arduino, and HyungSuk Shin. November 2008.

PEER 2008/06 *Shaking Table Tests and Numerical Investigation of Self-Centering Reinforced Concrete Bridge Columns.* Hyung IL Jeong, Junichi Sakai, and Stephen A. Mahin. September 2008.

PEER 2008/05 *Performance-Based Earthquake Engineering Design Evaluation Procedure for Bridge Foundations Undergoing Liquefaction-Induced Lateral Ground Displacement.* Christian A. Ledezma and Jonathan D. Bray. August 2008.

PEER 2008/04 *Benchmarking of Nonlinear Geotechnical Ground Response Analysis Procedures.* Jonathan P. Stewart, Annie On-Lei Kwok, Yousseff M. A. Hashash, Neven Matasovic, Robert Pyke, Zhiliang Wang, and Zhaohui Yang. August 2008.

PEER 2008/03 *Guidelines for Nonlinear Analysis of Bridge Structures in California.* Ady Aviram, Kevin R. Mackie, and Božidar Stojadinović. August 2008.

PEER 2008/02 *Treatment of Uncertainties in Seismic-Risk Analysis of Transportation Systems.* Evangelos Stergiou and Anne S. Kiremidjian. July 2008.

PEER 2008/01 *Seismic Performance Objectives for Tall Buildings.* William T. Holmes, Charles Kircher, William Petak, and Nabih Youssef. August 2008.

PEER 2007/12 *An Assessment to Benchmark the Seismic Performance of a Code-Conforming Reinforced Concrete Moment-Frame Building.* Curt Haselton, Christine A. Goulet, Judith Mitrani-Reiser, James L. Beck, Gregory G. Deierlein, Keith A. Porter, Jonathan P. Stewart, and Ertugrul Taciroglu. August 2008.

PEER 2007/11 *Bar Buckling in Reinforced Concrete Bridge Columns.* Wayne A. Brown, Dawn E. Lehman, and John F. Stanton. February 2008.

PEER 2007/10 *Computational Modeling of Progressive Collapse in Reinforced Concrete Frame Structures.* Mohamed M. Talaat and Khalid M. Mosalam. May 2008.

PEER 2007/09 *Integrated Probabilistic Performance-Based Evaluation of Benchmark Reinforced Concrete Bridges.* Kevin R. Mackie, John-Michael Wong, and Božidar Stojadinović. January 2008.

PEER 2007/08 *Assessing Seismic Collapse Safety of Modern Reinforced Concrete Moment-Frame Buildings.* Curt B. Haselton and Gregory G. Deierlein. February 2008.

PEER 2007/07 *Performance Modeling Strategies for Modern Reinforced Concrete Bridge Columns.* Michael P. Berry and Marc O. Eberhard. April 2008.

PEER 2007/06 *Development of Improved Procedures for Seismic Design of Buried and Partially Buried Structures.* Linda Al Atik and Nicholas Sitar. June 2007.

PEER 2007/05 *Uncertainty and Correlation in Seismic Risk Assessment of Transportation Systems.* Renee G. Lee and Anne S. Kiremidjian. July 2007.

PEER 2007/04 *Numerical Models for Analysis and Performance-Based Design of Shallow Foundations Subjected to Seismic Loading.* Sivapalan Gajan, Tara C. Hutchinson, Bruce L. Kutter, Prishati Raychowdhury, José A. Ugalde, and Jonathan P. Stewart. May 2008.

PEER 2007/03 *Beam-Column Element Model Calibrated for Predicting Flexural Response Leading to Global Collapse of RC Frame Buildings.* Curt B. Haselton, Abbie B. Liel, Sarah Taylor Lange, and Gregory g. Deierlein. May 2008.

PEER 2007/02 *Campbell-Bozorgnia NGA Ground Motion Relations for the Geometric Mean Horizontal Component of Peak and Spectral Ground Motion Parameters.* Kenneth W. Campbell and Yousef Bozorgnia. May 2007.

PEER 2007/01 *Boore-Atkinson NGA Ground Motion Relations for the Geometric Mean Horizontal Component of Peak and Spectral Ground Motion Parameters.* David M. Boore and Gail M. Atkinson. May. May 2007.

PEER 2006/12 *Societal Implications of Performance-Based Earthquake Engineering.* Peter J. May. May 2007.

PEER 2006/11 *Probabilistic Seismic Demand Analysis Using Advanced Ground Motion Intensity Measures, Attenuation Relationships, and Near-Fault Effects.* Polsak Tothong and C. Allin Cornell. March 2007.

PEER 2006/10 *Application of the PEER PBEE Methodology to the I-880 Viaduct.* Sashi Kunnath. February 2007.

PEER 2006/09 *Quantifying Economic Losses from Travel Forgone Following a Large Metropolitan Earthquake.* James Moore, Sungbin Cho, Yue Yue Fan, and Stuart Werner. November 2006.

PEER 2006/08 *Vector-Valued Ground Motion Intensity Measures for Probabilistic Seismic Demand Analysis*. Jack W. Baker and C. Allin Cornell. October 2006.

PEER 2006/07 *Analytical Modeling of Reinforced Concrete Walls for Predicting Flexural and Coupled–Shear-Flexural Responses*. Kutay Orakcal, Leonardo M. Massone, and John W. Wallace. October 2006.

PEER 2006/06 *Nonlinear Analysis of a Soil-Drilled Pier System under Static and Dynamic Axial Loading.* Gang Wang and Nicholas Sitar. November 2006.

PEER 2006/05 *Advanced Seismic Assessment Guidelines.* Paolo Bazzurro, C. Allin Cornell, Charles Menun, Maziar Motahari, and Nicolas Luco. September 2006.

PEER 2006/04 *Probabilistic Seismic Evaluation of Reinforced Concrete Structural Components and Systems.* Tae Hyung Lee and Khalid M. Mosalam. August 2006.

PEER 2006/03 *Performance of Lifelines Subjected to Lateral Spreading.* Scott A. Ashford and Teerawut Juirnarongrit. July 2006.

PEER 2006/02 *Pacific Earthquake Engineering Research Center Highway Demonstration Project.* Anne Kiremidjian, James Moore, Yue Yue Fan, Nesrin Basoz, Ozgur Yazali, and Meredith Williams. April 2006.

PEER 2006/01 *Bracing Berkeley. A Guide to Seismic Safety on the UC Berkeley Campus.* Mary C. Comerio, Stephen Tobriner, and Ariane Fehrenkamp. January 2006.

PEER 2005/16 *Seismic Response and Reliability of Electrical Substation Equipment and Systems.* Junho Song, Armen Der Kiureghian, and Jerome L. Sackman. April 2006.

PEER 2005/15 *CPT-Based Probabilistic Assessment of Seismic Soil Liquefaction Initiation.* R. E. S. Moss, R. B. Seed, R. E. Kayen, J. P. Stewart, and A. Der Kiureghian. April 2006.

PEER 2005/14 *Workshop on Modeling of Nonlinear Cyclic Load-Deformation Behavior of Shallow Foundations.* Bruce L. Kutter, Geoffrey Martin, Tara Hutchinson, Chad Harden, Sivapalan Gajan, and Justin Phalen. March 2006.

PEER 2005/13 *Stochastic Characterization and Decision Bases under Time-Dependent Aftershock Risk in Performance-Based Earthquake Engineering.* Gee Liek Yeo and C. Allin Cornell. July 2005.

PEER 2005/12 *PEER Testbed Study on a Laboratory Building: Exercising Seismic Performance Assessment.* Mary C. Comerio, editor. November 2005.

PEER 2005/11 *Van Nuys Hotel Building Testbed Report: Exercising Seismic Performance Assessment.* Helmut Krawinkler, editor. October 2005.

PEER 2005/10 *First NEES/E-Defense Workshop on Collapse Simulation of Reinforced Concrete Building Structures.* September 2005.

PEER 2005/09 *Test Applications of Advanced Seismic Assessment Guidelines.* Joe Maffei, Karl Telleen, Danya Mohr, William Holmes, and Yuki Nakayama. August 2006.

PEER 2005/08 *Damage Accumulation in Lightly Confined Reinforced Concrete Bridge Columns.* R. Tyler Ranf, Jared M. Nelson, Zach Price, Marc O. Eberhard, and John F. Stanton. April 2006.

PEER 2005/07 *Experimental and Analytical Studies on the Seismic Response of Freestanding and Anchored Laboratory Equipment.* Dimitrios Konstantinidis and Nicos Makris. January 2005.

PEER 2005/06 *Global Collapse of Frame Structures under Seismic Excitations*. Luis F. Ibarra and Helmut Krawinkler. September 2005.

PEER 2005//05 *Performance Characterization of Bench- and Shelf-Mounted Equipment.* Samit Ray Chaudhuri and Tara C. Hutchinson. May 2006.

PEER 2005/04 *Numerical Modeling of the Nonlinear Cyclic Response of Shallow Foundations.* Chad Harden, Tara Hutchinson, Geoffrey R. Martin, and Bruce L. Kutter. August 2005.

PEER 2005/03 *A Taxonomy of Building Components for Performance-Based Earthquake Engineering.* Keith A. Porter. September 2005.

PEER 2005/02 *Fragility Basis for California Highway Overpass Bridge Seismic Decision Making*. Kevin R. Mackie and Božidar Stojadinović. June 2005.

PEER 2005/01 *Empirical Characterization of Site Conditions on Strong Ground Motion.* Jonathan P. Stewart, Yoojoong Choi, and Robert W. Graves. June 2005.

PEER 2004/09 *Electrical Substation Equipment Interaction: Experimental Rigid Conductor Studies.* Christopher Stearns and André Filiatrault. February 2005.

PEER 2004/08 *Seismic Qualification and Fragility Testing of Line Break 550-kV Disconnect Switches.* Shakhzod M. Takhirov, Gregory L. Fenves, and Eric Fujisaki. January 2005.

PEER 2004/07 *Ground Motions for Earthquake Simulator Qualification of Electrical Substation Equipment.* Shakhzod M. Takhirov, Gregory L. Fenves, Eric Fujisaki, and Don Clyde. January 2005.

PEER 2004/06 *Performance-Based Regulation and Regulatory Regimes.* Peter J. May and Chris Koski. September 2004.

PEER 2004/05 *Performance-Based Seismic Design Concepts and Implementation: Proceedings of an International Workshop.* Peter Fajfar and Helmut Krawinkler, editors. September 2004.

PEER 2004/04 *Seismic Performance of an Instrumented Tilt-up Wall Building.* James C. Anderson and Vitelmo V. Bertero. July 2004.

PEER 2004/03 *Evaluation and Application of Concrete Tilt-up Assessment Methodologies.* Timothy Graf and James O. Malley. October 2004.

PEER 2004/02 *Analytical Investigations of New Methods for Reducing Residual Displacements of Reinforced Concrete Bridge Columns.* Junichi Sakai and Stephen A. Mahin. August 2004.

PEER 2004/01 *Seismic Performance of Masonry Buildings and Design Implications.* Kerri Anne Taeko Tokoro, James C. Anderson, and Vitelmo V. Bertero. February 2004.

PEER 2003/18 *Performance Models for Flexural Damage in Reinforced Concrete Columns.* Michael Berry and Marc Eberhard. August 2003.

PEER 2003/17 *Predicting Earthquake Damage in Older Reinforced Concrete Beam-Column Joints.* Catherine Pagni and Laura Lowes. October 2004.

PEER 2003/16 *Seismic Demands for Performance-Based Design of Bridges.* Kevin Mackie and Božidar Stojadinović. August 2003.

PEER 2003/15 *Seismic Demands for Nondeteriorating Frame Structures and Their Dependence on Ground Motions.* Ricardo Antonio Medina and Helmut Krawinkler. May 2004.

PEER 2003/14 *Finite Element Reliability and Sensitivity Methods for Performance-Based Earthquake Engineering.* Terje Haukaas and Armen Der Kiureghian. April 2004.

PEER 2003/13 *Effects of Connection Hysteretic Degradation on the Seismic Behavior of Steel Moment-Resisting Frames.* Janise E. Rodgers and Stephen A. Mahin. March 2004.

PEER 2003/12 *Implementation Manual for the Seismic Protection of Laboratory Contents: Format and Case Studies.* William T. Holmes and Mary C. Comerio. October 2003.

PEER 2003/11 *Fifth U.S.-Japan Workshop on Performance-Based Earthquake Engineering Methodology for Reinforced Concrete Building Structures.* February 2004.

PEER 2003/10 *A Beam-Column Joint Model for Simulating the Earthquake Response of Reinforced Concrete Frames.* Laura N. Lowes, Nilanjan Mitra, and Arash Altoontash. February 2004.

PEER 2003/09 *Sequencing Repairs after an Earthquake: An Economic Approach.* Marco Casari and Simon J. Wilkie. April 2004.

PEER 2003/08 *A Technical Framework for Probability-Based Demand and Capacity Factor Design (DCFD) Seismic Formats*. Fatemeh Jalayer and C. Allin Cornell. November 2003.

PEER 2003/07 *Uncertainty Specification and Propagation for Loss Estimation Using FOSM Methods.* Jack W. Baker and C. Allin Cornell. September 2003.

PEER 2003/06 *Performance of Circular Reinforced Concrete Bridge Columns under Bidirectional Earthquake Loading*. Mahmoud M. Hachem, Stephen A. Mahin, and Jack P. Moehle. February 2003.

PEER 2003/05 *Response Assessment for Building-Specific Loss Estimation.* Eduardo Miranda and Shahram Taghavi. September 2003.

PEER 2003/04 *Experimental Assessment of Columns with Short Lap Splices Subjected to Cyclic Loads*. Murat Melek, John W. Wallace, and Joel Conte. April 2003.

PEER 2003/03 *Probabilistic Response Assessment for Building-Specific Loss Estimation.* Eduardo Miranda and Hesameddin Aslani. September 2003.

PEER 2003/02 *Software Framework for Collaborative Development of Nonlinear Dynamic Analysis Program.* Jun Peng and Kincho H. Law. September 2003.

PEER 2003/01 *Shake Table Tests and Analytical Studies on the Gravity Load Collapse of Reinforced Concrete Frames.* Kenneth John Elwood and Jack P. Moehle. November 2003.

PEER 2002/24 *Performance of Beam to Column Bridge Joints Subjected to a Large Velocity Pulse.* Natalie Gibson, André Filiatrault, and Scott A. Ashford. April 2002.

PEER 2002/23 *Effects of Large Velocity Pulses on Reinforced Concrete Bridge Columns.* Greg L. Orozco and Scott A. Ashford. April 2002.

PEER 2002/22 *Characterization of Large Velocity Pulses for Laboratory Testing.* Kenneth E. Cox and Scott A. Ashford. April 2002.

PEER 2002/21 *Fourth U.S.-Japan Workshop on Performance-Based Earthquake Engineering Methodology for Reinforced Concrete Building Structures*. December 2002.

PEER 2002/20 *Barriers to Adoption and Implementation of PBEE Innovations.* Peter J. May. August 2002.

PEER 2002/19 *Economic-Engineered Integrated Models for Earthquakes: Socioeconomic Impacts.* Peter Gordon, James E. Moore II, and Harry W. Richardson. July 2002.

PEER 2002/18 *Assessment of Reinforced Concrete Building Exterior Joints with Substandard Details.* Chris P. Pantelides, Jon Hansen, Justin Nadauld, and Lawrence D. Reaveley. May 2002.

PEER 2002/17 *Structural Characterization and Seismic Response Analysis of a Highway Overcrossing Equipped with Elastomeric Bearings and Fluid Dampers: A Case Study.* Nicos Makris and Jian Zhang. November 2002.

PEER 2002/16 *Estimation of Uncertainty in Geotechnical Properties for Performance-Based Earthquake Engineering.* Allen L. Jones, Steven L. Kramer, and Pedro Arduino. December 2002.

PEER 2002/15 *Seismic Behavior of Bridge Columns Subjected to Various Loading Patterns.* Asadollah Esmaeily-Gh. and Yan Xiao. December 2002.

PEER 2002/14 *Inelastic Seismic Response of Extended Pile Shaft Supported Bridge Structures.* T.C. Hutchinson, R.W. Boulanger, Y.H. Chai, and I.M. Idriss. December 2002.

PEER 2002/13 *Probabilistic Models and Fragility Estimates for Bridge Components and Systems.* Paolo Gardoni, Armen Der Kiureghian, and Khalid M. Mosalam. June 2002.

PEER 2002/12 *Effects of Fault Dip and Slip Rake on Near-Source Ground Motions: Why Chi-Chi Was a Relatively Mild M7.6 Earthquake.* Brad T. Aagaard, John F. Hall, and Thomas H. Heaton. December 2002.

PEER 2002/11 *Analytical and Experimental Study of Fiber-Reinforced Strip Isolators*. James M. Kelly and Shakhzod M. Takhirov. September 2002.

PEER 2002/10 *Centrifuge Modeling of Settlement and Lateral Spreading with Comparisons to Numerical Analyses***.** Sivapalan Gajan and Bruce L. Kutter. January 2003.

PEER 2002/09 *Documentation and Analysis of Field Case Histories of Seismic Compression during the 1994 Northridge, California, Earthquake.* Jonathan P. Stewart, Patrick M. Smith, Daniel H. Whang, and Jonathan D. Bray. October 2002.

PEER 2002/08 *Component Testing, Stability Analysis and Characterization of Buckling-Restrained Unbonded Braces™.* Cameron Black, Nicos Makris, and Ian Aiken. September 2002.

PEER 2002/07 *Seismic Performance of Pile-Wharf Connections.* Charles W. Roeder, Robert Graff, Jennifer Soderstrom, and Jun Han Yoo. December 2001.

PEER 2002/06 *The Use of Benefit-Cost Analysis for Evaluation of Performance-Based Earthquake Engineering Decisions*. Richard O. Zerbe and Anthony Falit-Baiamonte. September 2001.

PEER 2002/05 *Guidelines, Specifications, and Seismic Performance Characterization of Nonstructural Building Components and Equipment*. André Filiatrault, Constantin Christopoulos, and Christopher Stearns. September 2001.

PEER 2002/04 *Consortium of Organizations for Strong-Motion Observation Systems and the Pacific Earthquake Engineering Research Center Lifelines Program: Invited Workshop on Archiving and Web Dissemination of Geotechnical Data, 4–5 October 2001*. September 2002.

PEER 2002/03 *Investigation of Sensitivity of Building Loss Estimates to Major Uncertain Variables for the Van Nuys Testbed.* Keith A. Porter, James L. Beck, and Rustem V. Shaikhutdinov. August 2002.

PEER 2002/02 *The Third U.S.-Japan Workshop on Performance-Based Earthquake Engineering Methodology for Reinforced Concrete Building Structures*. July 2002.

PEER 2002/01 *Nonstructural Loss Estimation: The UC Berkeley Case Study.* Mary C. Comerio and John C. Stallmeyer. December 2001.

PEER 2001/16 *Statistics of SDF-System Estimate of Roof Displacement for Pushover Analysis of Buildings.* Anil K. Chopra, Rakesh K. Goel, and Chatpan Chintanapakdee. December 2001.

PEER 2001/15 *Damage to Bridges during the 2001 Nisqually Earthquake.* R. Tyler Ranf, Marc O. Eberhard, and Michael P. Berry. November 2001.

PEER 2001/14 *Rocking Response of Equipment Anchored to a Base Foundation*. Nicos Makris and Cameron J. Black. September 2001.

PEER 2001/13 *Modeling Soil Liquefaction Hazards for Performance-Based Earthquake Engineering.* Steven L. Kramer and Ahmed-W. Elgamal. February 2001.

PEER 2001/12 *Development of Geotechnical Capabilities in OpenSees.* Boris Jeremi . September 2001.

PEER 2001/11 *Analytical and Experimental Study of Fiber-Reinforced Elastomeric Isolators*. James M. Kelly and Shakhzod M. Takhirov. September 2001.

PEER 2001/10 *Amplification Factors for Spectral Acceleration in Active Regions.* Jonathan P. Stewart, Andrew H. Liu, Yoojoong Choi, and Mehmet B. Baturay. December 2001.

PEER 2001/09 *Ground Motion Evaluation Procedures for Performance-Based Design.* Jonathan P. Stewart, Shyh-Jeng Chiou, Jonathan D. Bray, Robert W. Graves, Paul G. Somerville, and Norman A. Abrahamson. September 2001.

PEER 2001/08 *Experimental and Computational Evaluation of Reinforced Concrete Bridge Beam-Column Connections for Seismic Performance*. Clay J. Naito, Jack P. Moehle, and Khalid M. Mosalam. November 2001.

PEER 2001/07 *The Rocking Spectrum and the Shortcomings of Design Guidelines.* Nicos Makris and Dimitrios Konstantinidis. August 2001.

PEER 2001/06 *Development of an Electrical Substation Equipment Performance Database for Evaluation of Equipment Fragilities*. Thalia Agnanos. April 1999.

PEER 2001/05 *Stiffness Analysis of Fiber-Reinforced Elastomeric Isolators.* Hsiang-Chuan Tsai and James M. Kelly. May 2001.

PEER 2001/04 *Organizational and Societal Considerations for Performance-Based Earthquake Engineering.* Peter J. May. April 2001.

PEER 2001/03 *A Modal Pushover Analysis Procedure to Estimate Seismic Demands for Buildings: Theory and Preliminary Evaluation.* Anil K. Chopra and Rakesh K. Goel. January 2001.

PEER 2001/02 *Seismic Response Analysis of Highway Overcrossings Including Soil-Structure Interaction.* Jian Zhang and Nicos Makris. March 2001.

PEER 2001/01 *Experimental Study of Large Seismic Steel Beam-to-Column Connections.* Egor P. Popov and Shakhzod M. Takhirov. November 2000.

PEER 2000/10 *The Second U.S.-Japan Workshop on Performance-Based Earthquake Engineering Methodology for Reinforced Concrete Building Structures.* March 2000.

PEER 2000/09 *Structural Engineering Reconnaissance of the August 17, 1999 Earthquake: Kocaeli (Izmit), Turkey*. Halil Sezen, Kenneth J. Elwood, Andrew S. Whittaker, Khalid Mosalam, John J. Wallace, and John F. Stanton. December 2000.

PEER 2000/08 *Behavior of Reinforced Concrete Bridge Columns Having Varying Aspect Ratios and Varying Lengths of Confinement.* Anthony J. Calderone, Dawn E. Lehman, and Jack P. Moehle. January 2001.

PEER 2000/07 *Cover-Plate and Flange-Plate Reinforced Steel Moment-Resisting Connections.* Taejin Kim, Andrew S. Whittaker, Amir S. Gilani, Vitelmo V. Bertero, and Shakhzod M. Takhirov. September 2000.

PEER 2000/06 *Seismic Evaluation and Analysis of 230-kV Disconnect Switches.* Amir S. J. Gilani, Andrew S. Whittaker, Gregory L. Fenves, Chun-Hao Chen, Henry Ho, and Eric Fujisaki. July 2000.

PEER 2000/05 *Performance-Based Evaluation of Exterior Reinforced Concrete Building Joints for Seismic Excitation.* Chandra Clyde, Chris P. Pantelides, and Lawrence D. Reaveley. July 2000.

PEER 2000/04 *An Evaluation of Seismic Energy Demand: An Attenuation Approach.* Chung-Che Chou and Chia-Ming Uang. July 1999.

PEER 2000/03 *Framing Earthquake Retrofitting Decisions: The Case of Hillside Homes in Los Angeles.* Detlof von Winterfeldt, Nels Roselund, and Alicia Kitsuse. March 2000.

PEER 2000/02 *U.S.-Japan Workshop on the Effects of Near-Field Earthquake Shaking.* Andrew Whittaker, ed. July 2000.

PEER 2000/01 *Further Studies on Seismic Interaction in Interconnected Electrical Substation Equipment.* Armen Der Kiureghian, Kee-Jeung Hong, and Jerome L. Sackman. November 1999.

PEER 1999/14 *Seismic Evaluation and Retrofit of 230-kV Porcelain Transformer Bushings*. Amir S. Gilani, Andrew S. Whittaker, Gregory L. Fenves, and Eric Fujisaki. December 1999.

PEER 1999/13 *Building Vulnerability Studies: Modeling and Evaluation of Tilt-up and Steel Reinforced Concrete Buildings.* John W. Wallace, Jonathan P. Stewart, and Andrew S. Whittaker, editors. December 1999.

PEER 1999/12 *Rehabilitation of Nonductile RC Frame Building Using Encasement Plates and Energy-Dissipating Devices.* Mehrdad Sasani, Vitelmo V. Bertero, James C. Anderson. December 1999.

PEER 1999/11 *Performance Evaluation Database for Concrete Bridge Components and Systems under Simulated Seismic Loads.* Yael D. Hose and Frieder Seible. November 1999.

PEER 1999/10 *U.S.-Japan Workshop on Performance-Based Earthquake Engineering Methodology for Reinforced Concrete Building Structures.* December 1999.

PEER 1999/09 *Performance Improvement of Long Period Building Structures Subjected to Severe Pulse-Type Ground Motions*. James C. Anderson, Vitelmo V. Bertero, and Raul Bertero. October 1999.

PEER 1999/08 *Envelopes for Seismic Response Vectors.* Charles Menun and Armen Der Kiureghian. July 1999.

PEER 1999/07 *Documentation of Strengths and Weaknesses of Current Computer Analysis Methods for Seismic Performance of Reinforced Concrete Members.* William F. Cofer. November 1999.

PEER 1999/06 *Rocking Response and Overturning of Anchored Equipment under Seismic Excitations.* Nicos Makris and Jian Zhang. November 1999.

PEER 1999/05 *Seismic Evaluation of 550 kV Porcelain Transformer Bushings.* Amir S. Gilani, Andrew S. Whittaker, Gregory L. Fenves, and Eric Fujisaki. October 1999.

PEER 1999/04 *Adoption and Enforcement of Earthquake Risk-Reduction Measures.* Peter J. May, Raymond J. Burby, T. Jens Feeley, and Robert Wood.

PEER 1999/03 *Task 3 Characterization of Site Response General Site Categories*. Adrian Rodriguez-Marek, Jonathan D. Bray, and Norman Abrahamson. February 1999.

PEER 1999/02 *Capacity-Demand-Diagram Methods for Estimating Seismic Deformation of Inelastic Structures: SDF Systems*. Anil K. Chopra and Rakesh Goel. April 1999.

PEER 1999/01 *Interaction in Interconnected Electrical Substation Equipment Subjected to Earthquake Ground Motions.* Armen Der Kiureghian, Jerome L. Sackman, and Kee-Jeung Hong. February 1999.

PEER 1998/08 *Behavior and Failure Analysis of a Multiple-Frame Highway Bridge in the 1994 Northridge Earthquake.* Gregory L. Fenves and Michael Ellery. December 1998.

PEER 1998/07 *Empirical Evaluation of Inertial Soil-Structure Interaction Effects.* Jonathan P. Stewart, Raymond B. Seed, and Gregory L. Fenves. November 1998.

PEER 1998/06 *Effect of Damping Mechanisms on the Response of Seismic Isolated Structures.* Nicos Makris and Shih-Po Chang. November 1998.

PEER 1998/05 *Rocking Response and Overturning of Equipment under Horizontal Pulse-Type Motions.* Nicos Makris and Yiannis Roussos. October 1998.

PEER 1998/04 *Pacific Earthquake Engineering Research Invitational Workshop Proceedings, May 14–15, 1998: Defining the Links between Planning, Policy Analysis, Economics and Earthquake Engineering.* Mary Comerio and Peter Gordon. September 1998.

PEER 1998/03 *Repair/Upgrade Procedures for Welded Beam to Column Connections.* James C. Anderson and Xiaojing Duan. May 1998.

PEER 1998/02 *Seismic Evaluation of 196 kV Porcelain Transformer Bushings.* Amir S. Gilani, Juan W. Chavez, Gregory L. Fenves, and Andrew S. Whittaker. May 1998.

PEER 1998/01 *Seismic Performance of Well-Confined Concrete Bridge Columns.* Dawn E. Lehman and Jack P. Moehle. December 2000.

ONLINE REPORTS

The following PEER reports are available by Internet only at http://peer.berkeley.edu/publications/peer_reports.html

PEER 2008/103 *Experimental and Computational Evaluation of Current and Innovative In-Span Hinge Details in Reinforced Concrete Box-Girder Bridges. Part 1: Experimental Findings and Pre-Test Analysis.* Matias A. Hube and Khalid M. Mosalam. January 2009.

PEER 2008/102 *Modeling of Unreinforced Masonry Infill Walls Considering In-Plane and Out-of-Plane Interaction.* Stephen Kadysiewski and Khalid M. Mosalam. January 2009.

PEER 2008/101 *Seismic Performance Objectives for Tall Buildings.* William T. Holmes, Charles Kircher, William Petak, and Nabih Youssef. August 2008.

PEER 2007/101 *Generalized Hybrid Simulation Framework for Structural Systems Subjected to Seismic Loading.* Tarek Elkhoraibi and Khalid M. Mosalam. July 2007.

PEER 2007/100 *Seismic Evaluation of Reinforced Concrete Buildings Including Effects of Masonry Infill Walls.* Alidad Hashemi and Khalid M. Mosalam. July 2007.